Multidimensional Characterisation of Inorganic Nanoparticles Using Scanning Transmission Electron Microscopy

A thesis submitted to The University of Manchester for the degree of

Doctor of Philosophy

in the Faculty of Science and Engineering

by

Yichi Wang

2019

Department of Materials

List of Contents

Word counts: 37559

List of Abbreviations

2D: two-dimensional

3D: three-dimensional

CTEM: conventional transmission electron microscopy

DP: diffraction pattern

EDS: energy dispersive x-ray spectroscopy

EELS: electron energy loss spectroscopy

FCC: face centred cubic

FEG: field emission gun

FET: field-effect transistor

HAADF: high angle annular dark field

PtNi: platinum-nickel

ROI: region of interests

SDD: silicon drift detector

STEM: scanning transmission electron microscopy/microscope

SPR: single particle reconstruction

SNR: signal-to-noise ratio

TS-ET: tilt-series electron tomography

TEM: transmission electron microscope

Abstract

In this thesis, an electron fluence efficient method for the 3D chemical imaging of inorganic nanoparticles have been explored through the use of scanning transmission electron microscopy (STEM), high angle annular dark field image (HAADF) and energy dispersive X-ray spectroscopy (EDS). The method, termed as spectroscopic single particle reconstruction (SPR), assumes nanoparticles are identical but randomly orientated on a support. Thus by expose each nanoparticle to electron beam only once, a collection of nanoparticles viewed at different orientations can be obtained to perform 3D reconstruction. Unlike tilt-series electron tomography (TS-ET) which images the same specimen multiple times, spectroscopic single particle reconstruction disperses total dose budget to all imaged particles thus not only enables the ability to imaging beam sensitive nanoparticles in 3D, but also increase the EDS counts for better EDS quantification.

The presumption of nanoparticle population homogeneity can be eased to that only a subset of the whole population are all identical. By applying selection criterion such as thresholding nanoparticle compositions, platinum-nickel (PtNi) nanoparticles contain 45-55 at% Pt and 55-65 at% Pt were characterised by spectroscopic single particle reconstruction approach and found they show similar 3D elemental segregation behaviour. The 3D elemental segregation results not only agree with previous reports to show Ni-enriched facets, but also find new evidence for the importance of considering effect of crystallographic vertices and surface facets on local elemental distribution.

An additional advantage of spectroscopic SPR for 3D imaging is that no high angle tilt is needed, which opens the possibility to perform 3D structural and chemical imaging for nanoparticles in-situ using all ranges of commercial in-situ holders without special requirement for high tilt to do TS-ET. This opportunity is explored using an in-situ heating holder to reconstruct the 3D structure transformation of PtNi at different temperatures.

Declaration

No portion of the work referred to in the thesis has been submitted in support of an application for another degree or qualification of this or any other university or other institute of learning

Copyright Statement

Acknowledgements

I would like to express the sincerest gratitude to my supervisor, Prof Sarah Haigh, and my mentor, Dr Thomas Slater. My PhD journey would be much harder without their guidance and support. They are always very patient with me, never missed our meetings and always provide constructive advices.

I would like to thank all members of the Haigh group and staffs in electron microscopy centre. In particular, I want to thank Mr. Matthew Smith for his nice teaching of TEM. I would also like to thank my collaborators. I also wish to thank my friends.

Special thanks to my parents, who always love and support me.

Finally, I want to express my thanks to myself.

I would like to acknowledge the China Scholarship Council for the support of my PhD study.

Publications

Journal

- **Wang, Y. C.**, Slater, T.J., Leteba, G.M., Roseman, A.M., Race, C.P., Young, N.P., Kirkland, A.I., Lang, C.I. and Haigh, S.J., (2019). Imaging Three-Dimensional Elemental Inhomogeneity in Pt–Ni Nanoparticles Using Spectroscopic Single Particle Reconstruction. *Nano Letters,* 19(2), 732-738. (DOI: 10.1021/acs.nanolett.8b03768)
- **Wang, Y. C.**, Slater, T.J.A., Rodrigues, T.S., Camargo, P.H.C. and Haigh, S.J., (2017). Automated quantification of morphology and chemistry from STEM data of individual nanoparticles. *Journal of Physics: Conference Series*, 902, 012018. (DOI: 10.1088/1742-6596/902/1/012018)
- Xu, S., Chansai, S., Shao, Y., Xu, S., **Wang, Y.C.**, Haigh, S.J., Mu, Y., Jiao, Y., Stere, C.E., Chen, H., Fan, X., Hardacre, C. (2020). Mechanistic Study of Non-Thermal Plasma Assisted CO2 Hydrogenation over Ru Supported on MgAl Layered Double Hydroxide. *Applied Catalysis B: Environmental* (DOI: 10.1016/j.apcatb.2020.118752)
- Nguyen, T. S., McKeever, P., Arredondo-Arechavala, M., **Wang, Y. C**., Slater, T. J. A., Haigh, S. J., Beale, A. M., Thompson, J. M. (2020). Correlation of the ratio of metallic to oxide species with activity of PdPt catalysts for methane oxidation *Catalysis Science & Technology*.(DOI: 0.1039/C9CY02371B)
- Yu, W., Batchelor-McAuley, C., **Wang, Y.C.,** Shao, S.Q., Fairclough, S.M., Haigh, S.J., Young, N.P. and Compton, R.G., (2019). Characterising Porosity in Platinum Nanoparticles. *Nanoscale*.(DOI: 10.1039/C9NR06071E)
- Li, X., Iqbal, M.A., Xu, M., **Wang, Y. C.**, Wang, H., Ji, M., Wan, X., Slater, T.J., Liu, J., Liu, J. and Rong, H., Chen, W., Stephen, V.K., Haigh, S.J., Rogach, A.L., Xie, L., Zhang, J., (2019). Au@HgxCd1-xTe core@shell nanorods by sequential aqueous cation exchange for near-infrared photodetectors, *Nano Energy*, 57, 57-65. (DOI: 10.1016/j.nanoen.2018.12.030)
- Quiroz, J., Barbosa, E. C., Araujo, T. P., Fiorio, J. L., **Wang, Y. C.**, Zou, Y.C., Mou, T., Alves, T.V., de Oliveira, D.C., Wang, B. and Haigh, S.J., (2018). Controlling Reaction Selectivity over

Hybrid Plasmonic Nanocatalysts. *Nano Letters*,*18*(11), 7289-7297. (DOI: 10.1021/acs.nanolett.8b03499)

- Stewart, C., Gibson, E.K., Morgan, K., Cibin, G., Dent, A.J., Hardacre, C., Kondratenko, E.V., Kondratenko, V.A., McManus, C., Rogers, S. Stere, C.E., Chansai, S, **Wang, Y.C.**, Haigh, S.J., Wells, P.P., Goguet, A., (2018). Unraveling the H2 Promotional Effect on Palladium-Catalyzed CO Oxidation Using a Combination of Temporally and Spatially Resolved Investigations. *ACS catalysis*, *8*(9), 8255-8262. (DOI: 10.1021/acscatal.8b01509)

Conferences

- **Oral presentation (Aug 2019)** "Three-dimensional imaging of nanoparticle chemistry using spectroscopic single particle reconstruction", Microscopy and Microanalysis, Portland, US
- **Oral presentation (Jul 2019)** "Three-dimensional imaging of nanoparticle chemistry using spectroscopic single particle reconstruction", Microscience Microscopy Congress, Manchester, UK
- **Oral presentation (Jan 2019)** "Nanoscale 3D elemental imaging and quantification of multi-element nanoparticles", UK Catalysis Conference, Loughborough, UK
- **Oral presentation (Aug 2018)** "Revealing 3D elemental distribution in nanoparticles by STEM-EDS tomography", China Electron Microscopy Conference, Chengdu, China
- **Oral presentation (Sep 2018)** "High-throughput chemical imaging and quantification of nanoparticles in 2D and 3D", International Microscopy Congress, Sydney, Australia
- **Oral presentation (Jul 2017)** "Automated quantification of morphology and chemistry from STEM data of individual nanoparticles", Microscience Microscopy Congress, Manchester, UK
- **Oral presentation (May 2016)** "Image processing and 3D reconstruction of nanoparticles via STEM data", Postgraduate Reseachers Conference, Manchester, UK
- **Oral and poster presentation (Jul 2016)** "Automated quantification of Ag-Pt/Pd nanoparticle surface roughness with STEM data", Electron Microscopy Analysis Group, Durham, UK

1. Introduction

1.1. Project aim and objectives

The main aim of this doctoral project was to characterise the three-dimensional (3D) structure and compositional distribution of beam sensitive nanoparticles using a novel approach named single particle reconstruction. The main objective towards this aim required collection of large data set containing high angle annular dark field (HAADF) images of thousands individual nanoparticles and associated energy dispersive x-ray spectroscopic (EDS) spectrum data. Processing such data set required a systematic imaging and automated data processing method to be developed. Once this was realised, optimisation of the reconstruction quality should be performed in an iterative manner starting from new high quality data acquisition using scanning transmission electron microscopy (STEM) and EDS to utilise various image processing methods. Finally, another dimensionality of characterisation was introduced to incorporate spectroscopic single particle reconstruction (SPR) with in situ heating experiments.

1.2. Thesis structure

The thesis starts with an overview of scanning transmission electron microscopy, followed by detailed EDS in chapter 3. Chapter 4 presents a comparative review of two 3D reconstruction methods, tilt-series electron tomography (TS-ET) and SPR. Chapter 5 contains the study of spectroscopic SPR and its application on platinum-nickel (PtNi) nanoparticles. Chapter 6 extends the application of SPR to in-situ heating experiment to study the structure and composition stability of same PtNi nanoparticles at high temperatures.

2. Transmission electron microscope

The transmission electron microscope (TEM) was invented in the early 1930's by Ernst Ruska and Max Knoll[1]. The illuminating source in TEM is high energy electrons, with few picometer wavelength, which significantly advances the resolution compared to visible light source microscopy. Applicable to electron transparent specimen, TEM has been playing a major role in the investigation of the microscopic world from nanoscale to sub-angstrom scale, for physicists, biologists, materials scientists and chemists. Development of TEM is continuously flourishing in all aspects of theories, hardware and software, benefiting from recent advances in engineering and technology[2,3].

The sequence of this chapter starts with an overview of the configuration of the TEM, followed by electron-matter interactions. Elastic scattering is discussed mainly here as it is the basis of structural imaging and inelastic scattering of EDS is discussed in chapter 3. STEM imaging is detailed in the end of this chapter, along with using the wave interpretation of electrons to understand coherent and incoherent imaging theory.

2.1. Microscope configuration

In this thesis, the acronym TEM strictly means the transmission electron microscope instrument, whereas imaging modes are distinguished as conventional transmission electron microscopy (CTEM) and STEM. The stream of electrons is generally referred to as the 'beam' and the converged beam is also referred to as the 'probe' when necessary.

A schematic of a typical configuration of TEM is illustrated in Figure 2-1, consisting of the gun filament, lenses, beam deflectors, lens stigmators, apertures, detectors and specimen holder.

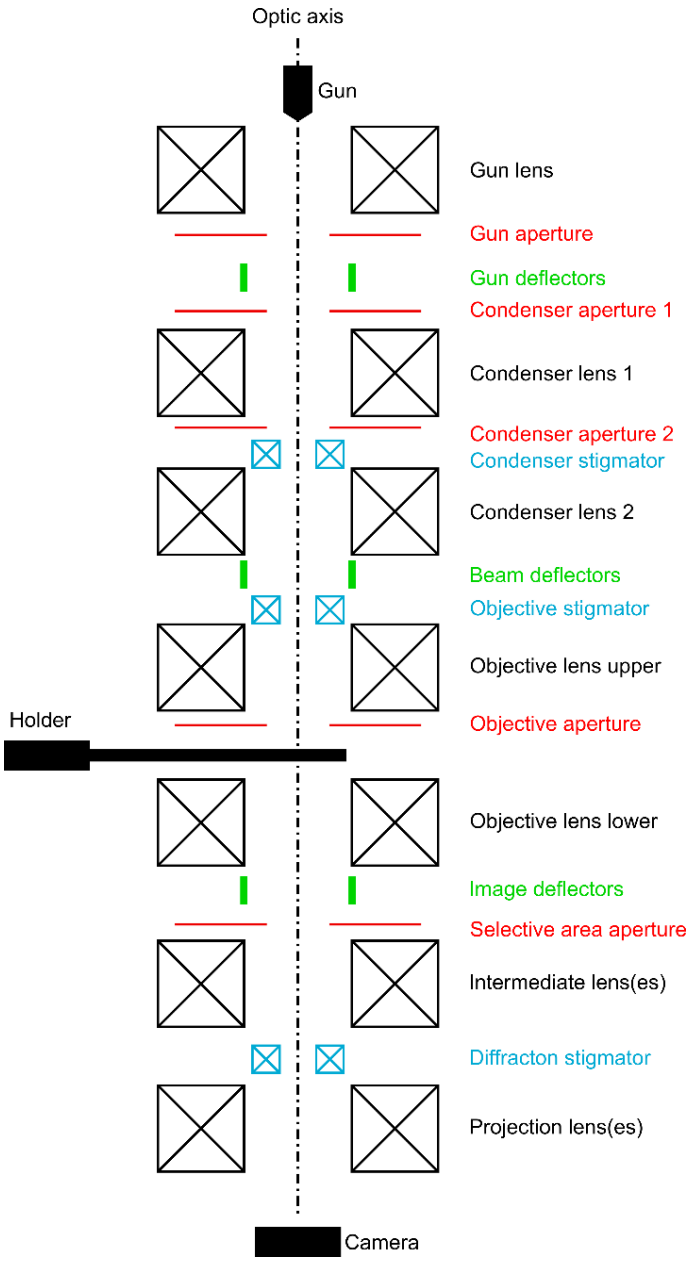

Figure 2-1 A schematic of a typical transmission electron microscope without abberation correctors.

2.1.1. Gun

The gun or the filament is the "light source" of the TEM and electrons are generated from it when high temperature (thermionic emission) or high voltage (field emission) is applied. The gun materials are usually made by tungsten filament, LaB_6 crystal or tungsten needle. The field emission gun (FEG) has many advantages over the thermionic gun such as resolution, coherence, stability, brightness but requires ultra-high vacuum[4]. There are two types of FEGs, Schottky FEG and cold FEG. Schottky

FEG is constantly heated to eliminate the surface contaminants and oxide but the thermal assistant results in a relative large source size and larger energy spread. The cold FEG is operated at ambient temperature but higher vacuum to ensure clean tip surface. Free of heating on cold FEG provides smaller source size and smaller energy spread which are good for ultimate spatial resolution or energy resolution in electron energy loss spectroscopy (EELS), but the beam current in a cold FEG unavoidably fades with time due to trapped contaminants on the tip surface. Therefore, cold FEG TEM needs tip flashing to eliminate tip contamination after several hours of operation[5].

2.1.2. Lenses

Lenses are usually electromagnetic lenses in almost all modern TEMs[6]. Electric current through the lens controls its focus strength to magnify or demagnify the beam, producing images or diffraction patterns (DPs). The theory of lens magnification can be described by Newton's lens equation[6] and Figure 2-2:

$$\frac{1}{f} = \frac{1}{d_o} + \frac{1}{d_i} \qquad \text{Equation 1}$$

Where f is the focal length, d_o is the object distance and d_i is the image distance. According to the lens equation, the magnification of a convex lens M is defined as:

$$M = \frac{d_i}{d_o} \qquad \text{Equation 2}$$

Therefore, reducing the object distance d_o by placing the specimen closer to a lens and/or increase the image distance d_i (focal length) by increasing the lens strength can increase magnification. In addition, using a combination of lenses and placing the image plane of the first lens to coincide with the object plane of the second lens and so on, magnification can be further increased. This is the basic theory for demagnification of illuminating source to sub-angstrom probe in STEM and for magnification of images and DPs in CTEM.

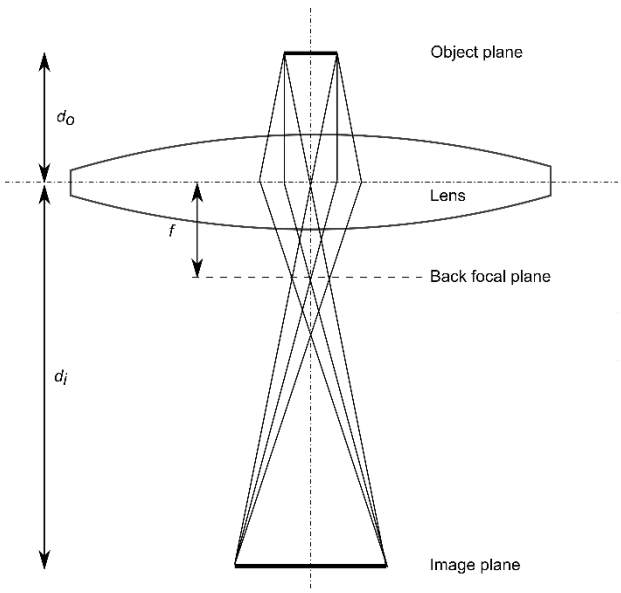

Figure 2-2 The ray diagram for the lens equation.

Condenser lenses installed above the specimen are used to transform either parallel or convergent electron beam onto specimen in CTEM and STEM, respectively. Objective lenses paired one above and one below the specimen form images and diffraction patterns in CTEM. Intermediate and projection lenses are placed below specimen. For CTEM, these lenses provide flexibility of controlling focal length and magnification for images and DPs. For STEM, these lenses control cameral length and decide detector collection angles.

2.1.3. Apertures

Apertures are disks or a strip made from heavy metals such as Pt or Mo with circular holes on them. Apertures are inserted in the optic axis to exclude electrons travelling outside the aperture hole. Depending on the position of the aperture, using an aperture has five main purposes: 1) reducing the beam convergence angle; 2) limiting the lens collection angle; 3) changing beam current; 4) selecting diffracted beam based on diffraction angles and 5) selecting region of interest in real space.

However, introducing an aperture causes electron wave diffraction, blurring an image of a point to a disc with surrounding oscillations, i.e. an Airy disk. The radii of the Airy disk (r_{th}) in TEM is approximately[7]:

$$r_{th} = 1.22\frac{\lambda}{\beta}$$ Equation 3

Where λ is the wavelength of the electron beam and β is the semi-collection angle of the aperture.

This equation is also the theoretical resolution of the TEM using the Rayleigh criterion, i.e. two resolvable Airy disks are separated by the radius of the Airy disc. Therefore, the equation 3 also demonstrates that increasing the aperture size (β) can improve the ultimate achievable resolution, although in practice using larger aperture size the lens aberration is becoming the limiting factor of the resolution.

2.1.4. Deflectors

Deflectors tilt or shift the beam with respect to the optic axis, which requires a pair of coils applying inverse magnetic fields on either side of the beam. Except for alignments, beam tilt is essential in advanced imaging techniques such as precision electron diffraction[8] and beam shift is normal for STEM to control beam scan over the specimen pixel by pixel.

2.1.5. Aberrations

Lenses in the microscope are not perfect and cause aberrations which distort images. Astigmatism, coma, spherical aberration and chromatic aberration are four major aberrations existing in all TEMs (Figure 2-3).

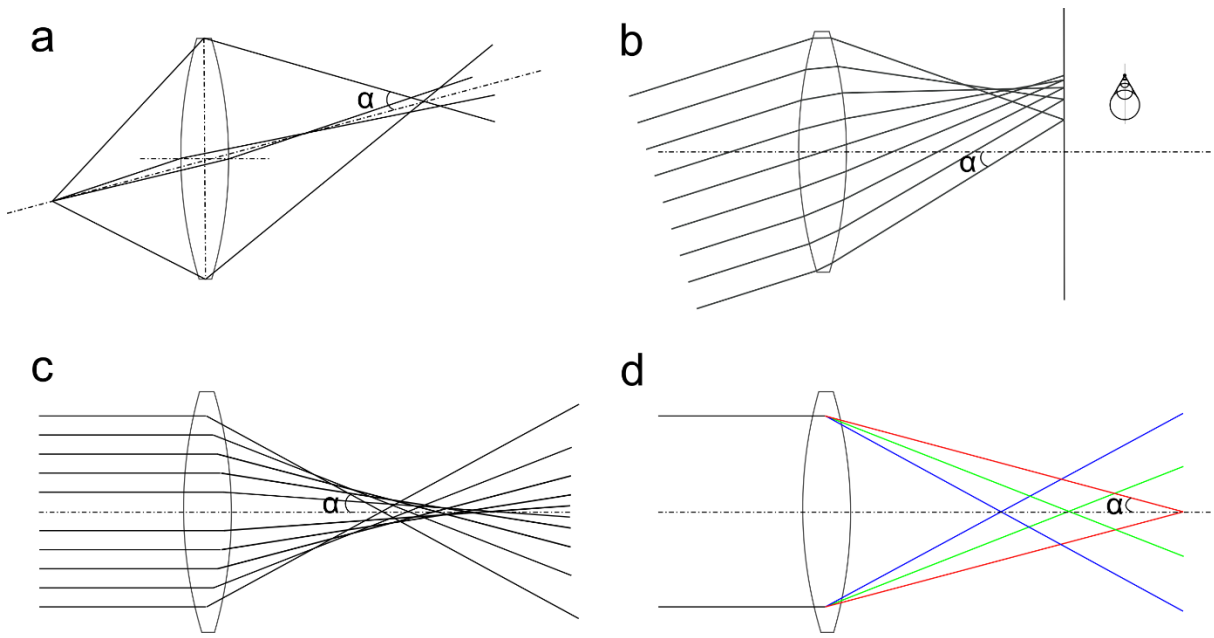

Figure 2-3 Four major abberations exist in TEM. a) Astigmatism. b) Coma. c) Spherical aberration. d) Chromatic aberration. Labeled angle α is the convergence angle.

Astigmatism (Figure 2-3 a) arises due to electrons travelling through a non-uniform magnetic field and therefore the focal length of the passing electrons behaves differently as a function of the azimuthal angle of the lens. This aberration is caused by imperfect manufacturing of cylindrical lenses, microstructural inhomogeneity of the soft iron shell of the lens, a not precisely centred aperture or contamination trapped on the aperture[6]. Astigmatism can be easily corrected using stigmators (another form of lens) to introduce a compensating field.

Coma (Figure 2-3 b) happens when lenses weakly bend incoming rays with a tilt angle at one end of the lens and strongly bend rays at another end of the lens. Aligning beam parallel to the optic axis can reduce this aberration.

Spherical aberration (Figure 2-3 c) occurs because the off-axis electrons are more strongly bent back toward the optic axis. As a result, a point image is blurred to a disk at the Gaussian image plane with a diameter (D) of the disk described as:

$$D = 2C_s\beta^3 \qquad \text{Equation 4}$$

Where C_s is the spherical aberration coefficient and β is the lens/aperture semi-collection angle. It is clear that the spherical aberration increases with larger β.

Correcting spherical aberration is becoming popular as the technology is becoming mature and the ability of aberration corrected TEMs to achieve atomic resolution finds many applications such as analysing atom arrangements at materials surface[9]. C_S-corrector acts like a concave lens to spread out the off-axis beams and ensure they are re-converged onto the same point at the Gaussian image plane. Unlike the usual round lenses, correctors break the cylindrical symmetry and consist of hexapoles[10] or quadrupole-octupole[11] lenses, and are placed below the target objective or condenser lens which needs aberration correction.

Chromatic aberration (Figure 2-3 d) occurs due to the lens focusing low energy electrons more strongly than high energy electrons. The energy difference is less significant at high accelerating voltage (~0.1 eV in a FEG TEM at 100 keV) but more severe at low accelerating voltages[6]. The energy difference can also occur due to energy loss from inelastic scattering as electrons pass through a specimen. Therefore, energy filtered TEM (EFTEM) and EELS will benefit from chromatic aberration free TEM[12]. There are two ways to correct chromatic aberration, either by excluding the outlier electrons that have varied energies before (i.e. monochromator) or after (i.e. EFTEM) the beam passes through the specimen, or install a chromatic aberration corrector underneath the gun lenses to make sure electrons with different energies focus to the same point. Whereas the former method results in a beam current reduction which may be undesirable for high signal-to-noise ratio (SNR) imaging or analysis via EDS. Furthermore, the latter method using a chromatic aberration corrector is still not as widely available as C_S corrector due to various reasons such as cost and instability[7].

2.2. Interaction of electron and sample for information detection

Electrons can be described as particles with mass and momentum or waves with amplitude and phase. Once an electron interacts with specimen atoms, it will behave differently compared to the original incoming electron and this difference carries information about the specimen which we want to detect and interpret. Therefore, basic knowledge about the electron-matter interaction is essential to understand the images and imaging modes in TEM.

If an electron is considered as a particle, it is a low-mass, negatively charged particle. A 'billiard ball' model can approximately describe the interaction of an electron and an atom, governed by the electrostatic Coulomb interaction between incident electrons and positively charged nucleus or negatively charged electron clouds of sample atoms[13]. The probability of an incoming electron hitting an isolated atom can be simply considered as the cross section (σ_{atom}) area of the isolated atom[6]:

$$\sigma_{atom} = \pi r^2 \qquad \text{Equation 5}$$

Where r is the effective scattering radius of an isolated atom and depends on atomic number (Z), accelerating voltage of the incident electron (V) and scattering angle (θ).

The total cross section (σ_t) is the summation of elastic and inelastic cross sections (σ_{el} and σ_{inel}, respectively).

$$\sigma_t = \sigma_{el} + \sigma_{inel} \qquad \text{Equation 6}$$

Considering incident electrons and their interacted specimen atoms as a whole system, elastic and inelastic scattering are usually distinguished as an event when incident electrons result in no loss or measurable loss of kinetic energy after interacting with specimen atoms. If electrons travel elastically through the optic axis in TEM, electrons experience no energy difference but only directional deviation due to scattering, therefore electrons doesn't care which direction they go

through in the TEM. This is the basis of the reciprocity of CTEM and STEM[6]. Only elastic scattering is detailed here and the inelastic EDS imaging mode is detailed in the chapter 3.

2.2.1. Elastic scattering

If the incident electron passes through a small interval of the cross section $d\sigma$ and is scattered into an interval of solid angle $d\Omega$, the probability is described as the differential cross section [6] ($\frac{d\sigma}{d\Omega}$) as a function of scattering angle θ:

$$\frac{d\sigma}{d\Omega} = \frac{1}{2\pi sin\theta}\frac{d\sigma}{d\theta} \qquad \text{Equation 7}$$

Equation 7 demonstrates that increasing scattering angle decreases the interaction cross section.

By integrating Equation 7 over θ from 0 to π, total elastic cross section is obtained [6].

$$\sigma_{el} = 2\pi \int_0^{\pi} \frac{d\sigma}{d\Omega} sin\theta \, d\theta \qquad \text{Equation 8}$$

However, instead of Equation 8, we usually break elastic scattering events into high-angle (more than a few degree) electron-nucleus scattering and low-angle electron-electron scattering. The latter is also called screening effect[6]. Considering both events, elastic scattering can be described as Rutherford scattering differential cross section ($\frac{d\sigma_R}{d\Omega}$) with screening correction and relativistic correction[6]:

$$\frac{d\sigma_R}{d\Omega} = \frac{\lambda_R^4 Z^2}{64\pi^2 a_0^2 (sin^2\frac{\theta}{2} + \frac{\theta_0^2}{4})^2} \qquad \text{Equation 9}$$

Where λ_R is the relativistically corrected wavelength, Z is the atomic number, a_0 is the Bohr radius of the scattering atom and θ_0 is the screening parameter.

The unscreened Rutherford scattering demonstrates that for a fixed accelerating voltage, only collecting electrons scattered at angle θ (or a certain range of angles) using an aperture in CTEM or a

detector in STEM, the image intensity is usually considered to be proportional to Z^2. But screening and relativistic effect slightly reduces the Z^2 dependence to $Z^{1.5\sim2.0}$[7,13,14].

The Rutherford scattering is the basic of mass-thickness contrast for BF and DF in CTEM and Z-contrast in HAADF-STEM[6]. The contrast dependence of specimen thickness arises when converting the above single atom cross section to a specimen cross section considering a collection of atoms.

As mentioned above, the image intensity is proportional to scattering cross section. But it is not accurate as the wave nature has been ignored. If we consider the electrons as waves, the square of the amplitude is proportional to the scattered intensity and therefore the particle nature and wave nature of the elastically scattered electron beam can be related as[6]:

$$|f(\theta)|^2 = \frac{d\sigma_R}{d\Omega} \qquad \text{Equation 10}$$

Where $f(\theta)$ is the atomic scattering factor that measures the amplitude of an electron wave scattered from an isolated atom, defined as[6]:

$$f(\theta) = \frac{\left(1 + \frac{E_0}{m_0 c^2}\right)}{8\pi^2 a_0} \left(\frac{\lambda}{sin\frac{\theta}{2}}\right)^2 (Z - f_x) \qquad \text{Equation 11}$$

The atomic scattering factor drops the screening term and includes the X-ray scattering factor, f_x, to describe both high angle and low-angle elastic scattering more accurately than Rutherford cross section. If we neglect the f_x describing the electron-cloud scattering, $|f(\theta)|^2$ is mathematically equivalent to Equation 9.

Extending the single atom elastic scattering event to crystalline specimens, the structure factor $F(\theta)$ is introduced to measure the amplitude scattered by a unit cell of a crystal structure[6]. The structure factor is defined as the sum of the $f(\theta)$ from all the i atoms with coordinate (x_i, y_i, z_i) in the unit cell. Phase factor is introduced as considering the waves scattered from atoms on different but parallel atomic places with the same Miller indices (hkl):

$$F(\theta) = \sum_{i}^{\infty} f_i e^{2\pi i(hx_i + ky_i + ly_i)}$$ Equation 12

This is the basis of diffraction contrast relating to the type of atom ($f(\theta)$), the position of the atom in the unit cell (x, y, z), and the specific atomic plane (hkl).

2.3. Details of STEM imaging

Considering an electron beam as a wave, it may be coherent or incoherent due to phase shift. The incident beam can be considered as a coherent plane wave, interacting with atoms that act as scattering centres, generating secondary spherical waves interfering with each other to form strong direct zero-order wave (considered as plane wave again, i.e. unscattered transmitted beam) and several higher-order coherent waves scattering at specific angles (θ). Phase differences in coherent scattering in a crystalline lattice is the basis of phase contrast and diffraction contrast imaging. In this section, a more detailed explanation of contrast in STEM imaging is described using the wave interpretation of electron beam.

A simplified schematic of STEM is shown in Figure 2-4 starting from the illuminating source to the detectors. Electrons emitting from the gun can be idealised as a spherical wave $\Psi_s(\boldsymbol{R})$ with unit amplitude 1[15]:

$$\Psi_s(\boldsymbol{R}) = 1 \cdot \frac{e^{2\pi i \boldsymbol{K} \cdot \boldsymbol{R}}}{r}$$ Equation 13

Where $\boldsymbol{K}$ is the 3D wave vector normal to the wave front representing direction of the electron wave propagating from the source. $\boldsymbol{R}$ is the two dimensional specimen vector as the wave seen in specimen position. r is the radius of the spherical wave.

The spherical wave becomes plane wave after demagnification before entering the probe-defining lens and can be described as:

$$\Psi_0(\boldsymbol{R}) = 1 \cdot e^{2\pi i \boldsymbol{K}\cdot\boldsymbol{R}} \qquad \text{Equation 14}$$

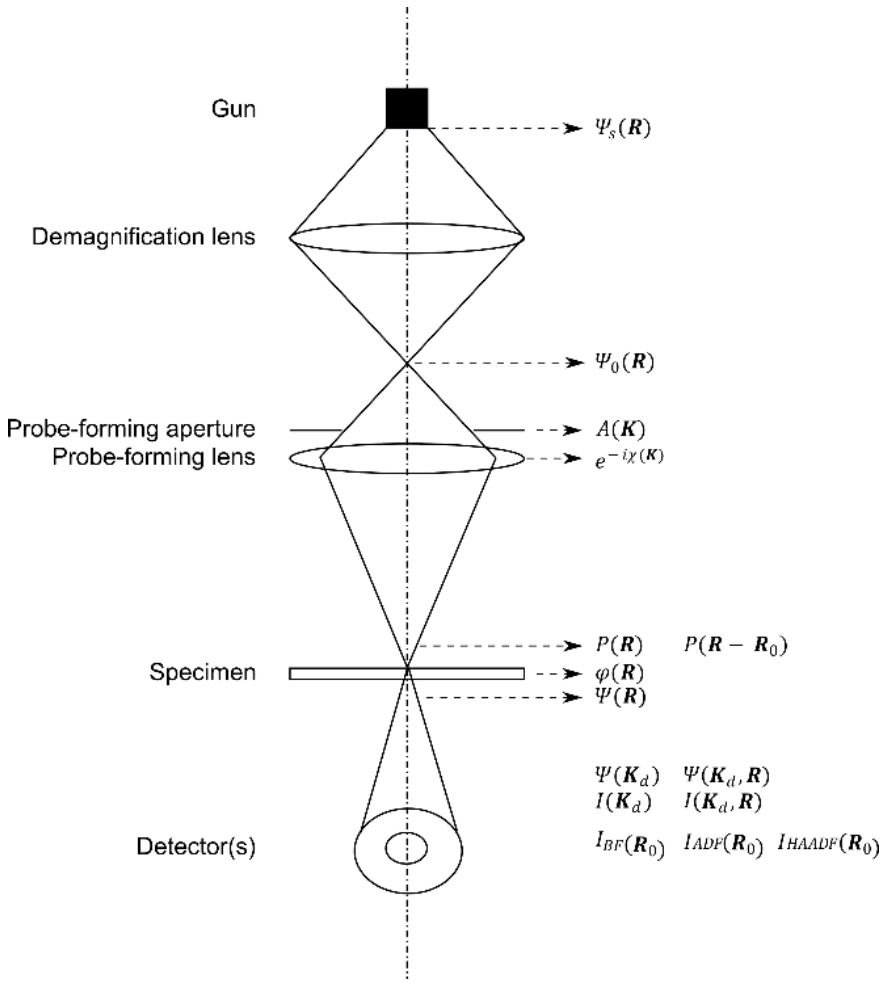

Figure 2-4 A simplified schematic ray diagram of STEM configuration

After plane waves passing through the probe-forming aperture and lens, a small localised electron probe is formed. This probe can be considered in two representations, wave vectors in reciprocal space (Figure 2-5 a) and intensity profiles in real space (Figure 2-5 b). If the probe travels in only one direction, one wave vector can represent its reciprocal form (Figure 2-5 a i) and the corresponding real space intensity is a uniform profile (Figure 2-5 b i). If the probe with few directions passes through an aperture, the corresponding wave vectors are illustrated as Figure 2-5 a ii-iv and its intensity profile are few peaks (Figure 2-5 b ii-iv). For a realistic probe with an infinite number of plane waves at all angles within the probe-forming aperture, all possible wave vectors “fill in” the

reciprocal space confined by the probe-forming aperture (Figure 2-5 a v). The real space intensity of the probe becomes one airy disk (Figure 2-5 b v) due to all waves coherently and destructively adding together.

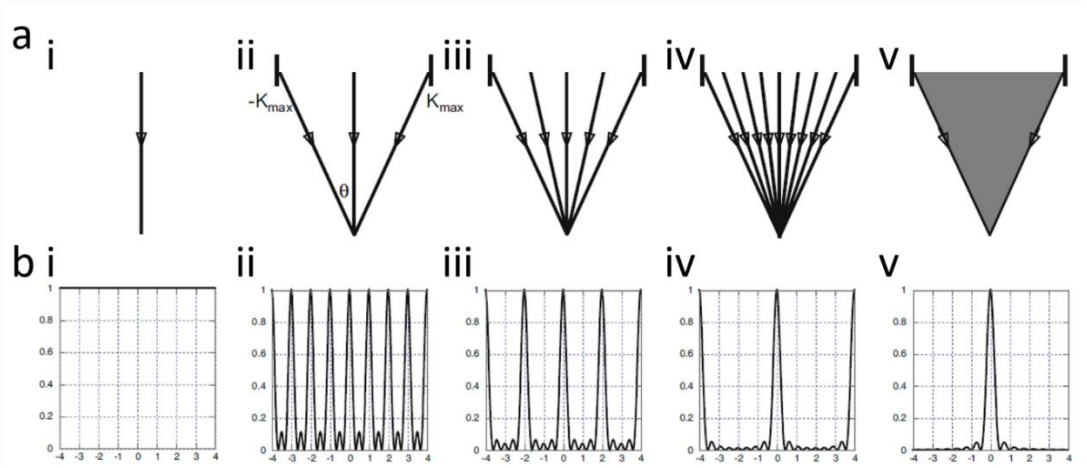

Figure 2-5 Representation of beam in (a) reciprocal space and (b) real space. If the probe only consists of one direction wave vector (a i), the real space intensity is a uniform profile (b i). If wave vectors coming in few distinct directions (a ii-iv), the corresponding intensity profile forms few peaks (b ii-iv). If the probe contains all possible angles within the probe-forming aperture (a v), all waves are coherently added togather and the destructive interference results one airy disk formed in the real space (b v). Reproduced from [15]

The probe amplitude within the aperture is uniform and the circular probe-forming aperture function $A(\boldsymbol{K})$ having a value 1 inside the aperture and zero outside. The probe amplitude in real space is the inverse Fourier transform of the reciprocal space probe amplitude defined by the aperture function:

$$FT^{-1}\{A(\boldsymbol{K})\} = A(\boldsymbol{K})e^{2\pi i\boldsymbol{K}\cdot\boldsymbol{R}} \qquad \text{Equation 15}$$

Integrating this function over the aperture, we have the real space probe amplitude function without consider the effect of any lens aberration, $P_{w/o}$:

$$P_{w/o}(\boldsymbol{R}) = \int A(\boldsymbol{K}) e^{2\pi i \boldsymbol{K}\cdot\boldsymbol{R}} \, \mathrm{d}\boldsymbol{K} \qquad \text{Equation 16}$$

As the lens aberrations induce a phase shift factor $e^{-i\chi(\boldsymbol{K})}$, the final probe wave amplitude function in real space incident onto the specimen is:

$$P(\boldsymbol{R}) = \int A(\boldsymbol{K}) e^{2\pi i \boldsymbol{K}\cdot\boldsymbol{R}} \, e^{-i\chi(\boldsymbol{K})} \mathrm{d}\boldsymbol{K} \qquad \text{Equation 17}$$

The probe intensity is the squared modulus of the probe amplitude:

$$I(\boldsymbol{R}) = |P(\boldsymbol{R})|^2 \qquad \text{Equation 18}$$

Assuming the specimen is very thin, therefore only a phase shift is introduced when electron waves are passing through, the specimen induced phase shift can be defined as a specimen transmission function:

$$\varphi(\boldsymbol{R}) = e^{i\sigma_i V(\boldsymbol{R})} \qquad \text{Equation 19}$$

Where

$$\sigma_i = \frac{\pi}{\lambda E} \qquad \text{Equation 20}$$

And σ_i is the interaction constant, E is the accelerating voltage and $V(\boldsymbol{R})$ is the potential.

Then, the exit wave function leaving the specimen in real space is:

$$\Psi(\boldsymbol{R}) = \varphi(\boldsymbol{R}) P(\boldsymbol{R}) \qquad \text{Equation 21}$$

This equation is a product of the real space probe amplitude with the specimen transmission function.

In STEM, a detector is placed on the diffraction plane (i.e. reciprocal space) below the specimen; the detected wave function is represented in reciprocal space as:

$$\Psi(\boldsymbol{K}_d) = FT\{\Psi(\boldsymbol{R})\}$$

$$= \int e^{-2\pi i \boldsymbol{K}_d \cdot \boldsymbol{R}} \varphi(\boldsymbol{R}) P(\boldsymbol{R})\, \mathrm{d}\boldsymbol{R}$$

$$= \int A(\boldsymbol{K}) e^{-i\chi(\boldsymbol{K})} \varphi(\boldsymbol{K} - \boldsymbol{K_d})\, \mathrm{d}\boldsymbol{K}$$

$$= P(\boldsymbol{K}_d) \otimes \varphi(\boldsymbol{K}_d) \qquad \text{Equation 22}$$

Denoting the wave vector in the detector plane as $\boldsymbol{K}_d$. This equation shows the convolution of the probe amplitude with the specimen transmission function in reciprocal space.

The intensity on the detector plane is:

$$I(\boldsymbol{K}_d) = |P(\boldsymbol{K}_d) \otimes \varphi(\boldsymbol{K}_d)|^2 \qquad \text{Equation 23}$$

The detected intensity is a function of the position of the diffracted wave vector on the diffraction plane. This is the intensity for a stationary probe on the optic axis.

When the probe scans across the specimen, a second real-space variable $\boldsymbol{R}_0$ is introduced to represent the centre of the probe. Thus the probe amplitude in real space before interacting with specimen in Equation 17 becomes:

$$P(\boldsymbol{R} - \boldsymbol{R}_0) = \int A(\boldsymbol{K}) e^{2\pi i \boldsymbol{K} \cdot (\boldsymbol{R} - \boldsymbol{R}_0)}\, e^{-i\chi(\boldsymbol{K})} \mathrm{d}\boldsymbol{K} \qquad \text{Equation 24}$$

From the equation above, the shift of the probe can be considered as all plane wave components in the probe multiplying a phase factor $e^{-2\pi i \boldsymbol{K} \cdot \boldsymbol{R}_0}$ in reciprocal space. The corresponding detected probe amplitude and simplified intensity expression in the detector plane with scan coordinate $\boldsymbol{R}_0$ becomes:

$$\Psi(\boldsymbol{K}_d, \boldsymbol{R}) = \int e^{-2\pi i \boldsymbol{K}_d \cdot \boldsymbol{R}} \varphi(\boldsymbol{R}) P(\boldsymbol{R} - \boldsymbol{R}_0)\, \mathrm{d}\boldsymbol{R} \qquad \text{Equation 25}$$

$$I(\boldsymbol{K}_d, \boldsymbol{R}) = |\Psi(\boldsymbol{K}_d, \boldsymbol{R})|^2$$

$$= \left| \int e^{-2\pi i \boldsymbol{K}_d \cdot \boldsymbol{R}} \varphi(\boldsymbol{R}) P(\boldsymbol{R} - \boldsymbol{R}_0)\, \mathrm{d}\boldsymbol{R} \right|^2 \qquad \text{Equation 26}$$

The explicit expression for the intensity in the detector plane is the multiplication of the detected probe amplitude with its complex conjugate.

$$I(\boldsymbol{K}_d, \boldsymbol{R}) = \Psi(\boldsymbol{K}_d, \boldsymbol{R}) \Psi^*(\boldsymbol{K}_d, \boldsymbol{R})$$

$$= \int A(\boldsymbol{K}) e^{-i\chi(\boldsymbol{K})} e^{2\pi i \boldsymbol{K} \cdot \boldsymbol{R}_0} \varphi(\boldsymbol{K} - \boldsymbol{K}_d)\, \mathrm{d}\boldsymbol{K} \int A^*(\boldsymbol{K}') e^{-i\chi(\boldsymbol{K}')} e^{2\pi i \boldsymbol{K}' \cdot \boldsymbol{R}_0} \varphi^*(\boldsymbol{K}' - \boldsymbol{K}_d)\, \mathrm{d}\boldsymbol{K}'$$

$$= \iint A(\boldsymbol{K}) A^*(\boldsymbol{K}') e^{-i[\chi(\boldsymbol{K}) - \chi(\boldsymbol{K}')]} e^{2\pi i (\boldsymbol{K} - \boldsymbol{K}') \cdot \boldsymbol{R}_0} \varphi(\boldsymbol{K} - \boldsymbol{K}_d) \varphi^*(\boldsymbol{K}' - \boldsymbol{K}_d)\, \mathrm{d}\boldsymbol{K} \mathrm{d}\boldsymbol{K}' \qquad \text{Equation 27}$$

Where the primes and asterisk denote the corresponding complex variable.

The complete intensity equation for STEM in Equation 27 means that the intensity recorded at each detector position is the interference of all possible pairs of wave components within the incident probe with wave vectors $\boldsymbol{K}$ and $\boldsymbol{K}'$ which are scattered by the sample into the same detecting direction $\boldsymbol{K}_d$.

Only one term $e^{2\pi i (\boldsymbol{K} - \boldsymbol{K}') \cdot \boldsymbol{R}_0}$ contains the probe scanning position $\boldsymbol{R}_0$. This demonstrates that the contrast of the STEM image arises from the oscillation of the phase differences with spatial frequency $\boldsymbol{K} - \boldsymbol{K}'$ as the probe scans. In addition, the larger the size of the probe-forming aperture, the greater the difference of incident probe wave vectors $\boldsymbol{K}$ and $\boldsymbol{K}'$, which results in higher spatial frequency and therefore better resolution. Therefore, the probe-forming aperture size is one of the factors governing the STEM image resolution.

2.3.1. Bright-field imaging

As BF imaging collects on axis transmitted electrons, the detector can be considered as a point detector fixed on optic axis, $\boldsymbol{K}_d = 0$, then $e^{-2\pi i \boldsymbol{K}_d \cdot \boldsymbol{R}}$=1. Deriving from Equation 26, the intensity is:

$$I_{BF}(\boldsymbol{R}_0) = \left| \iint \varphi(\boldsymbol{R}) P(\boldsymbol{R} - \boldsymbol{R}_0)\, \mathrm{d}\boldsymbol{R} \right|^2$$

$$= |\varphi(\boldsymbol{R}_0) \otimes P(\boldsymbol{R}_0)|^2 \qquad \text{Equation 28}$$

This equation is for the scanned bright-field image and the intensity on each point differs as the probe scanning over the specimen. This equation and the similar form of Equation 26 represent the coherent phase contrast imaging in STEM as the specimen transmission function $\varphi(\boldsymbol{R}_0)$ is first convoluted with the probe function $P(\boldsymbol{R}_0)$ before squaring the modulus.

2.3.2. Annular dark field imaging

For an annular detector, starting from Equation 26 and introducing a detector function that has unity over the detector and zero outside, the image intensity becomes:

$$I_{ADF}(\boldsymbol{R}_0) = \int |P(\boldsymbol{K_d}) \otimes \varphi(\boldsymbol{K_d})|^2\, D(\boldsymbol{K}_d) \mathrm{d}\boldsymbol{K}_d \qquad \text{Equation 29}$$

As the detector function has no phase, it can be inserted inside the square to give:

$$I_{ADF}(\boldsymbol{R}_0) = \int |[P(\boldsymbol{K_d}) \otimes \varphi(\boldsymbol{K_d})] D(\boldsymbol{K}_d)|^2 \mathrm{d}\boldsymbol{K}_d \qquad \text{Equation 30}$$

If the central hole of the detector is much larger than the probe-forming aperture, i.e. $\boldsymbol{K}_d \gg \boldsymbol{K}$, (typically the inner detector radius is 3 times larger the aperture radius [16]), the physical meaning is that all electron waves, no matter which wave factor $\boldsymbol{K}$, incident onto the specimen plane have all scattered to high angle $\boldsymbol{K}_d$ in detector plane, then the $\boldsymbol{K}$ dependence of $\varphi(\boldsymbol{K} - \boldsymbol{K_d})$ can be ignored and the detector function can be multiplied with $\varphi(\boldsymbol{K_d})$ to give[15]:

$$I_{HAADF}(\boldsymbol{R}_0) = \int |P(\boldsymbol{K_d}) \otimes [\varphi(\boldsymbol{K_d})D(\boldsymbol{K}_d)]|^2 \mathrm{d}\boldsymbol{K}_d \qquad \text{Equation 31}$$

Converting the integral $I_{HAADF}(\boldsymbol{R}_0)$ to real space with respect to $\mathrm{d}\boldsymbol{R}$:

$$I_{HAADF}(\boldsymbol{R}_0) = \int |P(\boldsymbol{R} - \boldsymbol{R}_0)[\varphi(\boldsymbol{R}) \otimes D(\boldsymbol{R})]|^2 \mathrm{d}\boldsymbol{R}$$

$$= |P(\boldsymbol{R}_0)|^2 \otimes |\varphi(\boldsymbol{R}_0) \otimes D(\boldsymbol{R}_0)|^2 \qquad \text{Equation 32}$$

This is the form for an incoherent image in HAADF mode. The detector function $D(\boldsymbol{R}_0)$ can be thought of as a high pass filter to detect only the sharp features (i.e. atoms) from high-angle components of the specimen transfer function $\varphi(\boldsymbol{R}_0)$. The incoherence is due to probe amplitude function $P(\boldsymbol{R}_0)$ being squared independently before the convolution with $|\varphi(\boldsymbol{R}_0) \otimes D(\boldsymbol{R}_0)|^2$. HAADF imaging does not show contrast reversal and decays monotonically as a function of spatial frequency[16].

2.3.3. Infinite size detector

For an infinite detector, in the case of elastic scattering, $\boldsymbol{K}_d = \infty$, then $e^{-2\pi i \boldsymbol{K}_d \cdot \boldsymbol{R}} = 0$. This condition results in no contrast for detection. This condition can be considered as all interference of electron waves has been summed, which also illustrates the necessity of using an annular detector with a hole in the middle.

3. Energy dispersive X-ray spectroscopy

Energy dispersive X-ray spectroscopy has several acronyms such as EDX, EDXS or XEDS interchangeably used in the literature, or called energy dispersive X-ray analysis (EDXA). In this thesis the acronym EDS is used for consistency. EDS is the result of inelastic scattering of the incident beam with the specimen. Nowadays, EDS is a popular technique to characterise elemental information in specimen using TEM due to the easier acquisition in practice than EELS and straightforward interpretation using commercial EDS software. This section starts with the origin of X-ray emission during electron-sample interaction and illustrates how the generated X-ray signals are detected in TEM. Afterwards, an explanation is given on X-ray detectors, followed by the demonstration of configuration of the detector inside the TEM. The section is concluded with a consideration of both qualitative and quantitative interpretation of EDS spectra.

3.1. Physical origin of X-ray emission

When an incoming electron from the incident beam penetrates through the outer conduction and valence bands of an atom in the specimen, two types of X-rays can be generated: Characteristic X-rays and Bremsstrahlung X-rays. An X-ray can be considered as a photon in its particle nature and an electromagnetic wave in its wave nature.

3.1.1. Characteristic X-rays

Characteristic X-rays are generated in the process of the incoming electron interacting with the inner-shell electrons.

Figure 3-1 illustrates the process of the emission of characteristic X-rays. When the incoming electron ejects an inner shell electron of a specimen atom, the atom has been ionised and leaves a hole in its shell. The hole will be filled by another electron from a more weakly bound shell. This electron transition releases energy, which can occur as the emission of a characteristic X-ray[13].

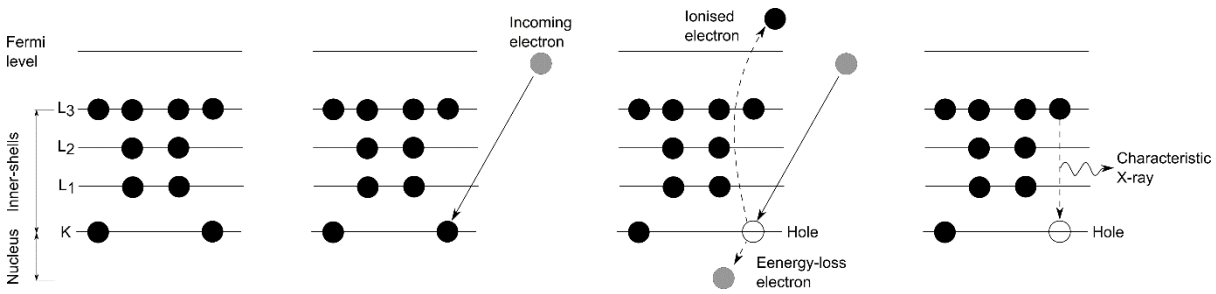

Figure 3-1 Illustration of characteristic X-ray emission process

Because the released energy of characteristic X-rays depends on the difference in the inner-shell energies and is unique to each atomic transition, we use characteristic X-rays to discriminate between elements in the sample. The monotonically decreasing characteristic X-ray wavelength λ_x with increasing atomic number Z is described by Moseley's law[17]:

$$\lambda_x = \frac{B}{(Z - C)^2} \qquad \text{Equation 33}$$

Where B and C are constants.

The energy of characteristic X-rays is also unique to different electron shells in the same atom. A specific X-ray is denoted, for example, as Cu Kα or Cu Kβ. In this denotation, Cu is the atom species, K is the shell where the electron has been ejected to leave a hole and α or β means the K-shell hole is filled by L-shell or M-shell electron, respectively[6]. The complete K, L, M characteristic X-rays are demonstrated in Figure 3-2, but not all these X-rays are detectable in STEM-EDS. Usually we only use K, L, M and α and β X-rays.

In order to generate characteristic X-rays, an inner-shell electron bonded to an atom has to be ionised by an incoming electron beam above a certain energy. This energy is the critical ionisation energy E_c. As atomic number increases, inner-shell electrons are more strongly bound to the nucleus leading to higher E_c for generating characteristic X-rays. However, the energy carried by the generated characteristic X-ray is slightly less than the required critical ionisation energy to generate

the X-ray. These differences are due to the atom is not returned completely to its ground state when the X-ray emitted[6].

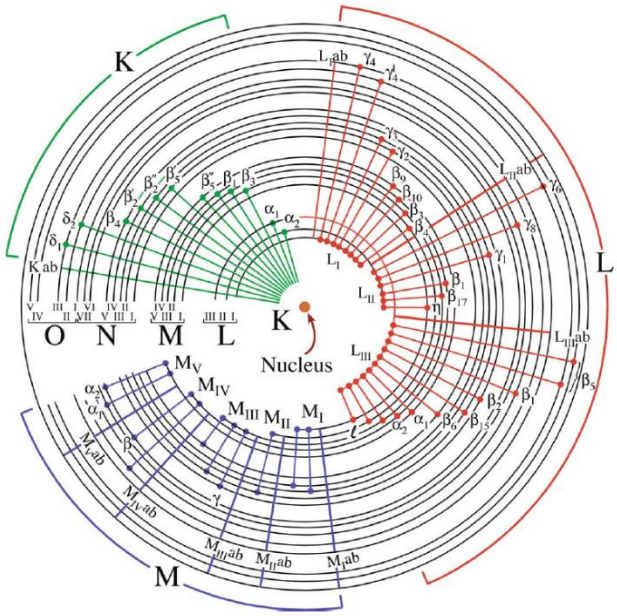

Figure 3-2 All possible K, L and M characteristic X-rays. Reproduced from from [6].

The probability of generating characteristic X-rays firstly depends on the successful ionisation of an atom. Because the ionised atom can also emit Auger electron instead of characteristic X-ray photon, the ratio of generating characteristic X-rays over Auger emissions also needs to be considered[13].

The probability of successful ionisation is described by the ionisation cross section[18]:

$$\sigma_T = \frac{\pi e^4 b_s n_s}{E_0 E_c} \log\left(\frac{c_s E_0}{E_c}\right) \qquad \text{Equation 34}$$

Where n_s is the number of electrons in the ionised subshell, b_s and c_s are constants for that shell.

Equation 34 shows the probability to generate an X-ray depends on the ratio of beam energy E_0 and critical ionisation energy E_c. This ratio is usually more than 5 as $E_0 > 100\ keV$ and $E_c < 20\ keV$[6].

The probability of generating characteristic X-rays over Auger emissions is described as fluorescence yield[19]:

$$\omega = \frac{Z^4}{a + Z^4} \qquad \text{Equation 35}$$

Where a is a constant for the ionised shell.

This equation demonstrates the significant dependence of characteristic X-ray intensity on the atomic number. So there is not much characteristic X-rays to detect for light elements and using EELS is preferred.

3.1.2. Bremsstrahlung X-rays

Bremsstrahlung X-rays, translated from German to English is "braking radiation", also named as background or continuum X-rays, are generated when the incoming electron completely penetrates the sample atom's electron shells and interacts with the Coulomb field of the nucleus. During the interaction, the incoming electron suffers a substantial change in momentum and may emit bremsstrahlung X-rays. Unlike the characteristic X-rays that the same atom only generates characteristic peaks at certain energies, bremsstrahlung X-ray can be generated in a wide range of energy, therefore bremsstrahlung X-rays usually cannot be used to discriminate elements. The intensity of bremsstrahlung X-rays, N, as a function of their energy E is commonly described by Kramers' law[20]:

$$N(E) = KZ\frac{(E_0 - E)}{E} \qquad \text{Equation 36}$$

Where K is Kramers' constant.

The theoretical bremsstrahlung X-ray intensity therefore can be described as a hyperbola function of E. At low X-ray energy range, smaller than ~2 keV, the calculated bremsstrahlung X-ray intensity is very high (as demonstrated as the dashed line in Figure 3-3). But this part of bremsstrahlung X-rays tend to be absorbed by specimen and detector materials, which results in a rapid drop of the detected bremsstrahlung to 0 (shown on the left of the Figure 3-3 as the solid lines.) As the X-ray energy increases and approaches the beam energy E_0, the chance to generate bremsstrahlung X-

rays decreases to 0. This anisotropic emission bremsstrahlung X-ray behaviour also means that EDS is more suitable to detect high Z elements where their characteristic X-rays are easier distinguished from the low background bremsstrahlung X-rays.

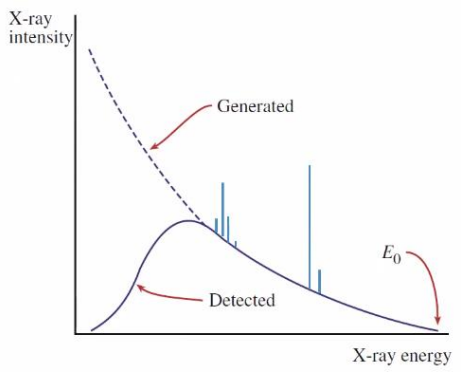

Figure 3-3 The bremsstrahlung X-ray intensity as a function of energy. Reproduced from [6].

3.2. Procedures to detect the X-ray signal in TEM

When an X-ray photon enters the EDS detector made by semiconductor materials, the X-ray energy generates electrons within the semiconductor. These electrons in detector materials transfer from the valence band to the conduction band and create electron-hole pairs. The number of generated electron-hole pairs is proportional to the energy of the incoming X-ray. Typically, thousands of electron-hole pairs are generated from one incoming X-ray photon since the energy required for creating electron-hole pairs in Si is ~3.8 eV while the energy carried by the characteristic X-ray is usually above 1 keV[6]. After the creation of electron-hole pairs, the detector utilises an internal bias voltage to separate electrons and holes. The separated electrons result in a charge pulse, which is proportional to the incoming X-ray energy. The charge pulse is then converted to a voltage, enters a field-effect transistor (FET) preamplifier and is amplified and digitised. The finally digitised voltage is computed as one count for one incoming X-ray and this count is registered on the spectrum at the according X-ray energy.

When a collection of X-rays hits the detector, it requires processing time to allow the detector electronics to go through all the procedures abovementioned to digitise X-ray photons to counts on the spectrum. During the processing, the detector rejects any other incoming X-rays and therefore this processing time is also named as “dead time”. For a given time interval, for example, a dwell time that the beam stays on one pixel before it moves to another, dead time increases as count rate increases. We should aim to maximise count rate if energy resolution is not the concern.

The above procedures only demonstrate the detection of one emission event of an X-ray photon. As the focused electron beam scans through an imaging area pixel by pixel, few to thousands of atoms (in 1-100nm) in the volume of the specimen at each pixel position can be ionized and emit X-ray photons, which results in the detection of many X-ray counts. Each count representing the same or different X-ray energies has been registered on the EDS spectrum accordingly. The final digitalised EDS spectrum at each pixel is a histogram of counts (on y-axis) versus energy (on x-axis), and “energy” is also digitalised as “channel” and normally each channel represents 5 or 10 eV.

Recently, EDS data collection has shifted from point or line scan acquisition to spectrum imaging (SI). SI collects the full EDS spectrum at each scanned pixel, forms a 3D data cube for the mapping region where the third dimension is X-ray energy range. SI enables the complete data collection and the flexibility to analysis data after collection. The part of this advance is due to the higher EDS collection efficiency made by larger detectors[21], so EDS detectors are described in the next section.

3.3. Detectors

Two mostly used detectors for EDS are Si(Li) detector and silicon drift detector (SDD) (Figure 3-4). The main part (middle grey area in Figure 3-4a) of the Si(Li) detector is made by Si with Li doping[22]. The Li doping produce intrinsic Si region with equal intrinsic electron and holes. So any additional electron or holes contributed by the incoming X-rays can be truthfully detected[6]. However, at the front and back side of the Si(Li) crystal the doping is not complete and may have to be covered by additional coating. Therefore, the front and back side of the detector act as dead layers to reduce

detector efficiency[6]. Another drawback inherent in Si(Li) detector design is the large anode (red region in Figure 3-4a) as it covers the whole back region of the detector. The large anode has large capacitance and leads to much slower throughput of counts than SDD[23]. Thermal noise is also more severe on large anode designed detector than it is for small anode SDD design. Liquid N_2 cooling can alleviate the thermal noise problem but could form ice or hydrocarbon contamination layer on the front face of detector[6].

The SDD detector consists a large n-type Si crystal, concentric p-type Si rings and a small n-type anode. The major advance of SDD is the much smaller anode compared to Si(Li) detectors for charge collection [23 24], which reduces thermal noise and release the necessity of liquid nitrogen cooling[25]. In addition, the ring-like design of SDD enables a larger cathode to collect more incoming X-rays while maintains a small anode in the centre of concentric rings[26], enables a much higher count rate output than Si(Li). Typically SDDs are thinner compared to Si(Li), however, it drops its detection efficiency when detecting X-ray energies above 10 keV [27]. Easier manufacturing of SDD leads to the development of larger detector with collection angle of π sr[28], annular detector [29] or multiple detectors systems [30,31] that also advances the total EDS detection efficiency.

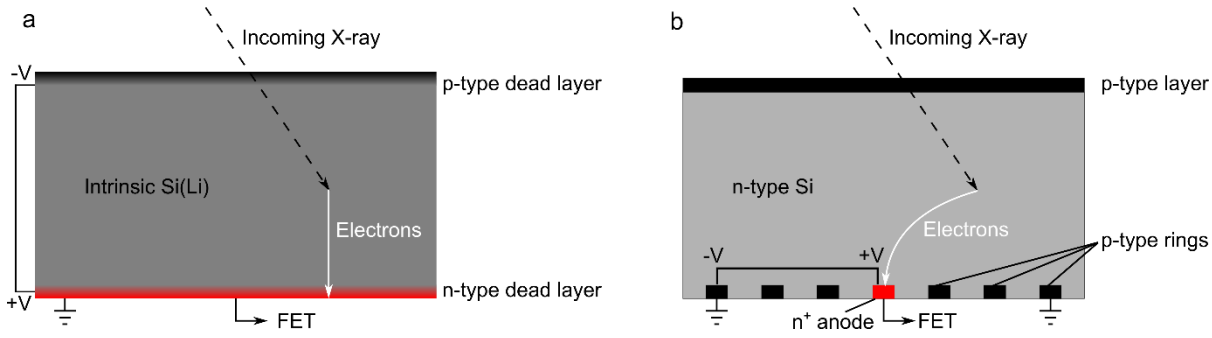

Figure 3-4 Schematic cross sections of EDS detectors. a) Si(Li) detector. b) SDD detector.

The collection angle is the most important factor to assess detector performance. Detector collection angle is the solid angle subtended at the analysis point on the specimen by the detector area[6]. X-rays are generated isotropically over a whole sphere. Therefore, an ideal detector should collect all signals on this sphere and has a collection solid angle of 4π sr. However, the collection

angle Ω is constrained by the size of the detector A and the distance between the detector and sample A as $\Omega = \frac{A}{S^2}$. A larger detector could be beneficial to increase the collection angle. Since the free space in which the detector can be placed is mainly limited by the gap between the upper and lower pole piece, a larger detector usually requires a larger pole piece gap to retain the same detector-sample distance. Multi-detector systems are another way to increase total collection angle [30,31]. For example, Thermo Fisher's ChemiSTEM technology uses four standard SDDs positioned on four corners of the polepiece and separated by 90°. The four-detector design increases the total collection solid angle to up to 0.9 sr. In addition, as Cs-corrected STEM becomes more popular, increasing the pole piece gap will not significantly reduce resolution, which allows larger detectors to be fitted closer to the specimen [7].

3.4. Qualitative interpretation

Although EDS has fairly high signal-to-background ratio for heavy elements and the qualitative identification of the presence of elements is straightforward, it is possible to misidentify spurious X-rays as new findings. Therefore, the common artefacts present in EDS analysis are introduced here.

3.4.1. EDS detector induced artefact X-rays

Dead layers in the EDS detector are a source for various artefact EDS peaks. If the part of incoming X-ray is blocked by the dead layer, it is called incomplete charge collection (ICC) and distorts perfect symmetric Gaussian peaks to an asymmetric peak with a tail at the low energy side. ICC happens especially on low energy X-rays and on Si(Li) detectors with thick dead layers.

If the incoming X-rays fluoresce dead layer materials (mainly Si), it results in a small Si Kα peak in the final spectrum, named as the internal fluorescence peak. For a long acquisition time, there is always a Si K peak appearing eventually, but a thin dead layer for SDD should minimise the issue.

If the incoming X-rays have higher energies than detector materials' critical ionisation energy (e.g. Si), they can excite the intrinsic region of the detector and generate secondary Si Kα X-rays (1.74 keV).

When these small amounts of secondary Si Kα X-rays escape outside the dead layer and have not been collected by the detector, the original high energy X-rays will register its peak to a lower energy position to form an escape peak (1.74 keV lower for Si Kα detector). Thin dead layers on SDD in this case, however, is a disadvantage. Modern EDS acquisition/processing system should identify the lower energy escape peak and re-register it to its mother peak energy.

The sum peak may appear at twice the energy of the major peak if the electronics cannot discriminate two incoming photons, especially when dead time is too high (over 60%)[6].

3.4.2. Post-specimen artefact X-rays

As electrons pass through the optic axis in the microscope, not only the specimen but also other parts of microscope materials may be excited to form X-rays or electrons to be detected as false X-ray signals.

Stray X-rays, usually due to the interaction of the beam and the condenser apertures, fluoresce the high energy peaks more efficiently (high K/L ratio). A thick 'top-hat' shape aperture will reduce stray X-rays. Stray electrons coming from the poorly collimated electrons will excite low-energy peaks (low K/L ratio). Carefully choosing a C2 aperture to define beam and a C_S-corrector will minimise this effect.

Various sources of spurious X-rays can also be generated from post-specimen scattering. High angle backscattered electrons could strike the holder (Cu), the polepiece (Fe, Co), detector (Si and Pb) and the X-ray collimator (Zr), as well as the specimen away from the target analysing point to form specimen-characteristic spurious X-rays. Bremsstrahlung X-rays produced in the specimen will also fluoresce specimen and grid bar, especially at high tilt angle when perform tilt-series tomography. A wider pole piece gap and removing the cold finger tend to reduce the post-specimen scattering problems[6].

3.5. Quantitative interpretation

The quantification of STEM-EDS spectrum from a thin sample could provide sample composition and could achieve near atomic resolution[32]. There are two common methods used for EDS quantification in CTEM/STEM: the Cliff-Lorimer k-factor method[33] and the Zeta-factor method[34]. Before introduce these methods, two important features of characteristic peaks for quantification, peak intensity and spectrum background are discussed below.

3.5.1. Intensity

The detected intensity of the characteristic X-ray signal for element A can be described as the multiplication of the total number of electrons incident on the sample (D_e, i.e. beam current), the ionisation probability of one electron incident on the sample($n_A t Q_A$), fluorescence yield (ω_A), relative transition probability (a_A, i.e. relative line weights of α or β lines within the families) and total detection efficiency ($(\frac{\Omega}{4\pi})\varepsilon_A$) [13]:

$$I_A = D_e \cdot n_A t Q_A \cdot \omega_A \cdot a_A \cdot (\frac{\Omega}{4\pi})\varepsilon_A \qquad \text{Equation 37}$$

For the ionisation probability, the n_A is the density of atoms of element A within the sample, t is the sample thickness and Q_A is the ionisation cross section. For the total detection efficiency, Ω is the detector collection solid angle and ε_A is the detector efficiency.

3.5.2. Background subtraction

All intensities used for quantification are the integrated characteristic peaks on the EDS spectrum, which means the peak has to be separated firstly from the background bremsstrahlung. EDS background subtraction methods can be categorised into three: simple window-based, mathematical filtering and physical modelling.

The simple window-based method first identifies the characteristic peak region with a window and a defined width on the energy axis. Then two background regions on both sides of the peak have been

picked, integrated intensities of the background windows are averaged and subtracted from the integrated intensity of the peak region. If the characteristic peaks are not overlapping and the background is not changing dramatically, for example the high energy characteristic peaks, this simple method works fairly well.

As characteristic peaks show rapid variation on the spectrum and background varying slowly, a 'top-hat' kernel can be convolved with the original spectrum to separate peaks and background[35]. The result is the second derivative of the original spectrum, with background intensity around 0 and the peak shape is almost unchanged but shifted vertically to negative values. Although negative values presented in the filtered spectrum has no physical meaning.

Modelling background using Kramers' law in Equation 36 and superimpose it with Gaussian-shaped characteristic peaks fits a smooth curve to the complete spectrum. This modelling is particularly useful if overlapped peaks require deconvolution and for low SNR spectra[36].

Advanced methods for background-peak separation include using multivariant statistical analysis (MSA)[37]. MSA involves scaling the spectrum to fulfil some statistical noise distribution assumption, followed by an eigenanalysis[37,38]. After MSA processing, spectrum can be represented by few linearly independent components to either reduce noise[39] or describe specimen compositions[40]. For example, variants of MSA, the chemical components of Co@Fe_3O_4 core-shell nanoparticle has been successfully identified from EDS SI data without prior knowledge of nanoparticle chemistry[40]. But debate of using MSA for EDS quantification is ongoing[41]. The heavily processed spectrum is perhaps no longer quantitatively interpretable due to the physical nature of the signal and may not meet the mathematical requirements for MSA[41].

3.5.3. K-factor quantification method

Cliff and Lorimer's quantification method uses the intensity ratio of elements to calculate the weight fraction of the corresponding elements[33]. The ratio approach cancels out any variations in the microscope (historically the beam current is the major instability). For example, if there are two

elements of interest A and B, with known intensities (I_A and I_B), the weight percentages of both elements (C_A and C_B) can be calculated using Equation 38:

$$\frac{C_A}{C_B} = k_{AB}\frac{I_A}{I_B} \qquad \text{Equation 38}$$

$$C_A = \frac{k_{AB}I_A}{I_B + k_{AB}I_A}$$

$$C_B = \frac{k_{AB}B}{I_A + k_{AB}I_B}$$

The key term here is the Cliff-Lorimer k-factor k_{AB}. The k-factor is not a constant and relative to the combination of any two elements, it can be determined either by experiments or by calculation from first principles. We usually determine a list of k-factors for all elements by comparing to a standard (e.g. Silicon k_{si}) as:

$$k_{Asi} = \frac{k_A}{k_{si}} \qquad \text{Equation 39}$$

$$k_{AB} = \frac{k_{Asi}}{k_{Bsi}}$$

The experimental determination of k-factors is the most accurate way[42]. In theory, the method requires multiple multi-element thin samples with known composition (C_A, $C_B, etc.$) to work out the unknown k_{AB} after measuring intensities (I_A, $I_B, etc.$) from microscope. In practice, however, tedious repeated measurements and careful precautions such as sample thinning mean this method is rarely used.

The calculated k-factors via Equation 40 are widely used although they are not as accurate as experimental determined values[37].

$$k_{AB} = \frac{(Q\omega a\varepsilon)_B A_A}{(Q\omega a\varepsilon)_A A_B} \qquad \text{Equation 40}$$

Where subscripts denotes elements A and B, A_A is the atomic weight of element A.

The Equation 40 demonstrates that k-factor varies with accelerating voltage (affects Q), atomic numbers (affects ω, a and A) and detector (affects ε).

3.5.4. Zeta-factor quantification method

As modern microscopes have much more stable beam currents, the Zeta-factor approach have gained increasing interest[34,43,44]. This approach assumes the mass-thickness (ρt) of the thin film sample is proportional to the characteristic X-ray intensity of an element A normalised by the composition and the total number of electrons incident on the sample[34,43], as Equation 41:

$$C_A = \zeta_A \frac{I_A}{\rho t D_e} \qquad \text{Equation 41}$$

$$C_A = \frac{\zeta_A I_A}{\zeta_A I_A + \zeta_B I_B}$$

$$C_B = \frac{\zeta_B I_B}{\zeta_A I_A + \zeta_B I_B}$$

$$\rho t = \frac{\zeta_A I_A + \zeta_B I_B}{D_e}$$

Where ρ is the sample density.

The major advantage of zeta-factors when performing experimental determination is it only requires pure-element reference sample with known thickness rather than a multi-element standard, therefore the well-established pure-element standard approach developed for bulk analysis in the electron probe microanalyser can be applied [34]. In addition, the mass-thickness map (ρt) can be simultaneously measured using Equation 41.

The theoretical expression of ζ_A is given in Equation 42:

$$\zeta_A = \frac{A_A}{N_V \frac{\Omega}{4\pi} (Q\omega a\varepsilon)_A} \qquad \text{Equation 42}$$

Where the only new parameter N_V is Avogadro's constant. If we take the ratio of ζ_A and ζ_B and combines with Equation 40, the following equation shows the relationship between k-factor and zeta-factor[34]:

$$\zeta_A = k_{AB}\zeta_B \qquad \text{Equation 43}$$

This relationship permits the conversion of a series of k-factors into zeta-factors by measuring only one zeta-factor, such as a standard Si K.

4. Three-dimensional reconstruction using STEM

4.1. Introduction to principles of 3D reconstruction from 2D projections

As an electron beam passes through a 3D specimen, information about the specimen parallel to the electron beam direction is integrated and therefore images collected in the STEM are only 2D projections of the 3D object. If the specimen consists of complex structure, a single 2D projection may not be able to reveal the real 3D configuration, this is where 3D reconstruction plays a role.

The first few examples of using TEM to do 3D reconstruction was demonstrated on biological macromolecules at late 1960s [45]. The earlier works of the 3D reconstruction starts from the idea of demonstrating a set of montage images collected from different views of the same specimen [46]. Subsequently, the 3D structure of the tail of bacteriophage T4 has been reconstructed [47]. Although in this work only one electron micrograph was used for reconstruction due to a helical symmetry imposed, De Rosier and Klug detailed general principles of obtaining a 3D structure without high symmetry [47] by tilting and imaging the same specimen multiple times. This method is nowadays often referred to as electron tomography (ET), or TS-ET.

However, as the biological specimen are sensitive to electron beam, using TS acquisition scheme, the same specimen sees electron multiple times and suffers more beam damage or lower SNR per frame. Idea of averaging many identical macromolecules were developed to alleviate these issues for better images by taking advantage of facts that many macromolecules are identical [48–50]. Thus, as these identical macromolecules are randomly orientation on a support, imaging them only once results in a collection of projections from different view which can be 3D reconstructed. This approach has been referred to as single particle reconstruction (SPR), or single particle analysis.

Nowadays, in physical science, TS-ET is still the mainstream for 3D reconstruction probably because not many repeated identical specimens were available and physicists are more interested to unique phenomenon. Whilst SPR are predominantly used in structural biology and cryo-EM community. Nevertheless, both techniques share common principles of using 2D projections to reconstruct the 3D information of the object.

The mathematical principles of projecting a 3D object to a set of 2D projections is established by Radon back in 1917[51]. Radon transform describes the relationship between an n dimensional object and its n-1 dimensional projections. For example, for a 2D object $f(x, y)$, its 1D projections projected from any direction L can be described as the Radon transform R of the 2D object, i.e. Rf, which is the line integral through the projection direction L.

$$Rf = \int_L f(x, y) ds \qquad \text{Equation 44}$$

Where ds is the unit length of L.

After Radon transformation, i.e. forward projection, the Cartesian coordinate system (Figure 4-1 a) of the original object in the form of (x, y) becomes a Radon coordinate system (Figure 4-1 b) in the form of (l, θ), and a point in Cartesian space becomes a "sine-form" line in Radon space described as $l = rcos(\theta - \varphi)$, which is often termed as sinogram. The angle θ is usually termed as "projection angle".

Extending the abovementioned example to 3D space, the projection direction L can be explicitly described as (θ, ψ, ω), or altitude, azimuth and in-plane rotation angles (illustrated in Figure 4-1 c). For a single axis TS-ET, the tilt axis of the object is fixed on the x-y plane, the projection direction can be described use only one angle θ, which is usually recorded by microscope goniometer. By contrast, for SPR, as each particle is randomly oriented, to describe its projection direction requiring to obtain all three altitude, azimuth and in-plane rotation angles.

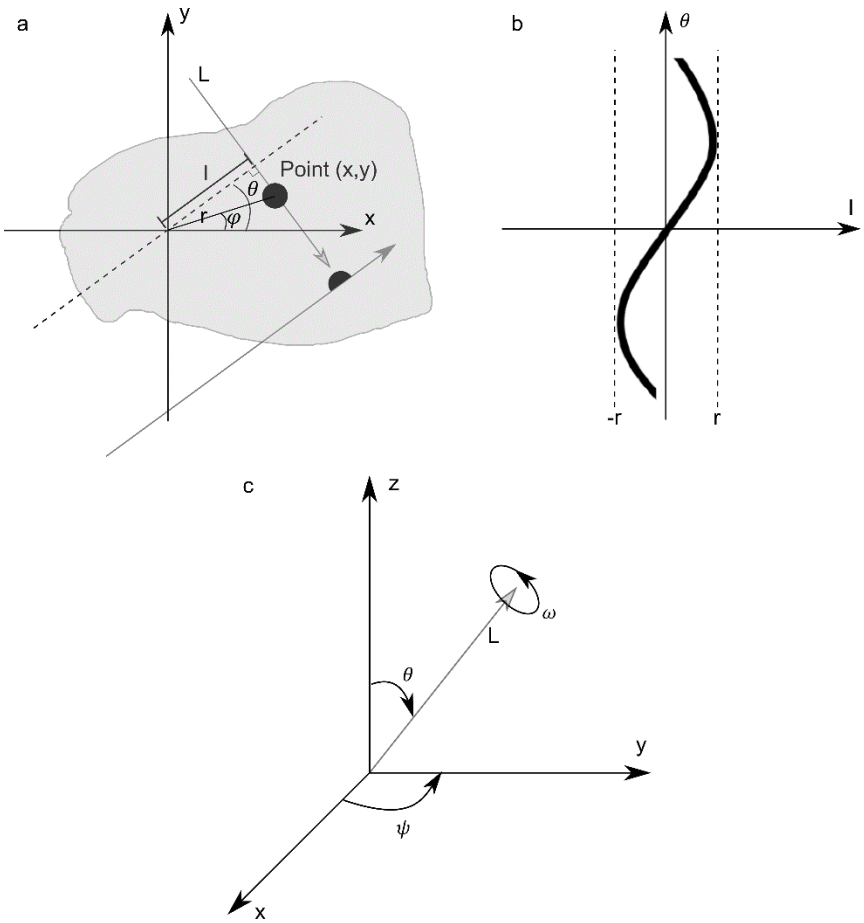

Figure 4-1 Schematic of a small dot in (a) Cartesian coordinates becomes a sinogram in (b) Radon space. (c) Three angles explicitly describe a projection direction in 3D real space.

The Radon transform that describes forward projection process from a n dimensional object to a n-1 dimensional projection is a real space operation. The Fourier slice theorem[52] (also termed as "projection slice theorem" or "central section theorem") extends the operation to Fourier space. The theorem states that a projection of an object from a projection angle is mathematically equal to a slice in the 3D Fourier transform of that object at the same angle.

4.1.1. Backprojection

As Radon transform and Fourier slice theorem implied, the 3D reconstruction from a set of 2D projections can be considered as an inverse Radon transformation or perform the inverse 3D Fourier transform if the Fourier space were filled by slices of the Fourier transform of the 2D projections.

The former is named real space backprojection and the latter is name direct Fourier space reconstruction.

During real space backprojection, intensity in each pixel on every projection image has been linearly added into a 3D volume along a ray at same forward projection direction. As many rays from different directions backprojected and intercepted at 3D, possible locations of the original objection can be revealed (Figure 4-2 a-c).

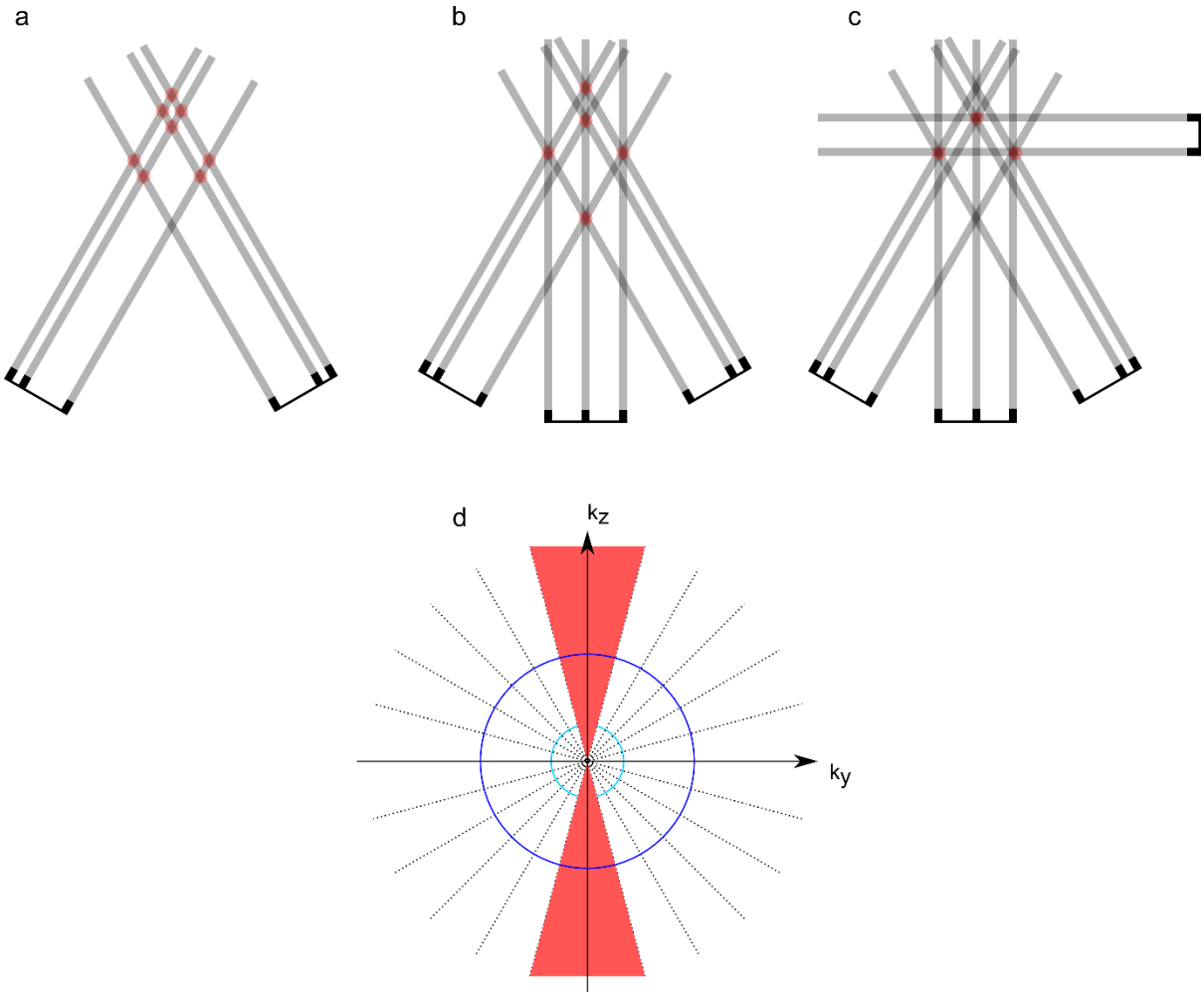

Figure 4-2 Illustrations of backprojection and Fourier central slice theorem. (a-c), backprojection using different number of projections to reconstruction object. (d) Fourier central slice and the missing wedge is shown in red. Light blue circle indicate oversampling region while dark blue circle region is under-sampled.

In Fourier space, if there is more space to be filled by Fourier slices of the 2D projections, the quality of the reconstruction will be improved (Figure 4-2 d). The filling slices in Fourier space also demonstrates two phenomenon: 1) space that is not filled by slices account for reconstruction artefacts, especially the “missing wedge” of information at high tilt in TS-ET results stretching of the reconstruction at same directions; 2) more space is filled at low frequency (close to the origin of Fourier space) than high frequency, which results oversampling at low frequency and under sampling at high frequency. A simple backprojection reconstruction without considering this nonuniform sampling would results blurred final reconstruction. Therefore, a ramp filter acted as a weighting function is often applied to either the Fourier space of 2D projections or to the final reconstruction. This method is known as weighed backprojection (WBP).

Simultaneous iterative reconstruction technique (SIRT) is one of the mostly used reconstruction method[53]. In this method, at each iteration, all experimental projections are compare with the corresponding reprojections from the reconstruction to provide differences at each orientation, then these differences are averaged, backprojected and multiplied with previous reconstruction for next iteration until there is no noticeable difference between reprojections and experimental projections. The precedent algebraic reconstruction technique (ART) only calculates the difference between experimental projection and reprojection at one orientation and update this difference to recalculate the reconstruction before next iteration [54]. SIRT usually outperforms ART at the presence of small amount of noise[54].

4.1.2. Advanced reconstruction techniques

The Radon transform and its inverse transformation assume intensity of the 3D object is linearly integrated onto 2D projection. A more general assumption for 3D reconstruction, also known as projection requirement, is that the projection intensity should be at least a monotonic function of some property of the 3D object. This assumption usually holds for HAADF [55], EDS [56] and EELS [55] signal. Nevertheless, altering the linear Radon transform to a non-linear model based transformation allows

more accurate reconstruction[57], for examples, utilising knowledges of experimental signal generation parameters for atomic HAADF 3D reconstruction [58], absorption correction for EDS tomography [59] and excitation of surface plasmons for EELS tomography [60].

As data acquisition for 3D reconstruction is discrete, as well as in certain conditions projections can be presented as only a number of intensity values [61], such sparse nature can be explored to utilise compressive sensing based reconstruction [62,63] to reduce tilt range [64] or produce more faithful reconstruction [65].

The oversampling in low frequency reciprocal space can explored to minimise the interpolation between real and reciprocal space during iterative refinements to increase reconstruction quality [66], which algorithm also demonstrate atomic resolution 3D reconstruction for TS-ET data [67,68].

4.2. Data acquisition

4.2.1. TS-ET

Tilt-series electron tomography is usually performed by rotating the specimen holder around a single axis and acquires one image at each tilt angle, with tilt range typically around ±50° to ±80° and angular increments between 1° and 10°.

The region of interest for TS-ET usually remains smaller than the field of view, so only one image needs to be taken at each tilt. When wider specimens are imaged (the width perpendicular to tilt axis and beam direction), at high tilt angle the regions away from tilt axis suffer more focus change. A dynamic focus mode varies focus as beam scan from over focus region to under focus region would be helpful for this situation [69]. Another way to increase the size of the region of interest, without losing resolution, is to perform a small tilt range TS-ET on each sub-region. This method is recently be applied on a two-dimensional MoS_2 materials and achieved 3D atomic resolution[70]. But this method may be only applicable to 2D materials as it requires the specimen is thin enough so the TS-ET performed on adjacent regions is not shadowed.

The maximum tilt range is limited by the combination of location of sample on the TEM grid, the spacing between TEM grid bars, the holder geometry and space between polepieces of the microscope [56]. If the maximum tilt range is exceeded, either the holder will touch the polepieces or a reduction of detected signals [56]. Excepting these hardware limits, the maximum tilt range and angular increments are mainly limited by the beam tolerance of the specimen and the available microscope session time. For a fixed dose budget, the reconstruction quality is found to exhibit no significant difference by either by reducing pixel dwell time or beam current to acquire low SNR image per tilt or increase tilt angular increments [71]. Despite this claim from recent research, the choice of reconstruction algorithm may also effect the choice of tilt angular increments and dose per tilt image. If the reconstruction algorithm is designed to enhance low SNR images [64], finer tilt annular increments but low dose per tilt image may be outperformed than other reconstructions.

Standard single tilt holder has limited maximum tilt range smaller than ±90° results in an artefact in reconstruction termed as “missing wedge” problem [72]. Special holders such as a dual-axis tilt holder can reduce the “missing wedge” to “missing pyramid” [73]. Combining an on-axis tomography holder with a needle shaped sample can achieve a full 180° rotation [74,75].

In addition to equally spaced angular increments, varied tilt steps are also reported such as using smaller tilt increments at high tilt angles [76] or using equally-sloped angular increments [77,78]. But these methods have not been widely used, perhaps due to the questionable reconstruction quality improvements [79] versus practical difficulties of varying tilt steps.

In STEM, HAADF, EDS and EFTEM/EELS are three main signal types and all of them have been explored for the 3D imaging of nanoparticles using TS-ET method. Therefore each imaging mode is outlined in next three sections.

4.2.1.1. Imaging mode: HAADF

When TS-ET initially gain attention by the field of material science, the use of BF-TEM signals (used for TS-ET in biology) had been realised to be unsuitable for many crystalline materials specimens due to diffraction contrast. Instead, HAADF signal with highly monotonic intensity relationship to atomic number demonstrates it advantage of more truthful reconstruction in TS-ET [55,80,81]. HAADF TS-ET was first used to study the interior mesopores in heterogeneous catalysts [55,80], then extended to the identify the embedded heavy metal nanoparticles on a light element support [80,82,83]. Because the Z-contrast mechanism of HAADF signal, distinguish high Z metal nanoparticles from low Z support in HAADF TS-ET is relatively easy even with the presence of reconstruction artefacts. This leads to the widespread qualitative use of HAADF TS-ET to identify the relative location between loading nanoparticles and its support. This study has covered a wide range of supported nanocatalysts including carbon [84,85], silica [86,87], alumina [88] and titania [89,90]. HAADF TS-ET can also be used to qualitive identify the existence of discrete elemental segregation, such as characterising core-shell [91] or Janus nanoparticles [92]. Quantitative interpretation of HAADF TS-ET including indexing the exposed

nanoparticle facets [93,94], surface area [95] and dispersion [96]. Combined with the state-of-art microscope, sophisticate image processing and advanced reconstruction algorithm, atomic resolution HAADF TS-ET were also realised [67,68,97–99].

4.2.1.2. Imaging mode: EDS

.HAADF TS-ET is usually limited to distinguish two well separated elements while EDS TS-ET has potential to characterise more elements simultaneously as long as sufficient signals were collected. EDS TS-ET is also efficient for thick specimens while HAADF TS-ET often assume a standard “thin foil” thickness. As tilting to high angle, increased effective specimen thickness up to three times in the beam direction are further enhance the utility of EDS TS-ET.

However, the usage of EDS TS-ET has not been widely reported until last five years. The major practical difficulty is that the EDS detector are heavy shadowed by the penumbra of the holder when tilted [56,100]. Conventional single EDS detector designs usually mount the detector slightly above the specimen and the most efficient EDS acquisition are achieve by tilting the holder to 15°-20°. The varable EDS collection efficiency at other tilts, combined with small EDS detector solid angle restricts the quality of TS data collected in earlier works [100].

The low detection efficiency of EDS signals also results the usage of high electron dose and long acquisition time. Developments in both hardware and software are ongoing to alleviate these issues since the first report of EDS TS-ET on FeAl alloy buried with yttrium and zirconium nanoparticles [100].

Larger detector or multiple detector designs [30,31] increase the total collection solid angle from 0.1 – 0.3 sr to 0.7 – 0.9 sr, which in general is beneficial to all EDS acquisition usages and not limited to TS-ET. Specifically for EDS TS-ET, the symmetric multiple detector design prevents the severe loss of detected counts when tilting the holder to the opposite direction of the detector. High brightness electron source and aberration corrector increase beam current without loss of resolution again increases EDS signal to background. Slater et al. shows that if detector efficiency at each tilt angle can be experimentally measured, applying this calibration to vary acquisition time while tilting

specimen could results same counts for each tilt and better reconstruction [56]. Advanced reconstruction algorithms such as compressive sensing [63] or hybrid reconstruction [101] utilising simultaneously acquired HAADF and EDS signals can reduce beam damage and acquisition time and increase reconstruction quality, which are discussed further in previous section.

Except the usage of EDS TS-ET in semiconductor industry to detail the chemistry on transistors [102–104] and to inform failure analysis [105], EDS TS-ET is becoming well recognised in chemical science. Earlier applications of EDS TS-ET on nanoparticles were used to identify elemental segregation for a single nanoparticle [106,107]. Later, more researches are focus on imaging multiple bimetallic nanoparticles as synthesised or tested at different conditions to link the elemental segregation to different synthesis routes [108,109] or sample compositions[110], or oxidation conditions [111,112]. Quantitively interpreting EDS intensity as atomic percentage are also demonstrated on a CdZnO nanowire [44] and metal-organic framework [113].

4.2.2. SPR

Single particle reconstruction relies on averaging many identical but randomly oriented units to enhance SNR and to provide a mean 3D structure for a whole population or a subgroup of the population. SPR are predominantly used for imaging biological specimens inside cryogenic electron microscopes (cryo-EM). The biological specimen is highly sensitive to electron beam, a common dose limit for damaging specimen is about 10-30 e^-/Å[114], thus usually 10^5 to 10^6 individual macromolecules were imaged and average to obtain high resolution images while not destroy individual repeating units. As many sample preparation techniques used for SPR are less relevant to material science specimens and non-cryo TEMs, thus these steps are only brief introduced and this section is mainly focused on common techniques have potential to be applied on material science.

Before imaging a specimen in an electron microscope, macromolecular objects are usually first purified through a biochemical means to increase conformation and composition homogeneity [115]. Then the purified specimen maintained in water is deposited on TEM grid, a tweezer holds the grid

to allow a “plunge-and-freeze” into liquid nitrogen to freeze specimen and vitrify water solution to amorphous ice layer [115,116]. The frozen macromolecules maintain their fully hydrated form and then reduce radiation damage from electron beam. The vast majority of SPR works utilise BF-TEM signals as it is more dose efficient than STEM signals. BF-TEM images of macromolecules usually highly defocused to increase the visibility of each particle and ease the later image processing such as particle finding and classification [117]. As hundreds of thousands particles need to be collected, automated image collection is key for a modern SPR workflow. Many software packages are available to integrate with microscope for automated acquisition [118]. The automated software works intuitively and iteratively through the following steps: 1)begin with capturing low magnification survey images to including many squares on TEM grid; 2) zoom in to intermediate magnification to identify holes on the support carbon film; 3) further zoom in to single particle resolvable magnification to capture images where particles stay on the hole to avoid support film; 4) move to next region and record image, until the movement beyond the size of previously captured position, then go back to previous magnification and redo the procedures.

Recently, the development of direct electron detector (DED) enables the detection of a single electron [119]. Such superior detective quantum efficiency comparing to CCD camera revolutionise the resolution of SPR works [120,121]. The use of DED not only dramatically improve image quality, but also allows a stack of images to be recorded instead of a single image using same amount of electrons so movement of molecules during acquisition can be aligned and corrected for afterwards [122]. Adding a phase plates at the back focal plane of the objective lens can also be used to increase image contrast without introducing defocus [123], but practical alignments still remain difficult [124]. Beside the majority use of cryo-TEM and bright field signals, using cryo-STEM and ADF signals for SPR has recently demonstrate the ability to detect Zn and Fe atoms in protein[125].

Other averaging based techniques rooted in cryo-EM community for 3D reconstruction of biological units including random conical tilt [126] and subtomogram averaging [127] (or termed as single particle

tomography [128]). Random conical tilt is similar to SPR but imaging same region twice, one at 0° tilt and another at high tilt. By finding particles with same azimuth and altitude orientation but different random in-plane rotation in first tilt image, the paired particle at second tilt can be arranged as a conical tilt series covers the complete 360° range with random azimuth angle. An extension to this method named orthogonal tilt reconstruction [129], which imaging same region twice at ±45° so the angle range of the "missing wedge" inherent in the random conical tilt method is reduced from 90° minus the high tilt angle to 0°. Subtomogram averaging performs a full tilt series for a field of view containing many identical particles and averaging the 3D reconstructed particles into one. Because particle orientations determined in these two methods do not require any presumption or searching, they are often used to create ab initio 3D model for SPR.

4.3. Data alignment

4.3.1. TS-ET

During the acquisition of TS data, the region of interest usually undergoes translational shifts in the plane perpendicular to the beam, which is the image shift alignment issue. In addition, the tilt axis may not coincide with the central line of the imaged region, which is the tilt axis alignment issue.

To align image shift, for a single axis TS-ET data, the most straightforward way is to perform cross correlation between two adjacent tilts as they are the most similar image pair. Middle tilt image or 0° tilt image is often used as a reference, and cross correlation of neighbouring images proceeds to both side of the tilt directions[130]. A "common line" method can also be used to align image shift[131], which utilises the Fourier slice theorem that a common line can be found on all Fourier form of 2D projections if they come from a same 3D object. Another kind of image shift alignments is based on fiducial markers [132] that is commonly used for biological specimen due to low contrast and low SNR of the as-collected TS images. In additional to abovementioned major issue of rigid translational shifts, non-rigid deformation of images such as shearing due to the sample drift during STEM acquisition could also be corrected[133].

For tilt axis alignment, a commonly used method is using an iterative manner to minimise "arc" artefacts present on slices of the quick 3D reconstruction at each iteration[134]. As demonstrated in Figure 4-3, if the tilt axis is misaligned, the reconstruction shows smearing artefacts and inspecting these arcs from three slices can be used to indicate tilt axis misalignments. If the tilt axis is shifted (Figure 4-3 b,c), all three arcs will present on the tilt axis shifted side. If the tilt axis is rotated, middle slice will not show significant arc feature but arcs will present on the opposite side of left and right slices.

It is also reported that downshifting background intensity [135,136] or applying a mask on 2D projections [71] reduces the contribution of background intensities to the reconstruction increase the final reconstruction quality.

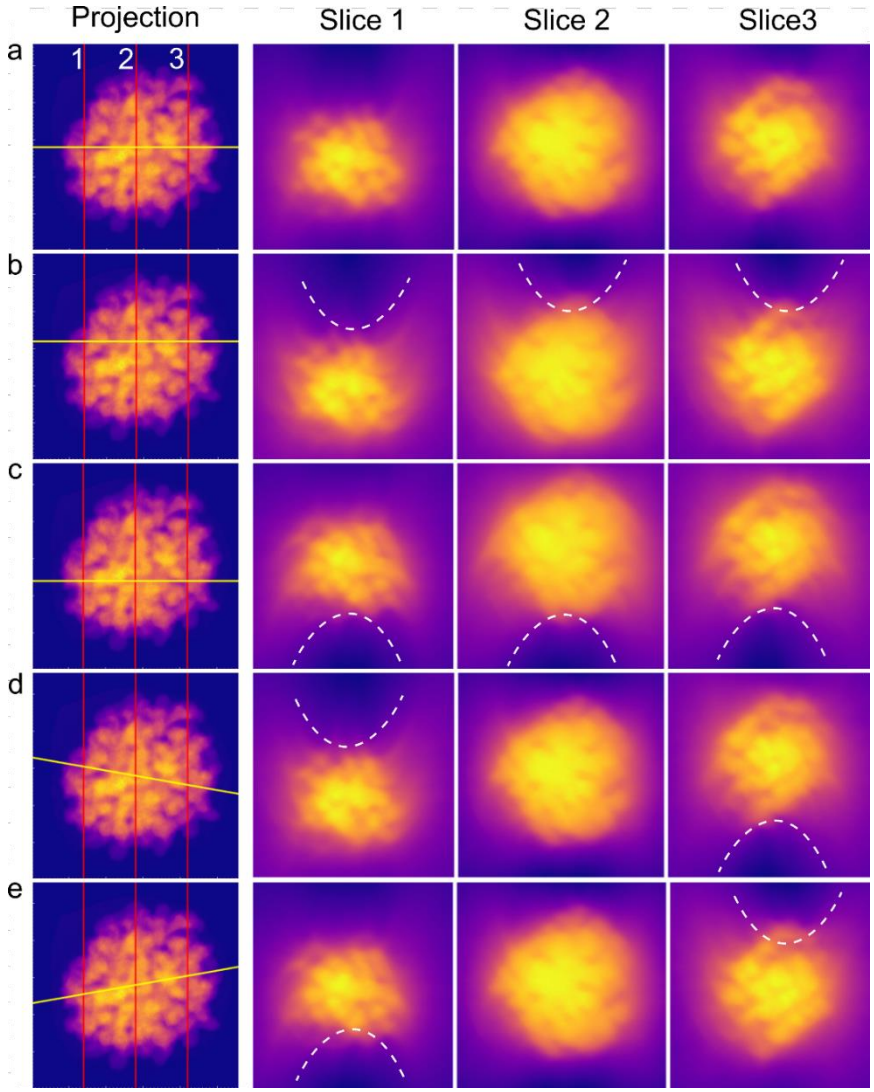

Figure 4-3 Illustration of the tilt axis alignment method. (a) Tilt axis well aligned. (b) Tilt axis shifted 20 pixels. (c) Tilt axis shifted -20 pixels. (d) Tilt axis rotated 10°. (e) Tilt axis rotated -10°. In projection column, yellow lines represent tilt axis and green lines represent slice positions. In slice columns, dashed white curve represent arc artefacts indicating the tilt axis misalignments. The sample represented here is a 30 nm Pt nanoparticle, supplied by Dr Chris Batchelor-McAuley (University of Oxford)

4.3.2. SPR

After acquisition of thousands images containing hundreds of thousands individual particles, firstly all particles need to be selected into small boxes (usually few hundreds of pixels in width) so later image processes are performed on each small images that containing ideally only one particle. Then, all particles are grouped into classes according to the similarity so particles in each class represent the same projection from a unique orientation. All particles within the same class are then averaged to enhance SNR and the averaged images are used to search orientation angles for the 3D reconstruction. Each of these procedures is detailed in the next few sections.

4.3.2.1. Particle picking

In the as-collected micrograph, hundreds of "good" particles may present, but "bad" particles showing fracture parts and non-macromolecular objects such as contamination are also present, as well as plausible particles that are unsure whether it is a good particle imaged at rare orientations or a bad particle. Methods to select individual particles from micrographs can be done in manual, semi-automated or fully automated manner.

In very early works, where only tens to hundreds of particles were used for averaging, manual selection is used [137]. A trained eye can outperform many automated algorithms to discriminate particles from non-particles, but human may focus on more familiar views and omit less presented orientations.

In semi-automated approaches, software or algorithms pre-pick particle candidates and leave human to judge whether or not to include the candidate as a particle for further study. The initial pre-picking is usually done by simple contrast enhancement on particles such as using low-pass filtering [138] or the difference of Gaussian filtering [139] to bring the intensity of particles above background and set a threshold value to accept the region if its intensity above the threshold.

Fully automated approaches often combines classification with statistical analysis to reject picked region if it only contains features not exist on true particles [140–142], or utilises template-based

matching to select particles match simulated projections from a known low resolution 3D model [143–145].

4.3.2.2. Classification

Picked individual particles show low SNR and require averaging many well-aligned identical particles to boost SNR for 3D reconstruction.

Most classification methods use multi-reference alignment [146–148] based on the principle of k-means clustering. The method runs iteratively as following: 1) select k number of initial templates; 2) align all particles to each template and assign particles to their most similar template group; 3) update templates by averaging all particles assigned to them and repeat the previous step until each group show maximum dissimilarity. Many variants of clustering methods are also explored to increase performance [149,150], in particular to alleviate a "group collapse" problem, which cause low SNR images in a less populous group to be wrongly assigned to a high SNR template and eventually the less populous groups are not recognised.

4.3.2.3. Assign orientation

Because all particles are randomly oriented, the position of each particle projection respect to its 3D structure can be described by five parameters: azimuth angles, altitude angles, in-plane rotation angles, X translational shift and Y translational shift. After classification, two translational shifts are aligned and the remaining three unknown parameters define the orientation used for 3D reconstruction. Solving orientations for each averaged image is based on an iterative projection matching between averaged images and reference projections generated from an initial 3D model.

The projection matching can be considered as an variant of the k-means algorithm [151]: k number of initial templates are k number of projections from initial 3D model; and updating templates can be done by reconstructing a new 3D model and re-generating template projections. The iteration stops if a metric of quality of the reconstruction do not improve. Such assessments of reconstruction quality are detailed in the next section 4.4.

The initial 3D model can be obtained by experimental methods such as random conical tilt and subtomogram averaging methods described in section 4.2.2, or by computational approaches. In extreme case, random orientations can be assigned to experimental images to produce an initial 3D model [152–154], then iteratively improve orientation assignments by template matching experimental images with new generated projections from the 3D model and update assigned orientations and 3D model. But this approach is high computing expensive and time consuming.

Another branch of projection matching is based on maximum likelihood [155–157]. During orientation assignment, each experimental image is not assigned by only one orientation but a set of orientations with weighting factors based on the similarity between experimental images and templates. The maximum likelihood estimation could overcome the bias introduced by a starting reference [117,155] but requires more computing power.

4.4. Resolution for 3D reconstruction

The resolution for 3D reconstruction is depending on many factors. In materials science and applications of TS-ET, the ultimate minimal resolve distance for a simple backprojected reconstruction derived by Crowther [52] is:

$$d_x = d_z = \frac{\pi D}{N} \qquad \text{Equation 45}$$

Where d_x is perpendicular to the tilt axis and d_z is parallel to beam direction, D is the diameter of the reconstructed volume and N is the number of projections.

However, due to "missing wedge" problem along the beam direction, minimal resolvable distance d_z is elongated by a factor e_{xz} as a function of the maximum tilt angle θ_{max} [72]:

$$e_{xz} = \sqrt{\frac{\theta_{max} + sin\theta_{max}cos\theta_{max}}{\theta_{max} - sin\theta_{max}cos\theta_{max}}} \qquad \text{Equation 46}$$

For a maximum tilt angle of 75°, d_z is elongated by a factor of 1.2. However, when reconstruction is performed by iterative methods such as SIRT or other advanced reconstruction techniques, this elongation values can only serve as an estimation and direct measurement of the size of minimal resolvable features on the finial reconstruction should be used [97,158,159].

In the field of biology and the reconstruction using SPR approach, resolution is often tested by a approach named Fourier shell correlation (FSC) [160,161]. In order to perform FSC, raw data of thousands of particles should be split in two halves and perform independent reconstructions for both halves. Then in the 3D Fourier space, from low frequency to high frequency, the shell of two half reconstructions are cross correlated and the similarity is plotted as a function of frequency in reciprocal space. When the similarity falls below an arbitrary threshold such as 0.5, the frequency at this similarity level is considered as the reconstruction resolution. Despite its simplicity in theory and

the widespread use, debating is ongoing such as the choice of the similarity threshold [162], using single representative value versus a 3D threshold volume [163,164].

5. Imaging 3D elemental inhomogeneity in Pt-Ni nanoparticles using spectroscopic single particle reconstruction

5.1. Introduction

The work presented in this chapter demonstrates the first realisation of utilising SPR approach on inorganic nanoparticles in combination with EDS spectroscopic signals for 3D elemental quantification. Compared to conventional tilt series EDS tomography, the new spectroscopic SPR approach presented here results two orders of magnitude reduction of electron fluence imaged on the specimen. The spectroscopic SPR approach reveals PtNi nanocatalysts possess a Pt-rich core, a Ni-rich hollow octahedral intermediate shell and a Pt-rich rhombic dodecahedral skeleton framework with less Pt at <100> vertices.

Dr Sarah Haigh and Dr Thomas Slater conceived the idea and supervised the project. Dr Thomas Slater and I acquired the HAADF-STEM and EDS data presented in this chapter. Dr Gerard Leteba and Dr Candace Lang synthesised nanoparticles. Dr Alan Roseman advised on the preliminary SPR reconstruction results and commented on final manuscript. Dr Christopher Race wrote preliminary python scripts and I modified his scripts to visualise the atomic arrangement of PtNi nanoparticles presented in Figure 4 in this chapter. Dr Neil Young and Dr Angus Kirkland performed preliminary TEM characterisation and results are shown in this chapter. Dr Sarah Haigh, Dr Thomas Slater and I cowrite the manuscript. The rest of the work demonstrated in this chapter has been done by myself.

The results of this project were published in Nano Letters in 2019. The original manuscript for "Imaging 3D elemental inhomogeneity in Pt-Ni nanoparticles using spectroscopic single particle

reconstruction" is presented below. The associated supplementary information is provided directly following the manuscript.

Publication details: Wang, Y. C., Slater, T.J., Leteba, G.M., Roseman, A.M., Race, C.P., Young, N.P., Kirkland, A.I., Lang, C.I. and Haigh, S.J., (2019). Imaging Three-Dimensional Elemental Inhomogeneity in Pt–Ni Nanoparticles Using Spectroscopic Single Particle Reconstruction. *Nano Letters,* 19(2), 732-738. (DOI: 10.1021/acs.nanolett.8b03768)

Paper: Imaging 3D elemental inhomogeneity in Pt-Ni nanoparticles using spectroscopic single particle reconstruction

Yi-Chi Wang[1], Thomas J A Slater[1, 2], Gerard Leteba[3], Alan M Roseman[4], Christopher P Race[1], Neil P Young[5], Angus I Kirkland[2, 5], Candace Lang[6], Sarah J Haigh*[1]*

1. School of Materials, University of Manchester, Oxford Road, Manchester, M13 9PL, U.K.

2. Electron Physical Sciences Imaging Centre, Diamond Light Source Ltd., OX11 0DE, U.K.

3. Catalysis Institute, Department of Chemical Engineering, University of Cape Town, Corner of Madiba Circle and South Lane, Rondebosch 7701, South Africa

4. School of Biological Sciences, Faculty of Biology, Medicine and Health, University of Manchester, Oxford Road, Manchester, M13 9PL, U.K.

5. Department of Materials, University of Oxford, Parks Road, Oxford, OX1 3PH, U.K.

6. School of Engineering, Macquarie University, NSW 2109 Australia

Keywords: three dimensional reconstruction; single particle reconstruction; PtNi nanoparticle catalysts; energy dispersive X-ray spectroscopy; surface segregation; scanning transmission electron microscopy

Abstract

The properties of nanoparticles are known to critically depend on their local chemistry but characterising three dimensional (3D) elemental segregation at the nanometre scale is highly challenging. Scanning transmission electron microscope (STEM) tomographic imaging is one of the few techniques able to measure local chemistry for inorganic nanoparticles but conventional methodologies often fail due to the high electron dose imparted. Here, we demonstrate realisation of a new spectroscopic single particle reconstruction approach built on a method developed by structural biologists. We apply this technique to the imaging of PtNi nanocatalysts and find new evidence of a complex inhomogeneous alloying with a Pt-rich core, a Ni-rich hollow octahedral intermediate shell and a Pt-rich rhombic dodecahedral skeleton framework with less Pt at <100> vertices. The ability to gain evidence of local surface enrichment that varies with the crystallographic orientation of facets and vertices is expected to provide significant insight towards the development of nanoparticles for sensing, medical imaging and catalysis.

Nanoparticles (NPs) are crucially important in many scientific fields, from inorganic particles[1,2] in catalysis, plasmonics and medical imaging, to proteins[3] in cellular processes. These nanoparticles may have complex morphologies and compositional disorder, both of which contribute to their properties. Electron microscopy is a valuable tool to characterise the structure and chemistry of individual NPs. However, conventional (scanning) transmission electron microscope ((S)TEM) imaging measures two dimensional (2D) projections of 3D objects, which often prevents the interpretation of complex 3D elemental distributions because chemical information is integrated in the third dimension.

There are several established acquisition schemes for 3D characterisation of individual NPs in the (S)TEM.[4–13] Tilt-series electron tomography (ET), in particular, has become a common acquisition

method in 3D imaging for materials science. The tilt-series ET approach is similar to X-ray computed tomography (CT); it requires multiple images of the sample viewed along different directions, which are then reconstructed to create a 3D distribution of some property of the object. Beyond characterising 3D morphology, ET based approaches have the ability to map elemental distributions and other physical properties, such as localised surface plasmons,[7] when STEM imaging is combined with spectroscopic techniques such as energy dispersive X-ray spectroscopy[14–16] and electron energy loss spectroscopy.[17,18] However, tilt-series ET-based approaches require repeated imaging of the same area, which often results in a high cumulative electron dose and may cause the technique to fail for even moderately beam sensitive samples. The total fluence required, the number of electrons per square area of the sample, is dependent on the required resolution. The typical electron fluence used for high angle annular dark field (HAADF) tomography, is about 10^6 electrons/Å^2 for a spatial resolution of the order of 1 nm (Supporting Information Table S1). The requirement for high electron fluence is even greater when elemental information is required, with typical requirements for STEM-EDS tomography[14,15] often exceeding 10^8 electrons/Å^2 for a similar spatial resolution (Table S1). Although, for some materials electron beam damage can be reduced or eliminated by imaging with a low accelerating voltage or low electron flux, the majority of specimens are found to have a critical electron fluence above which the specimen is permanently damaged. As (S)TEM instrumentation has improved, the instability of specimens under prolonged electron irradiation is often the principal obstacle to 3D imaging.

Organic biological structures such as proteins and viruses are typically many orders of magnitude more sensitive to the electron beam than common inorganic specimens. Acquiring 3D information for such highly beam sensitive objects requires an approach termed single particle reconstruction (SPR),[19–26] which combines the information from single images of many thousands of individual objects. This technique assumes that all the objects being imaged are identical but are randomly orientated on a support. The great importance of this approach was recognised with the awarding of the Nobel prize for Chemistry in 2017,[20] but single particle reconstruction approaches have not yet

been successfully applied to spectroscopic STEM data. Here, we demonstrate that by modifying the SPR approach to use STEM-EDS spectrum images rather than conventional (S)TEM data sets, we are able to recover quantitative 3D elemental information with a resolution of ~1 nm. This is achieved with an electron fluence per particle that is 500 times lower than would be required to achieve the same results using conventional STEM-EDS ET techniques (2×10^6 compared to 9×10^8 electrons/Å^2, Table S1).

Application of spectroscopic SPR to catalytic nanoparticles. We have applied our new approach to reconstruct the mean 3D elemental distribution for a population of bimetallic rhombic dodecahedral platinum-nickel (PtNi) NPs (Figure 1 a-d) which are amongst the most active oxygen reduction reaction (ORR) catalysts ever designed[1]. These NPs are too electron beam sensitive for conventional tilt-series electron tomography at a resolution on the order of 1 nm, so previous (S)TEM studies of the material have been limited to 2D elemental mapping.[27–32] Platinum is one of the most effective and widely used catalytic materials, with extensive applications in fuel cells, catalytic converters and batteries[1,2]. Alloying Pt NPs with a second metal, such as Ni, has been shown to improve activity/durability for the ORR and hydrogen evolution reaction (HER),[1,2,33,34] in addition to reducing cost. Despite the importance of these materials, the mechanism for these improved properties is still not well understood, hindering attempts to maximise catalytic efficiency and in-service lifetime. Key to understanding the mechanism of PtNi NP performance is the ability to characterise elemental surface segregation and specific faceting behaviour. Studies of elemental segregation in individual NPs have been largely restricted to 2D (S)TEM spectrum imaging,[27–32] due to the tendency of these NPs to alter their structure when subjected to high electron dose. We have independently measured the critical dose for electron beam damage in the PtNi nanoparticles used in this study, and found that they have restructured after an electron dose of approximately 5×10^7 electrons/Å^2 (See supplementary Fig. S6). This beam sensitivity precludes the use of a STEM-EDS tilt series tomography approach, which we have found requires an electron fluence on the order of 9×10^8 electrons/Å^2 to achieve an appreciable EDS signal to noise ratio (SNR) at 1 nanometre

resolution (Supplementary Table S1). For our spectroscopic SPR approach we have employed a total electron dose (2×10^6 electrons/Å^2, Methods and Supplementary Table S1) 25 times lower than the measured critical dose for each nanoparticle (5×10^7 electrons/Å^2), which ensures that the original morphology and compositional distribution of the NPs remain the same after data acquisition (Fig. S6, and Table S1).

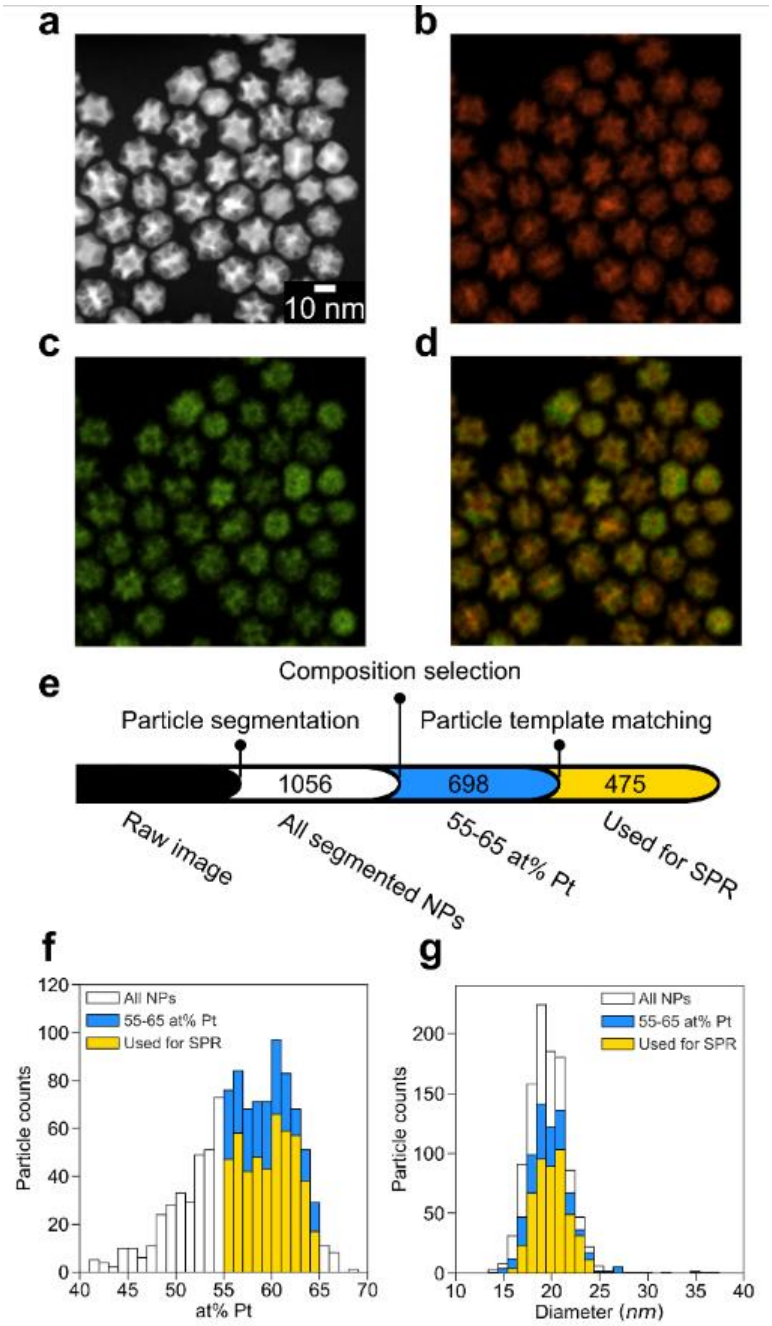

Figure 1 Overview of the PtNi NP population and quantification of specimen homogeneity. a, Representative STEM-HAADF image of the PtNi nanoparticles together with elemental maps for **b,** Pt

(Lα), **c,** Ni (Kα) and **d,** Pt + Ni extracted from STEM-EDS spectrum images. **e,** The sequence of image processing steps used to separate and identify nanoparticles to be used in the SPR reconstruction. Colours correspond to those used in histograms **(f** and **g)** and numbers correspond to the number of NPs remaining after each step. **f,** Compositional distribution of the PtNi NP population calculated by k-factor EDS quantification. **g,** Feret diameter distribution for the same particles. In **(f)** and **(g)** yellow bars represent the NPs that were matched with the ET template and used in final SPR reconstruction, blue bars include the NPs that were compositionally selected (limited to a range of 55-65 at% Pt) but not matched to a projection and white bars represent all segmented NPs in the raw data that were not included in the other two sets.

Quantification of nanoparticle population homogeneity. To perform spectroscopic single particle reconstruction, STEM-HAADF and STEM-EDS images were simultaneously acquired for over one thousand PtNi NPs as the beam is scanned pixel by pixel. As the probability of generating characteristic X-rays (and of these X-rays being detected) is much lower than the probability of an electron scattering onto the HAADF detector, the signal-to-noise ratio (SNR) of the STEM-EDS elemental images is lower than the HAADF image data set. However, the direct, one-to-one correlation between the pixels in the two data sets allows the high SNR HAADF images to be used for particle identification and segmentation of both data sets (for a full description see Methods).

Inorganic nanoparticles are typically less homogenous in size and shape than proteins and viruses, so selection criteria need to be applied to prevent outliers from deteriorating the quality of the single particle reconstruction. Analysis of the size and composition of our PtNi NPs showed unimodal distributions with a diameter of 20 nm ± 2 nm and composition of 56 ± 6 at% Pt (mean ± standard deviation; Figure 1 f-g, and Table S2). The majority of the NPs (698 of 1056) have a composition of 55-65 at% Pt (blue bars in Figure 1 e-g) so this subset was chosen to demonstrate our spectroscopic SPR approach. However, we note that for a bimodal or inhomogeneous nanoparticle population it is possible to perform several different reconstructions for different classes of nanoparticle, where these different classes are distinguishable in the 2D data on the basis of the particles' size, shape or

composition. To illustrate this we have separately performed a SPR reconstruction for NPs in the population with a lower Ni content (compositions of 45-55 at% Pt, see Figs. S16 and S17).

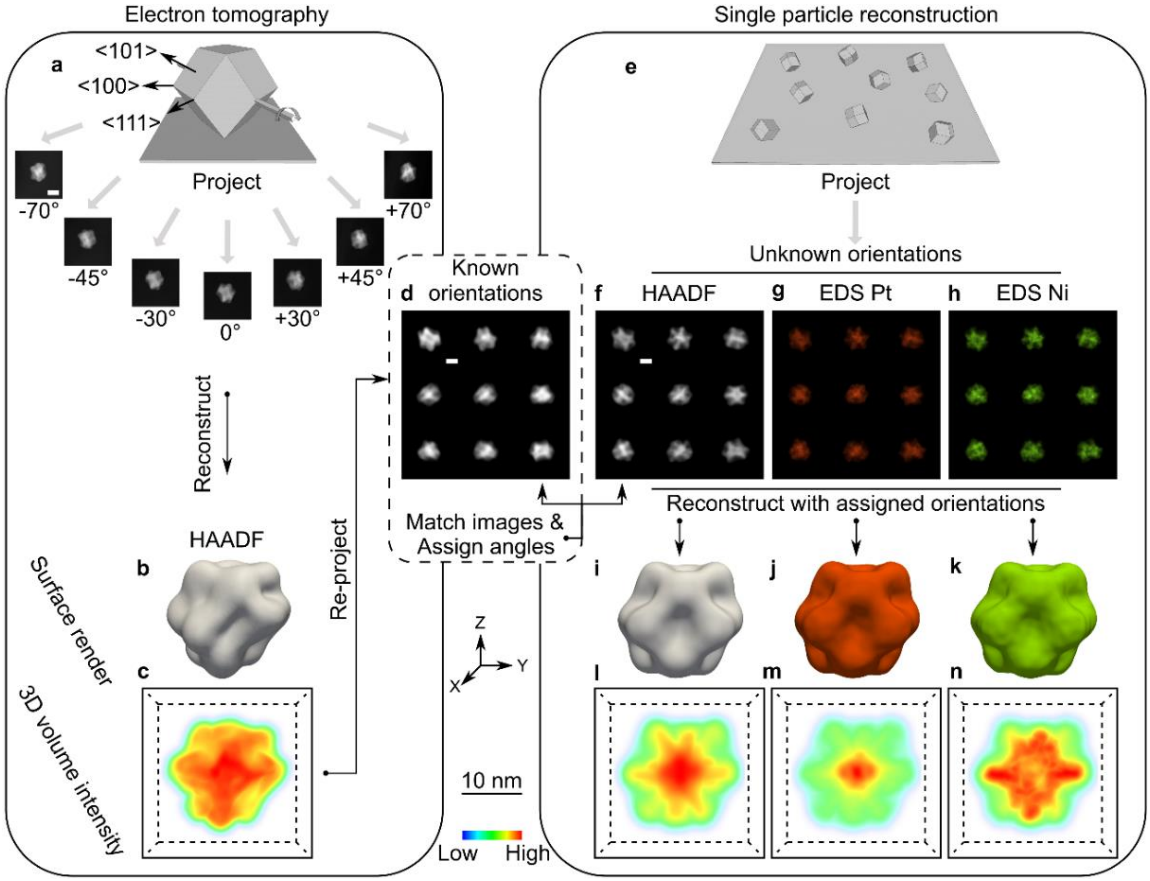

Figure 2 Workflow for spectroscopic single particle reconstruction. a, Schematic showing the acquisition of a traditional STEM-HAADF tilt-series tomography data set for one NP. **b** and **c,** Surface render and 3D volume intensity for the ET reconstructed HAADF signal, respectively. **d,** Re-projections with known orientations obtained from the reconstruction in **(b)** and **(c)** (9 illustrative examples are shown from 400 re-projections). **e,** Schematic of the SPR data acquisition (single images of many identical NPs with random orientations on a support film). **f,** Experimental SPR HAADF-STEM images are matched to the re-projections in **d** so as to assign known orientations. **g and h,** EDS Pt and EDS Ni signals are assigned the same known orientations as have been assigned to their simultaneously acquired STEM-HAADF data in **(f)**. **i-k** are surface renders and **l-n** are 3D volume intensities for SPR reconstructed HAADF, EDS Pt and EDS Ni 3D intensity distributions, respectively.

Grey, red and green colours in **(b)** and **(i)-(k)** represent HAADF, EDS Pt and EDS Ni signals, respectively. In **(c)** and **(l)-(n)**, the rainbow colour scaling from blue to red represents the signal intensity from minimum to maximum. Pixel values in **(g)** and **(h)** and reconstructed voxel values in **(j), (k), (m)** and **(n)** are EDS counts. All scale bars are 10 nm.

Spectroscopic single particle reconstruction workflow. The workflow we have developed for spectroscopic SPR from STEM-EDS data is illustrated in Figure 2. Initially, a conventional STEM-HAADF tilt-series ET data set is reconstructed for a single PtNi particle (Figure 2a and b, full details in Methods and Videos S1-2). The 3D electron tomography reconstruction serves as an initial morphological estimate that can be used to produce STEM-HAADF re-projections with known orientations (Figure 2c). The SPR input is a large data set of simultaneously acquired STEM-HAADF and STEM-EDS images in which the nanoparticle orientations are unknown. Orientations can be assigned to each nanoparticle in the SPR data by cross correlating the ET STEM-HAADF re-projections (Figure 2c) with the SPR STEM-HAADF experimental images (Figure 2e, Figs. S10-14). Once the orientations are known it is then possible to reconstruct 3D HAADF and EDS intensities (Figure 2 h-j and Videos S3-5).

Size analysis of the 475 SPR NP images matched to the ET re-projections showed that these particles possess the same distribution of diameters as the overall particle population, offering an initial validation of the matching process (matched particles are yellow and overall population is white in Figure 1 e-g). The use of an initial HAADF tilt-series tomographic reconstruction speeds up the processing, and a similar approach has been used in conventional SPR where a low resolution protein structure resolved by X-ray crystallography can be employed as an initial estimate for the SPR reconstruction.[3,22] Nevertheless, most inorganic nanoparticles are likely to possess a general geometric shape,[1,2,27–32] which could be used as the initial estimate for SPR,[24] particularly for nanoparticles that prove too beam sensitive for ET tilt-series acquisition.

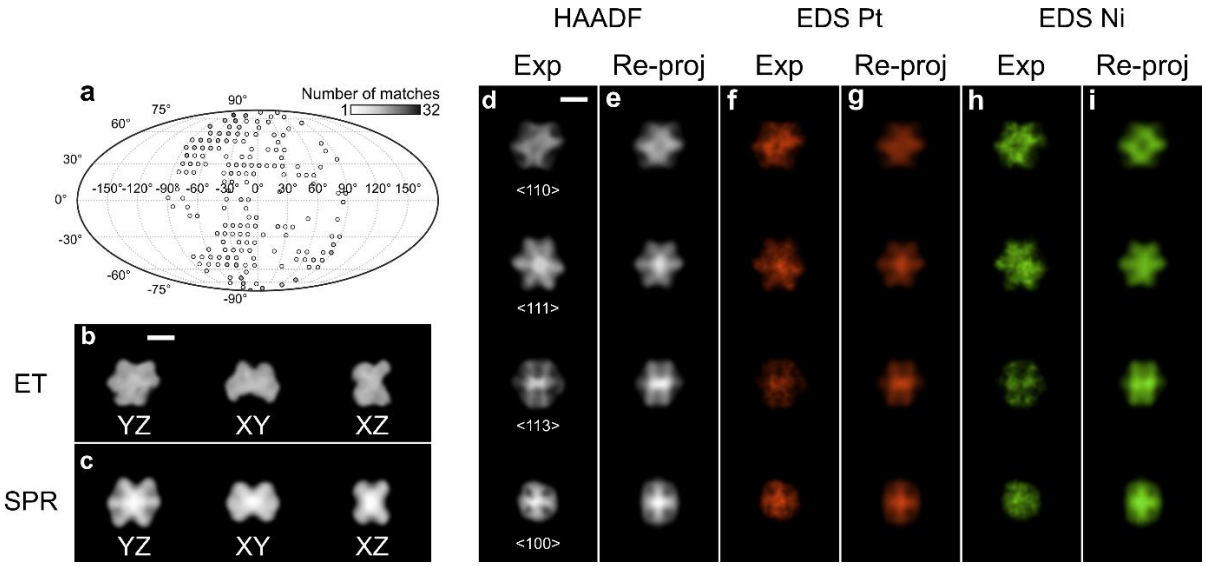

Figure 3 Verification of the fidelity of spectroscopic SPR. a, Distribution of matched nanoparticle orientations used for SPR. **b** and **c,** Orthoslices of YZ, XY and XZ planes from ET and SPR HAADF reconstructions respectively. The coordinate axes with respect to the 3D reconstructions are shown in Figure 2. **d, f, h** Experimental HAADF images and Pt or Ni elemental maps extracted from STEM-EDS spectrum images, respectively. **e, g, i,** Re-projections generated from SPR reconstructions for HAADF STEM image, and Pt or Ni elemental maps, respectively. In **(d-i),** images are acquired along approximately <110>, <111>, <113> and <100> crystallographic directions. Scale bars are 10 nm.

Verification of the fidelity of the spectroscopic single particle reconstruction. To confirm the accuracy of the orientation assignment, we perform a tilt-pair analysis for 53 NPs at 0° and 30° tilt angles (see Methods). The orientations of these tilt-pair particles were assigned using the same cross-correlation procedures applied in spectroscopic SPR reconstruction. The angular differences between untilted and tilted images were calculated based on the assigned orientations, which had a mean of 29° ± 8° (mean ± standard deviation), in good agreement with the nominal goniometer tilt angle of 30° (details in Methods and Figs. S8 and S9). The large standard deviation in orientation assignment is due in part to the 5° angular sampling interval used for the re-projections from the ET reconstructed template. The orientations display nearly complete angular coverage (Figure 3a), minimising the potential for reconstruction artefacts due to the presence of a restricted tilt range in

ET (commonly known as the 'missing wedge' problem; Fig. S5). A qualitatively good match between the perimeter shapes of orthoslices obtained from ET and SPR suggests the SPR has accurately reconstructed the morphology of the PtNi NPs (Figure 3 b, c). The differences observed between the SPR and ET reconstructions are likely to be due to the SPR reconstruction being an ensemble average of hundreds of NPs, while the ET reconstruction is a single 'representative' nanoparticle. In addition, comparison of experimental images and re-projections generated from the SPR reconstruction show a qualitatively good agreement for both HAADF images and elemental maps (Figure 3 d-i). The high similarity of this comparison indicates that neither the NP population heterogeneity after size and composition selection, or the few non-matched orientations affect the reconstruction quality. The local reconstruction resolution, as assessed by the ResMap method,[35] is from 0.6 nm to 1.1 nm (see Supporting Information for a comparison of ResMap and Fourier Shell Correlation, Figs S1-4).

Visualisation of 3D chemical inhomogeneity in the PtNi NP populations. Based on the reconstructed 3D EDS intensity distribution, we performed EDS quantification to determine the elemental Pt and Ni composition for each voxel using a standardless Cliff-Lorimer approach (Figure 4) (see Supporting Information for a brief discussion of errors in the EDS quantification). Enrichment of Pt above the mean composition of 59 at% was observed in the NP core and at vertices along <111> directions (red in Figure 4 a and b, also indicated by the arrows in c). Enrichment of Ni >41 at% occurs at the concave {110} type facets and at vertices oriented along <100> directions (green in Figure 4a and b, also indicated by arrows in d). As the particles are all single crystals we can use information from high resolution TEM (Fig. S15) or STEM images to assign the atomic structure to the reconstruction. In figure 4a and 4b, spheres represent approximately 4 atoms to illustrate the atomic arrangement in this nanocrystal for better clarity (see Methods). A realistic atomic model was built by filling the EDS atomic percentage reconstructions with atoms in the correct crystallographic arrangement (Figure 4e and f, Figs. S18 and S19 and Videos S9-11). Individual atom species (Pt or Ni) were assigned randomly using the quantitative voxel composition as a probability factor (for further information see Methods). In summary, these concave rhombic dodecahedron

NPs display a complex inhomogeneous alloying with a Pt-rich core, a Ni-rich hollow octahedral intermediate shell and a Pt-rich rhombic dodecahedral skeleton framework with less Pt at <100> vertices (See Videos S6-9).

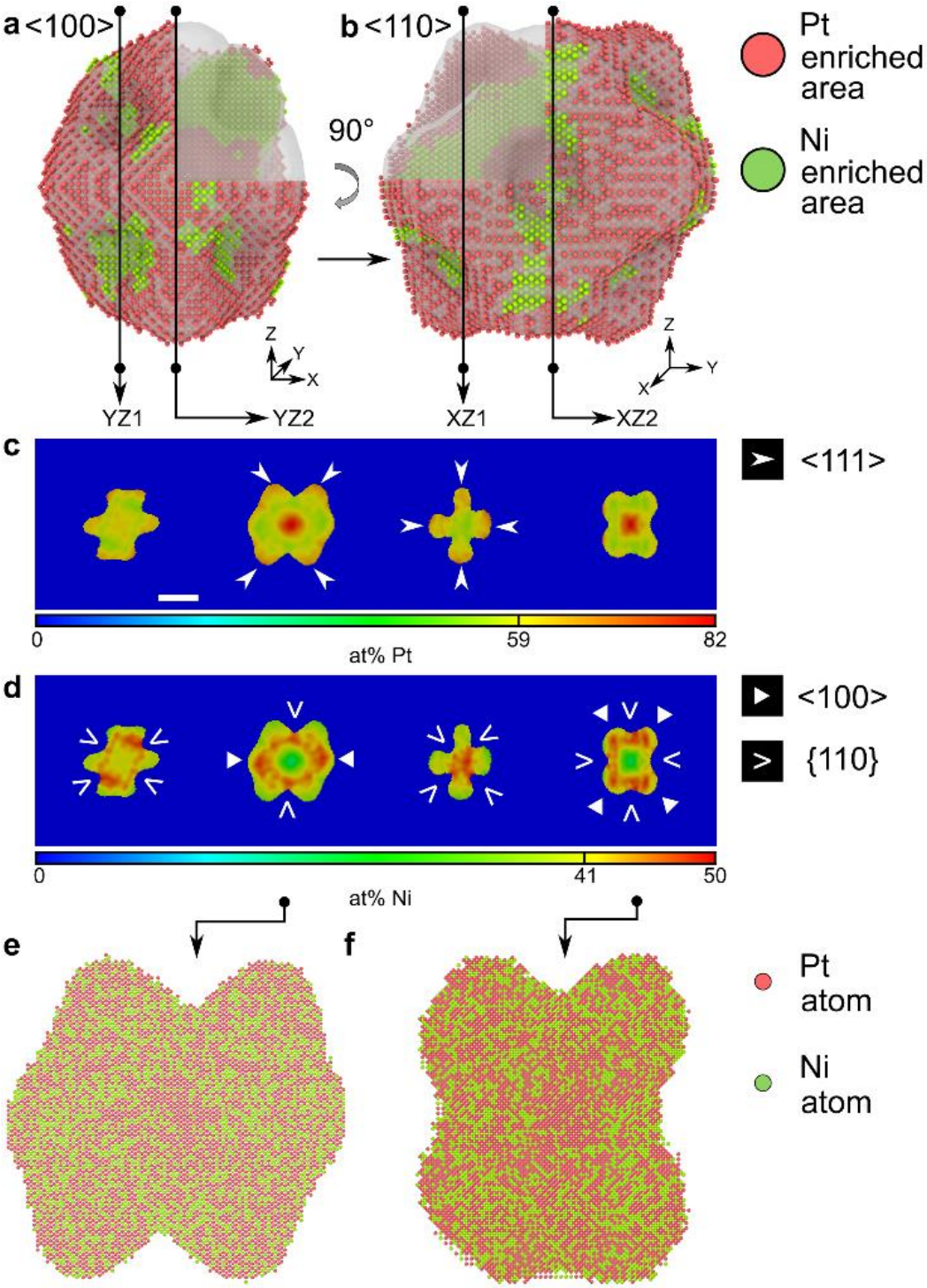

Figure 4 Visualisation of 3D chemical segregation in the PtNi NP population. a and **b,** Quantitative SPR elemental reconstruction thresholded at 59 at% Pt (higher Pt content is shown red while lower

Pt, above 41 at% Ni, is shown in green) viewed along <100> and <110> directions, respectively. One eighth of the volume is cut from each reconstruction (shaded) to reveal the internal elemental distribution. Red and green balls illustrate the crystallographic arrangement of atoms in this nanocrystal. **c-d,** Slices through the elemental distributions for Pt and Ni, respectively coloured to reflect the at% for each element. Elemental enrichment on the <111> vertices, {110} facets and <100> vertices are indicated by different arrows. Scale bar is 10 nm. **e** and **f,** Two-atom thick slices extracted from the atomic model (Video S9). Red and green atoms are Pt and Ni, respectively. Further details of the quantitative thresholding and atom fitting are described in Methods.

Previous characterisation of this important catalytic nanoparticle system was limited to 2D (S)TEM analysis[27–32], which can be difficult to interpret due to a complex structure being projected along the third dimension. The methodology we have described provides unambiguous information on elemental segregation, with details on facet-dependent elemental segregation that has previously been inaccessible. The 3D elemental reconstruction of these Pt-Ni concave rhombic dodecahedral nanoparticles is consistent with previous 2D elemental mapping results[27–32] in that it reveals a Pt rich core and Pt rich edges (Figure 4). The Pt-rich core is attributed to the Pt seeds used to nucleate the particles[30,32]. We also observe a depletion of Pt (Ni enrichment) on all {110} faces, which has also been observed in octahedral PtNi nanoparticles[27,28,30]. However, our detailed characterisation has also revealed differences in composition of the different vertices (<111> vertices are enriched in Pt while <100> vertices are depleted in Pt compared to the mean NP composition). Importantly, we observe the same elemental enrichment behaviour in our spectroscopic SPR reconstructions for particles with a lower mean Pt content (45-55 at% Pt, Fig. S16 and S17), suggesting this is general to the whole nanoparticle population.

Discussion. The complex compositional segregation we observed cannot be simply explained by equilibrium thermodynamics and are likely to be kinetically influenced by the synthesis route, as demonstrated by the Pt rich seed observed in the nanoparticle core. The depletion of Ni on the surfaces is also a result of the synthesis route and may be attributed to the different strength of the

interaction of Pt and Ni with the oleylamine surface ligands[29]. Ni atoms are more easily oxidised than Pt, forming soluble metal complexes, which leads to faster leaching of Ni from the surfaces during ageing[29].The different enrichment behaviour of the vertices can be explained by the drive to minimize both surface energy and local lattice strain. The surface free energies[36] for Ni are 2.011 J m^{-2} for {111}, 2.368 J m^{-2} for {110} and 2.426 J m^{-2} for {100} surface facets, while those for Pt are 2.299 J m^{-2} for {111}, 2.819 J m^{-2} for {110} and 2.734 J m^{-2} for {100}. Both elements therefore strongly prefer to sit on {111} facets but Pt has the larger lattice parameter[37] (0.39 nm vs 0.35 nm for Ni) so the enrichment of Pt we observe for the {111} vertices is likely favoured to minimise strain.

The distribution of Pt at different vertices will have an effect on the catalytic performance of nanoparticles. Studies of flat surfaces at different crystallographic orientations have revealed that certain orientations are strongly favoured for oxygen reduction activity,[33] and we would expect certain vertices to similarly display a higher activity towards catalysing reactions. However, the atomic arrangement and local lattice strain environments found at vertices are more complex than flat surfaces. Understanding the nature of individual surface sites at each vertex as a function of chemistry would be an interesting area for further work. Such investigations could be coupled with density functional theory or molecular dynamics calculations to study the effect of variations in vertex chemistry on catalytic properties.

We aim to develop our spectroscopic single particle reconstruction further in a number of directions. The first suggested development is with regards to the analysis of inhomogenous nanoparticle populations. In this study we have investigated nanoparticles with a very narrow distribution in size, morphology and chemistry, which is a pre-requisite of the reconstruction. The vast majority of inorganic nanoparticles have much wider distributions of these properties and a single particle reconstruction might not at first seem applicable. However, we have demonstrated a very simple method of pre-filtering particles by size and composition that we have shown can be used to separate the particle population in to different “classes” that can each be reconstructed separately. We suggest that application of more complex pre-filtering, for example by using machine

learning approaches, could allow sorting of nanoparticles in to tens or hundreds of “classes”, each providing a unique reconstruction, which could then be ranked by statistical significance in terms of the overall population. This is one clear advantage of the single particle reconstruction technique when compared to tilt-series electron tomography; the reconstruction obtained is representative of a larger subset of the nanoparticle population. The corresponding drawback is that features possessed by only a few particles may be lost in the reconstruction. One clear future direction for this research will be to optimise particle selection to balance the number of classes and the number of identical particles in each class to perform a reconstruction with a high signal to noise ratio that is representative of a significant part of the nanoparticle population.

Additionally, utilising the structural symmetry of the nanoparticle could increase the SNR further but may generate artefacts, since the imposed symmetry must be fulfilled during orientation matching and reconstruction. For example, the highest order symmetry applicable to the nanoparticles investigated here is octahedral, which should result in a 12 fold increase in SNR. We plan to utilise higher order symmetries in future reconstructions but demonstrate here that this is not necessary to achieve an appreciable SNR and therefore nanoparticles possessing no symmetry could be faithfully reconstructed.

The approach we developed can also be extended to other spectroscopic signals available in the microscope. For example, EELS could be used to map elemental distributions, bulk plasmons or oxidation states of geometric nanoparticles using the technique. In particular, the higher signal collection efficiency of EELS may give it an advantage in 3D mapping of lower atomic number elements.

In conclusion, we have developed a novel methodology for spectroscopic STEM-EDS single particle reconstruction for characterisation of 3D elemental distribution at the nanometer scale. Here we have applied the approach to relatively large NPs (~20 nm in diameter) but it would be an interesting next step to push the reconstruction resolution of the approach to resolve atomic chemistry for smaller particles. It could then be compared to another STEM based 3D reconstruction technique of

atom counting,[10–13] which is a powerful approach for atomic reconstruction of small particles but is currently limited to one or two component systems. Compared to traditional tilt-series STEM-EDS tomography, our SPR approach has demonstrated a near 500 times reduction in the required electron fluence per particle for the same cumulative dose in the final reconstruction and has the potential for further reduction simply by including more particle images, or through combination with sparse sampling and new reconstruction algorithms.[38–41] Our proof-of-principle study demonstrates the capabilities of the spectroscopic SPR technique to reveal complex elemental distributions within PtNi concave rhombic dodecahedral shaped nanoparticles, which have been identified as one of the most active ORR catalysts ever designed.[1,29] The reconstruction also provides new evidence for the importance of considering the effects of crystallographic vertices and surface facets on local elemental distribution.

The importance of advanced structural and elemental characterisation is being increasingly recognised as a necessary step to designing new nanomaterials with improved properties. The detailed structural information accessible using this approach is therefore likely to reduce the computational requirements for theoretical modelling of the energetics of large (>2 nm) alloy nanoparticles,[42] and hence assist the realisation of optimal nanoalloy NP design for catalysis, medical imaging and sensing.

ASSOCIATED CONTENT

Supporting Information.

The following files are available free of charge.

Detailed methods, discussion of spectroscopic single particle reconstruction resolution, figures S1 to S19, tables S1 and S2, description of videos 1 to 11, references. (PDF) Video S1: Tilt-series tomographic acquisition of HAADF images (AVI). Video S2: Tilt-series tomography reconstruction of HAADF intensity (AVI). Video S3: SPR reconstruction of HAADF

intensity (AVI). Video S4: SPR reconstruction of EDS Pt intensity (AVI). Video S5: SPR reconstruction of EDS Ni intensity (AVI). Video S6: 3D atomic percentage distribution of Pt (AVI). Video S7: 3D atomic percentage distribution of Ni (AVI). Video S8: Composite 3D atomic percentage distribution of Pt and Ni with one eighth cut out and thresholded at 59 at% Pt and 41 at% Ni (AVI). Video S9: 3D atomic models of PtNi based on Pt and Ni 3D atomic percentage distribution. The model contains 123086 Pt atoms (red) and 81040 Ni atoms (green) (AVI). Video S10: Two atom thick slices through the atomic models presented in Video S9. Viewed from the <110> direction (AVI). Video S11: Two atom thick slices through the atomic models presented in Video S9. Viewed from the <100> direction (AVI).

AUTHOR INFORMATION

Corresponding Authors

*E-mail: Sarah.haigh@manchester.ac.uk

*E-mail: Thomas.slater@diamond.ac.uk

Author Contributions

S.J.H. and T.J.A.S. conceived the idea and supervised the project. T.J.A.S. and Y.-C.W. acquired data. Y.-C.W. processed, interpreted and visualised data. G.L. and C.L. synthesised nanoparticles. Y.-C.W., T.J.A.S. and S.J.H. wrote the manuscript. A.M.R. helped with the improvement of the reconstruction quality. C.P.R. built a preliminary atomic model. N.P.Y. and A.I.K. performed preliminary TEM characterisation. All authors commented on the manuscript.

Notes

The authors declare no competing financial interest.

ACKNOWLEDGMENT

S.J.H. T.J.A.S and Y.-C.W acknowledge funding from the European Research Council (ERC) under the European Union's Horizon 2020 research and innovation programme (through the Hetero2D Synergy grant and grant agreement ERC-2016-STG-EvoluTEM-715502), from the Engineering and Physical Sciences research council (EPSRC) U.K grants EP/G035954/1, EP/K016946/1, EP/J021172/1 and EP/P009050/1, the NowNANO CDT, and the Defense Threat Reduction Agency Grant HDTRA1-12-1-0013. Y.-C.W acknowledges funding from the China Scholarship Council (CSC).

REFERENCES

(1) Strasser, P.; Gliech, M.; Kuehl, S.; Moeller, T. *Chem. Soc. Rev.* **2018**, *47*, 715–735.

(2) Gilroy, K. D.; Ruditskiy, A.; Peng, H. C.; Qin, D.; Xia, Y. *Chem. Rev.* **2016**, *116*, 10414–10472.

(3) Fernandez-Leiro, R.; Scheres, S. H. W. *Nature* **2016**, *537*, 339–346.

(4) Midgley, P. A.; Dunin-Borkowski, R. E. *Nat. Mater.* **2009**, *8*, 271–280.

(5) Scott, M. C.; Chen, C.-C.; Mecklenburg, M.; Zhu, C.; Xu, R.; Ercius, P.; Dahmen, U.; Regan, B. C.; Miao, J. *Nature* **2012**, *483*, 444–447.

(6) Goris, B.; Bals, S.; Van den Broek, W.; Carbó-Argibay, E.; Gómez-Graña, S.; Liz-Marzán, L. M.; Van Tendeloo, G. *Nat. Mater.* **2012**, *11*, 930–935.

(7) Nicoletti, O.; de la Peña, F.; Leary, R. K.; Holland, D. J.; Ducati, C.; Midgley, P. a. *Nature* **2013**, *502*, 80–84.

(8) Yang, Y.; Chen, C.-C.; Scott, M. C.; Ophus, C.; Xu, R.; Pryor, A.; Wu, L.; Sun, F.; Theis, W.; Zhou, J.; et al. *Nature* **2017**, *542*, 75.

(9) Van Dyck, D.; Jinschek, J. R.; Chen, F.-R. *Nature* **2012**, *486*, 243–246.

(10) Van Aert, S.; Batenburg, K. J.; Rossell, M. D.; Erni, R.; Van Tendeloo, G. *Nature* **2011**, *470*, 374–377.

(11) Jia, C. L.; Mi, S. B.; Barthel, J.; Wang, D. W.; Dunin-Borkowski, R. E.; Urban, K. W.; Thust, A. *Nat. Mater.* **2014**, *13*, 1044–1049.

(12) Jones, L.; Macarthur, K. E.; Fauske, V. T.; Van Helvoort, A. T. J.; Nellist, P. D. *Nano Lett.* **2014**, *14*, 6336–6341.

(13) van den Bos, K. H. W.; De Backer, A.; Martinez, G. T.; Winckelmans, N.; Bals, S.; Nellist, P. D.; Van Aert, S. *Phys. Rev. Lett.* **2016**, *116*, 246101.

(14) Slater, T. J. A.; Macedo, A.; Schroeder, S. L. M.; Burke, M. G.; O'Brien, P.; Camargo, P. H. C.; Haigh, S. J. *Nano Lett.* **2014**, *14*, 1921–1926.

(15) Slater, T. J. A.; Janssen, A.; Camargo, P. H. C.; Burke, M. G.; Zaluzec, N. J.; Haigh, S. J. *Ultramicroscopy* **2016**, *162*, 61–73.

(16) Rueda-Fonseca, P.; Robin, E.; Bellet-Amalric, E.; Lopez-Haro, M.; Den Hertog, M.; Genuist, Y.; André, R.; Artioli, A.; Tatarenko, S.; Ferrand, D.; et al. *Nano Lett.* **2016**, *16*, 1637–1642.

(17) Jarausch, K.; Thomas, P.; Leonard, D. N.; Twesten, R.; Booth, C. R. *Ultramicroscopy* **2009**, *109*, 326–337.

(18) Haberfehlner, G.; Orthacker, A.; Albu, M.; Li, J.; Kothleitner, G. *Nanoscale* **2014**, *6*, 14563-14569. (19) Frank, J. *Nat. Protoc.* **2017**, *12*, 209–212.

(20) Nobelprize.org. The Nobel Prize in Chemistry 2017 http://www.nobelprize.org/nobel_prizes/chemistry/laureates/2017/ (accessed Apr 10, 2018).

(21) Henderson, R. *Arch. Biochem. Biophys.* **2015**, *581*, 1–6.

(22) Cheng, Y.; Grigorieff, N.; Penczek, P. A.; Walz, T. *Cell* **2015**, *161*, 438–449.

(23) Rosenthal, P. B.; Henderson, R. *J. Mol. Biol.* **2003**, *333*, 721–745.

(24) Tang, G.; Peng, L.; Baldwin, P. R.; Mann, D. S.; Jiang, W.; Rees, I.; Ludtke, S. J. *J. Struct. Biol.* **2007**, *157*, 38–46.

(25) Baldwin, P. R.; Penczek, P. A. *J. Struct. Biol.* **2007**, *157*, 250–261.

(26) Pan, Y.-H.; Sader, K.; Powell, J. J.; Bleloch, A.; Gass, M.; Trinick, J.; Warley, A.; Li, A.; Brydson, R.; Brown, A. *J. Struct. Biol.* **2009**, *166*, 22–31.

(27) Cui, C.; Gan, L.; Heggen, M.; Rudi, S.; Strasser, P. *Nat. Mater.* **2013**, *12*, 765–771.

(28) Gan, L.; Cui, C.; Heggen, M.; Dionigi, F.; Rudi, S.; Strasser, P. *Science* **2014**, *346*, 1502–1506.

(29) Chen, C.; Kang, Y.; Huo, Z.; Zhu, Z.; Huang, W.; Xin, H. L.; Snyder, J. D.; Li, D.; Herron, J. A.; Mavrikakis, M.; et al. *Science* **2014**, *343*, 1339–1343.

(30) Oh, A.; Baik, H.; Choi, D. S.; Cheon, J. Y.; Kim, B.; Kim, H.; Kwon, S. J.; Joo, S. H.; Jung, Y.; Lee, K. *ACS Nano* **2015**, *9*, 2856–2867.

(31) Niu, Z.; Becknell, N.; Yu, Y.; Kim, D.; Chen, C.; Kornienko, N.; Somorjai, G. A.; Yang, P. *Nat. Mater.* **2016**, *15*, 1188–1194.

(32) Chang, Q.; Xu, Y.; Duan, Z.; Xiao, F.; Fu, F.; Hong, Y.; Kim, J.; Choi, S.-I. Il; Su, D.; Shao, M. *Nano Lett.* **2017**, *17*, 3926–3931.

(33) Stamenkovic, V. R.; Fowler, B.; Mun, B. S.; Wang, G.; Ross, P. N.; Lucas, C. A.; Marković, N. M. *Science* **2007**, *315*, 493–497.

(34) Stamenkovic, V. R.; Mun, B. S.; Arenz, M.; Mayrhofer, K. J. J.; Lucas, C. a; Wang, G. F.; Ross, P. N.; Markovic, N. M. *Nat. Mater.* **2007**, *6*, 241–247.

(35) Kucukelbir, A.; Sigworth, F. J.; Tagare, H. D. *Nat. Methods* **2014**, *11*, 63–65.

(36) Vitos, L.; Ruban, A. V.; Skriver, H. L.; Kollár, J. *Surf. Sci.* **1998**, *411*, 186–202.

(37) Davey, W. P. *Phys. Rev.* **1925**, *25*, 753–761.

(38) Saghi, Z.; Holland, D. J.; Leary, R.; Falqui, A.; Bertoni, G.; Sederman, A. J.; Gladden, L. F.; Midgley, P. a. *Nano Lett.* **2011**, *11*, 4666–4673.

(39) Goris, B.; Van den Broek, W.; Batenburg, K. J.; Heidari Mezerji, H.; Bals, S. *Ultramicroscopy* **2012**, *113*, 120–130.

(40) Leary, R.; Saghi, Z.; Midgley, P. A.; Holland, D. J. *Ultramicroscopy* **2013**, *131*, 70–91.

(41) Saghi, Z.; Benning, M.; Leary, R.; Macias-Montero, M.; Borras, A.; Midgley, P. a. *Adv. Struct. Chem. Imaging* **2015**, *1*, 1–10.

(42) Yan, Z.; Taylor, M. G.; Mascareno, A.; Mpourmpakis, G.; Yan, Z.; Taylor, M. G.; Mascareno, A.; Mpourmpakis, G. *Nano Lett.* **2018**.

Supporting Information: Imaging 3D elemental inhomogeneity in Pt-Ni nanoparticles using spectroscopic single particle reconstruction

Methods

Synthesis of PtNi nanoparticles. In a standard co-reduction procedure: nickel (II) acetate tetrahydrate (0.033g, 0.13 mmol) and chloroplatinic acid solution (8 wt. % in water) (1 ml, 0.20 mmol) precursor salts were dissolved in 25 ml 1-octadecene (1-OD) (a high boiling point solvent) in the presence of ternary hydrophobic surfactants oleylamine (OAm, 15 ml), octadecylamine (ODA, 4.4g) and oleic acid (OLEA, 15 ml) followed by sonication for 20 minutes. The resultant solution was heated and held at 150 °C under vigorous magnetic stirring, which yielded a homogeneous pale yellow solution. After the addition of the reductant tetrabutylammonium borohydride (TBAB) (0.05 g, 0.19 mmol), the reaction temperature was raised to 240 °C, with a heating rate of 10 °C/min and maintained at this temperature for 30–40 minutes in air. Upon complete reduction, the observed dark brown colloidal suspension was removed from the heat source and allowed to cool down to room temperature. The as-synthesized PtNi colloidal structures were then precipitated by the addition of excess ethanol as a flocculent. The flocculation-and-purification process was performed three times to eliminate unwanted surfactants that were not attached or adsorbed on the surface of the particles and undesired solvent (1-OD). Thereafter the resulting black product was re-suspended in chloroform, yielding a brownish colour with some particle agglomerates. This suggests that all the surfactants required for a stable homogeneous colloidal dispersion in organic solvents such as chloroform, toluene or hexane were eliminated from the surface of the particles, leading to destabilization of the particles. Provided the particles did not form agglomerates during synthesis but only after repeated washing, we reverse this particle homoagglomeration/homocoagulation via a peptization process using OAm as the dispersant to yield a complete homogeneous colloidal

suspension (mix purified nanoparticles with OAm and chloroform, vigorously sonicate the resultant solution for 15-20 minutes, leave for 1-2 days in air to allow OAm molecules to attach/adsorb on the surface of the particles). This was followed by washing the particles 2 times using ethanol and re-suspension in chloroform. We have discovered that the subsequent addition of OAm improves the processability of unstable particles by transforming them into a homogeneous colloidal suspension. However, this phenomenon is only predominant in nanoparticles solution-grown using hydrophobic surfactants but it also appears to selectively leach out/dissolve Ni-rich regions from the surfaces during ageing, resulting in concave Pt-rich surfaces.[1]

2D STEM HAADF and EDS data acquisition. Nanoparticle dispersions were drop-cast onto carbon-coated Cu grids and dried under ambient conditions. All HAADF and EDS data were collected using a Thermo Fisher (formerly FEI) Titan G2 80-200 S/TEM operated at 200 kV, which was equipped with an X-FEG high brightness source, STEM probe aberration correction and a ChemiSTEM™ Super-X EDS detector consisting of four silicon drift detectors (SDDs) with a total collection solid angle of approximately 0.7 sr. A convergence angle of 21 mrad and an acceptance inner angle of 55 mrad were used for HAADF image acquisition. Tilt-series tomography HAADF images were collected using a Fischione 2020 single tilt tomography holder and FEI Inspect3D software. The total tilt range was ±70° with a pixel size of 0.07 nm and a pixel dwell time of 10 µs. Incremental steps of 2° at ±50° and 1° for the rest of the tilt range were used. For the acquisitions used for spectroscopic single particle reconstruction, the beam current was approximately 520 pA and the per pixel dwell time for EDS was 190 µs with a total acquisition time of 20 minutes (24 frames) for 512×512 pixels areas with a pixel size of 0.28 nm. The same imaging conditions were applied for tilt-pair acquisitions at a tilt angle of 0°. For tilt-pair imaging of the same area at a tilt angle of 30°, the 2 EDS detectors away from the tilting direction were switched off to minimise detector shadowing[2] and the acquisition time was extended to 40 minutes.

Image processing and particle segmentation. After acquisition, the uneven background intensity of images was corrected by a "rolling ball" algorithm[3] in Fiji (ImageJ)[4] with a conservative optimisation parameter (rolling ball radius 200 pixels, 112 nm, and with the sliding paraboloid option enabled) as a preliminary background subtraction. Image intensities were rescaled with 50% saturation to enhance foreground particle regions. Thereafter, foreground particle regions were masked by a "Huang" thresholding algorithm.[5] Watershed segmentation[6] was used to segment touching particles and the averaged background intensity value was subtracted from the particle region of interest. Manual evaluation was performed after segmentation to make sure only well segmented particles remained. Subsequently STEM HAADF images had all background pixel values set to zero. 2D EDS intensity maps were extracted at energies of 7.334–7.622 keV (Ni Kα) and 9.281–9.603 keV (Pt Lα) using the HyperSpy python package.[7] Associated STEM HAADF images were used as masks to remove background signals from the EDS maps. All 2D STEM HAADF images and EDS maps shown in the main text were smoothed with a 2 sigma Gaussian filter (i.e. the standard deviation of the Gaussian is 2 pixels, 0.56 nm; Fig S8).

STEM HAADF tilt-series electron tomography reconstruction. The 3D reconstruction was performed using a simultaneous iterative reconstruction technique (SIRT) algorithm with the python application programming interface (API) in the Astra toolbox,[8] with 200 iterations. The reconstructed 3D tomogram was thresholded based on its histogram, rebinned to a voxel size of 0.28 nm and the particle size was rescaled to the mean size of the particles used for single particle reconstruction. The 3D tomogram was then aligned to the symmetry axis and its centre of mass. The box size was set to 151×151×151 voxels. A 3D Gaussian filter with 2 sigma kernel size was applied to the 3D tomogram and 400 re-projections were generated from this 3D tomogram with a box size of 151×151 pixels, 2-fold rotational (C2) symmetry and including mirror portions using the EMAN2 projection generator[9,10] coded in python.

Spectroscopic single particle reconstruction. STEM HAADF images and EDS elemental maps of each segmented particle were relocated into 151×151 pixels boxes and centred according to the geometric centre of the HAADF image. A 2D Gaussian filter with a 2 sigma kernel size was applied to all HAADF images and EDS elemental maps to ameliorate the sharp boundary after segmentation and to improve matching quality. Each HAADF particle image was matched with all 400 re-projection references using a cross correlation function implemented in EMAN2, including rotating each reference from 0°–360° with 2° increments. After matching, using the reference with the highest cross correlation coefficient value, an orientation was assigned to the matched HAADF images and the corresponding EDS elemental maps. Each matched particle-reference pair was then manually evaluated to discard any incorrect matches. Thereafter, the total intensity of each non-blurred HAADF image and EDS elemental maps was calculated separately and split into two groups, 45-55 at% Pt and 55-65 at% Pt, based on particle composition. In each group, the total intensity value of the HAADF image and EDS elemental maps were first calculated for each particle and then normalised to the mean total intensity of images in the group. The normalised images were used for the reconstruction. A direct Fourier reconstruction algorithm, C2 symmetry and a 151×151×151 voxel box size were used for the final SPR reconstruction using EMAN2[9] within python. After reconstruction, HAADF reconstruction was thresholded by a value of 1.14 determined by 'Huang' threshold algorithm[5] using 3D stack histogram in Fiji.[4] A 3D Gaussian filter with 2 sigma kernel size was then applied to both HAADF and EDS intensity reconstructions. Re-projections were generated by rotating the reconstructed 3D tomogram to the required orientation and then calculating the summed voxel intensities along the re-projection direction.

3D EDS quantification and visualisation. For each 2D EDS image, the mean weight percentage of Pt ($wt\%\ Pt_{mean}^{2D}$) and Ni ($wt\%\ Ni_{mean}^{2D}$) were determined using equation (1), using all 475 matched 2D EDS images and standard-less Cliff Lorimer k-factors of 5.162 (k_{Pt}^{2D}) and 1.585 (k_{Ni}^{2D}) (with respect to Si Kα) for Pt Lα and Ni Lα respectively, calculated in the Bruker Esprit software database. While some reports have found that standard-less k-factors can have associated errors of up to 20%,[11] our

previous experiments using the same microscope have found that for binary metal alloys with similar x-ray energies, the calculated k-factors possessed an error of less than 2%.

$\sum I^{2D}$ is the summation of all 2D pixel intensities from one of 475 EDS images and $\sum_1^{475}$ is the summation of image intensities over all 475 images. The new 3D k-factor ratio ($\frac{k_{Pt}^{3D}}{k_{Ni}^{3D}}$) was determined from equation (2), where $\sum I^{3D}$ is the summation of all 3D voxel intensities from the reconstructed EDS intensity tomograms. Finally, for a voxel i, its quantified 3D composition ($wt\%\ Pt_i^{3D}$ and $wt\%\ Ni_i^{3D}$) was determined from the calculated 3D k-factors and the reconstructed voxel intensities of Pt ($I_{i,Pt}^{3D}$) and Ni ($I_{i,Ni}^{3D}$) using equation (3). The weight percentage values were then converted to atomic percentage values. All 3D renders and movies were visualised using the open source software TomViz (https://tomviz.org).12

$$\frac{wt\%\ Pt_{mean}^{2D}}{wt\%\ Ni_{mean}^{2D}} = \frac{k_{Pt}^{2D}}{k_{Ni}^{2D}} \frac{\sum_1^{475} \sum I_{Pt}^{2D}}{\sum_1^{475} \sum I_{Ni}^{2D}} \qquad \text{Equation 1}$$

$$\frac{k_{Pt}^{3D}}{k_{Ni}^{3D}} = \frac{wt\%\ Pt_{mean}^{2D}}{wt\%\ Ni_{mean}^{2D}} \frac{\sum I_{Ni}^{3D}}{\sum I_{Pt}^{3D}} \qquad \text{Equation 2}$$

$$\frac{wt\%\ Pt_i^{3D}}{wt\%\ Ni_i^{3D}} = \frac{k_{Pt}^{3D}}{k_{Ni}^{3D}} \frac{I_{i,Pt}^{3D}}{I_{i,Ni}^{3D}} \qquad \text{Equation 3}$$

Atomic model. A unit cell length of 0.37 nm was used for generating atomic models. The unit cell value chosen was the mean unit cell length of Pt (0.39 nm) and Ni (0.35 nm).[13] The crystallographic orientation of the reconstructed particle was determined by examining high resolution TEM images (Fig. S15). Atom coordinates were generated in a face centred cubic (FCC) crystal and filled all space in the reconstruction box. The HAADF SPR reconstructed tomogram was used as a mask to delete atoms outside the mask area. For each voxel in the 3D atomic percentage distribution, atoms within that voxel were randomly assigned to be either Pt or Ni using the voxel at% values as a probability. For better clarity, in Figure 4 a and b, atomic percentage 3D reconstructions of Pt and Ni were thresholded and binned from a 151×151×151 voxel box to a 76×76×76 voxel box, which resulted in

the width of each voxel increasing from 2.8 nm to 5.6 nm. Then each voxel was treated as a FCC unit cell to assign atoms. 3D atomic models were visualised using Ovito (http://ovito.org).[14]

Spectroscopic single particle reconstruction (SPR) resolution

It is useful to assess the resolution of the reconstructions we have obtained in order to validate the fidelity of the elemental data. Optimal methodologies for assessing the resolution of 3D reconstruction data are still the subject of considerable debate[15–23] but in structural biology the spatial resolution of a single particle reconstruction is typically reported based on a Fourier Shell Correlation (FSC) analysis.[18–21] FSC involves splitting the full data set into two halves and performing two independent 3D reconstructions. The Fourier transforms of the resulting two 3D reconstructions are then compared shell by shell, starting from the lowest spatial frequency inner core and proceeding to the highest spatial frequency present in the data set. The resolution of the data set is reported as the spatial frequency for which the similarity of the Fourier shells of the two reconstructions falls below a threshold value.

We have performed FSC analysis on both our STEM-HAADF and STEM-EDS spectroscopic reconstructions. Initially, FSC was performed on reconstructions without the removal of reconstruction background. The FSC values under these conditions were found to be 23.6, 30.6 and 32.9 Å for the STEM-HAADF, STEM-EDS (Pt) and STEM-EDS (Ni) reconstructions respectively, using a 0.143 correlation coefficient value as a threshold[17] (Figs. S1 b, S2 a and S2 c). If employing thresholding[5] to remove reconstruction background, as employed for the final reconstructions, the FSC resolutions are found to be 6.6, 19.3, 21.0 Å for the HAADF, Pt and Ni reconstructions respectively, again using a 0.143 correlation coefficient value as a threshold[3] (Figs. S1 c, S2 b and S2 d). When performing FSC for the two reconstructions from unmasked data, high frequency information from 'true structure' is more likely to be supressed by high frequency reconstruction

artefacts (Fig. S1 b and e and Fig. S2 a and c). Since the artefacts from the two reconstructions are unlikely to be same, this procedure leads to a worse FSC resolution. However, the two reconstructions that were masked prior to the FSC, to eliminate reconstruction artefacts (Fig. S2 c and f and Fig. S3 b and d), possess a much better FSC resolution as high frequency artefacts are partially removed.

Our STEM-HAADF images have a far greater signal-to-noise-ratio (SNR) compared to typical virus or protein TEM image data sets used for SPR in structural biology. This allows us to use far fewer particles to achieve a successful reconstruction (hundreds of images rather than the hundreds of thousands of images typically used for conventional SPR[24]). Unfortunately the smaller number of particles hinders the accuracy of the FSC procedure, as some orientations will likely be missing when the data is split into two, producing artefacts in the resulting reconstructions. For this reason, we have employed a further method named 'ResMap'[23] to assess reconstruction resolution and further validate the methods employed.

The ResMap approach is based on local sinusoidal features.[23] This method defines the local resolution at a point as the smallest wavelength at which the 3D local sinusoid is statistically detectable above the noise/surrounding background signals at that point.[23] There are two advantages to applying this method to our spectroscopic SPR data sets compared to FSC. Firstly, this method does not require splitting full data sets into two halves. Secondly, the resolution is assessed against the surrounding background signals. This means it tests the detectability of real structure signals against reconstruction artefacts. Therefore, the measured resolution could be seen to be more reliable than that assessed using FSC. Using unmasked reconstructions (STEM-HAADF and spectroscopic STEM-EDS) as input data sets, more than 60% of the reconstructed voxels yielded resolution values better than 7 Å and all voxels yielded values better than 12 Å (Figure S3). The resolution range generated from ResMap methods is in agreement with the FSC resolution found for our masked STEM-HAADF data sets. The key elemental segregation features identified in our

reconstructed data have spatial dimensions considerably larger than this resolution; greater than 30 Å in most directions (main text Figure 4, Figure S4 and S18) so we can be confident of the fidelity of the compositional segregation behaviour we observe.

It is useful to also compare our data to a traditional tilt-series ET reconstruction. Qualitatively we observe that the SPR reconstruction possesses fewer artefacts due to its greater angular coverage and lack of 'missing wedge' (Figure S6). The SPR reconstruction procedure is a non-iterative one-time Fourier space back-projection[9] while the tilt-series reconstruction is an iterative SIRT reconstruction and yet the SPR reconstruction qualitatively appears to have a higher fidelity. Nevertheless when comparing ET and SPR reconstructions it is important to note that the ET approach is for a single NP while SPR is an ensemble average for the NP particle population. By providing 3D reconstructions that are truly representative of a large number of nanoparticles, spectroscopic SPR overcomes one of the major limitations of conventional 3D transmission electron microscope characterisation of inorganic nanoparticle systems. However, we recognise that both single and ensemble NP data may be important input for optimisation of NP properties.

Errors in EDS quantification at each voxel

It is informative to attempt to estimate the errors associated with our final quantification values for each voxel. Each image contains about 2210 total counts for the Ni K peaks and 3500 total counts for the Pt L peaks, which gives approximately 0.5 Ni counts per pixel and 0.7 Pt counts per pixel. A very naïve estimation of error is to consider that this would result in approximately 240 Ni counts and 330 Pt counts contributing to the intensity in each voxel, considering that the reconstruction is formed from 475 images. Taking the square root of these values as an initial estimate of error would give errors of 7% and 6% on the intensity at each voxel, for Pt and Ni respectively. These values are roughly equivalent to those obtained when considering backprojection as a simple sum of pixel intensities and propagating errors in quadrature.

This rough estimation does not take in to consideration how errors actually propagate through backprojection. However, a detailed consideration of EDS quantification errors in 3D would require extensive further study including consideration of the distortion to the quantification of the 3D reconstructions due to Fourier space interpolation and missing image orientations. For our work, we consider the limited number of x-ray counts for each element to be the major source of inaccuracy in the data and the quantification of composition could therefore be improved by increasing the number of counts per pixel in each image or through the addition of more images. For our SPR technique the latter approach is clearly preferable because unlike in conventional tilt series tomography increasing the number of images can be achieved without increasing the electron fluence experienced by individual particles.

Additionally, we expect errors through the use of standardless calculated Cliff-Lorimer k-factors, although measurement of Cliff-Lorimer k-factors from a standard PtFe sample on this microscope would indicate that errors are below 2% for k-factors at very similar energies.

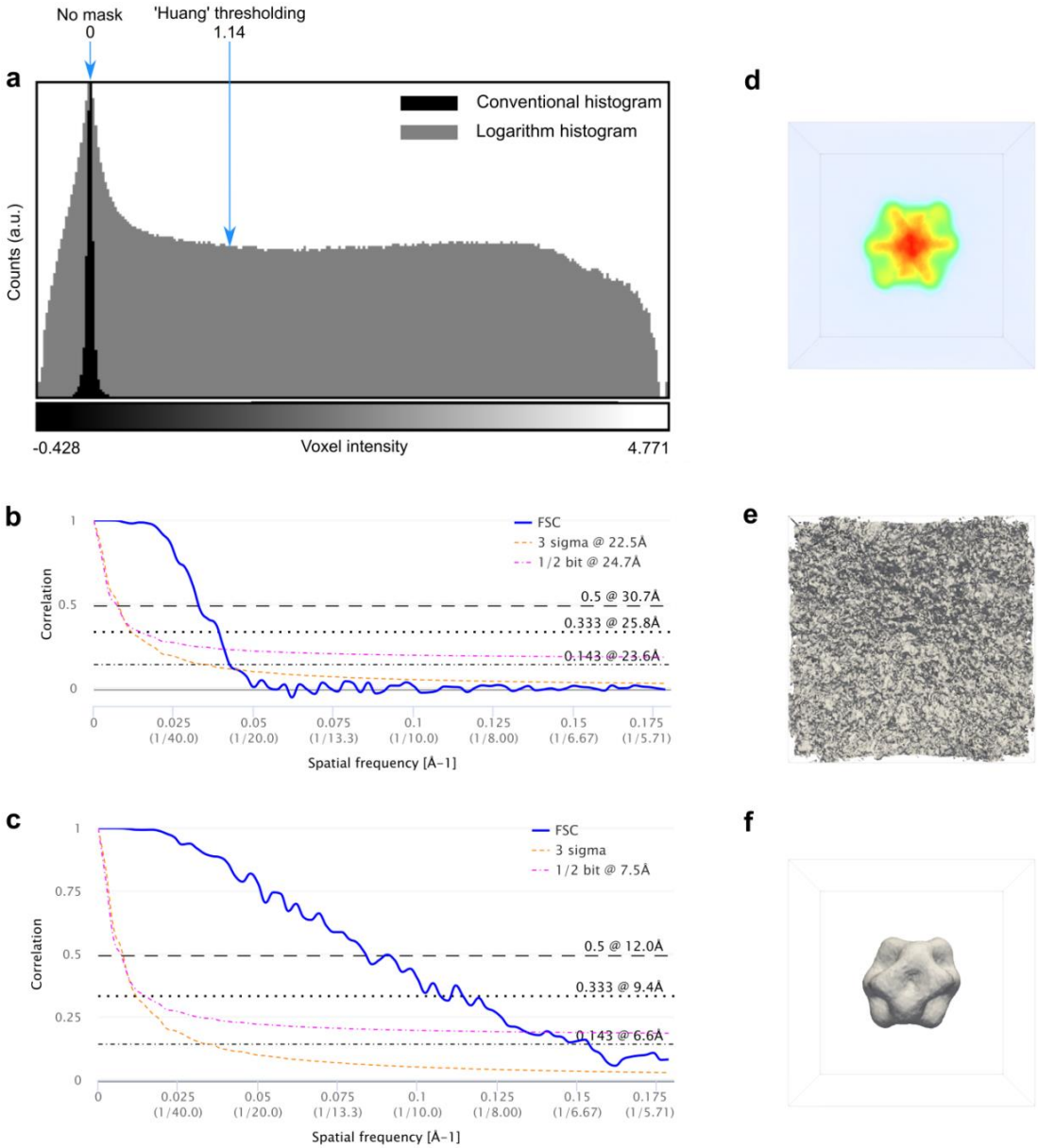

Figure S1: **Resolution analysis of 3D SPR HAADF intensity reconstructions evaluated by Fourier shell correlation.** a, Histograms of raw HAADF intensity reconstruction. b, FSC curves of unmasked HAADF data sets. c, FSC curves of thresholded HAADF data sets. The threshold value is indicated as 1.14 by an arrow in (a). d, 3D volume intensity displayed with a rainbow colour map, from blue (lowest intensity) to red (highest intensity). e, Surface render of unmasked reconstruction (displayed by setting threshold value as 0 to eliminate the negative voxel value artefacts due to the interpolation in reconstruction). This shows the artefacts cover the whole space of the reconstruction. f, Surface render of the thresholded reconstruction to show the absence of artefacts.

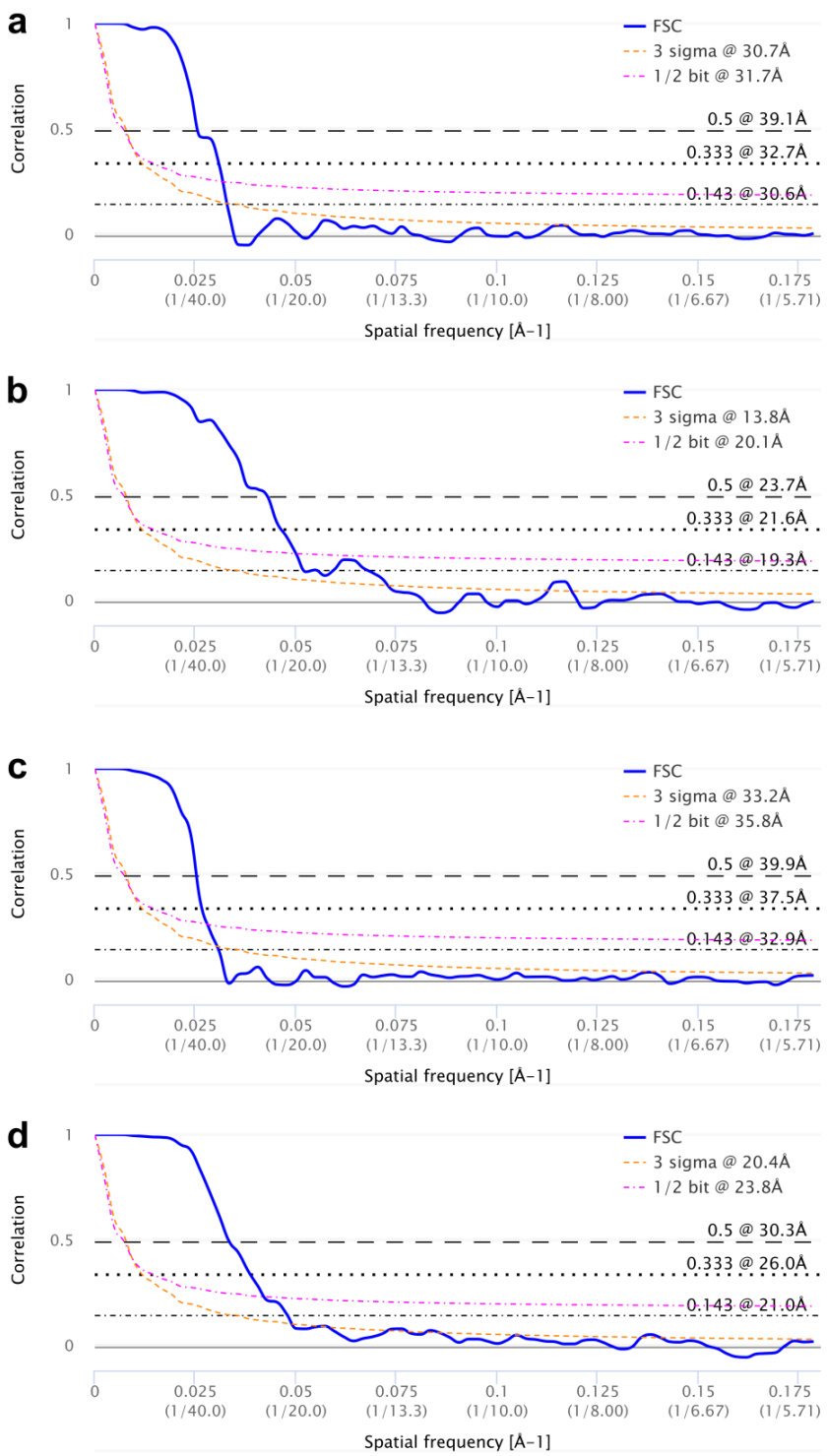

Figure S2: FSC curves of STEM-EDS intensity reconstructions. a and b, EDS Pt intensity reconstruction assessed by FSC using unmasked data sets and data sets masked with reference to the HAADF reconstruction thresholded at 1.14. c and d, EDS Ni intensity reconstruction assessed by FSC using unmasked data sets and data sets masked by HAADF reconstruction thresholded at 1.14.

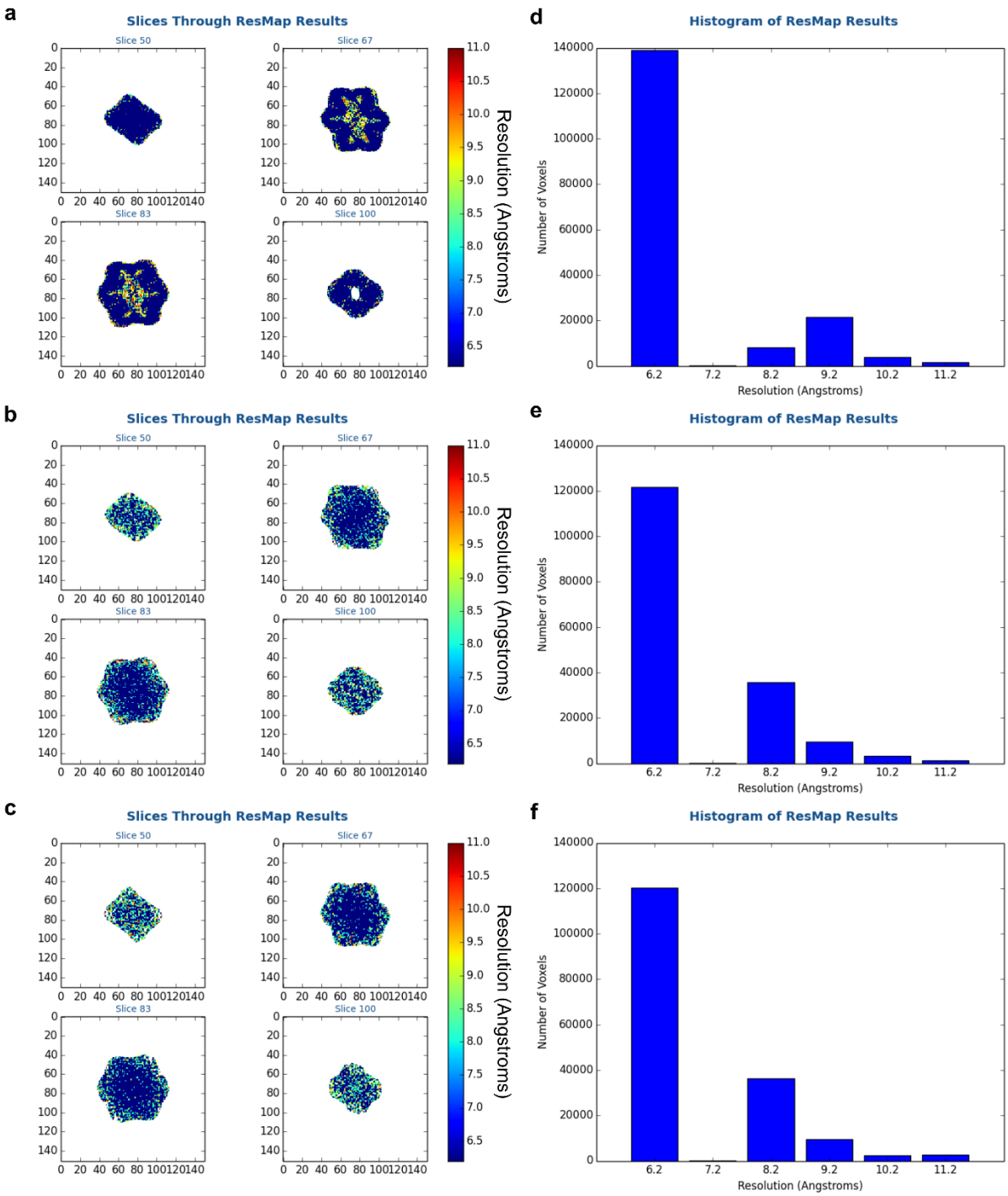

Figure S3: Resolution analysis of unprocessed 3D SPR intensity reconstructions evaluated by ResMap method.[23] **a-c**, Local resolution of 4 slices taken from 3D HAADF (**a**), EDS Pt (**b**) and EDS Ni (**c**) intensity reconstructions, respectively. **d-f**, Histograms of determined voxel resolution for 3D HAADF (**d**), EDS Pt (**e**) and EDS Ni (**f**) intensity reconstructions, respectively.

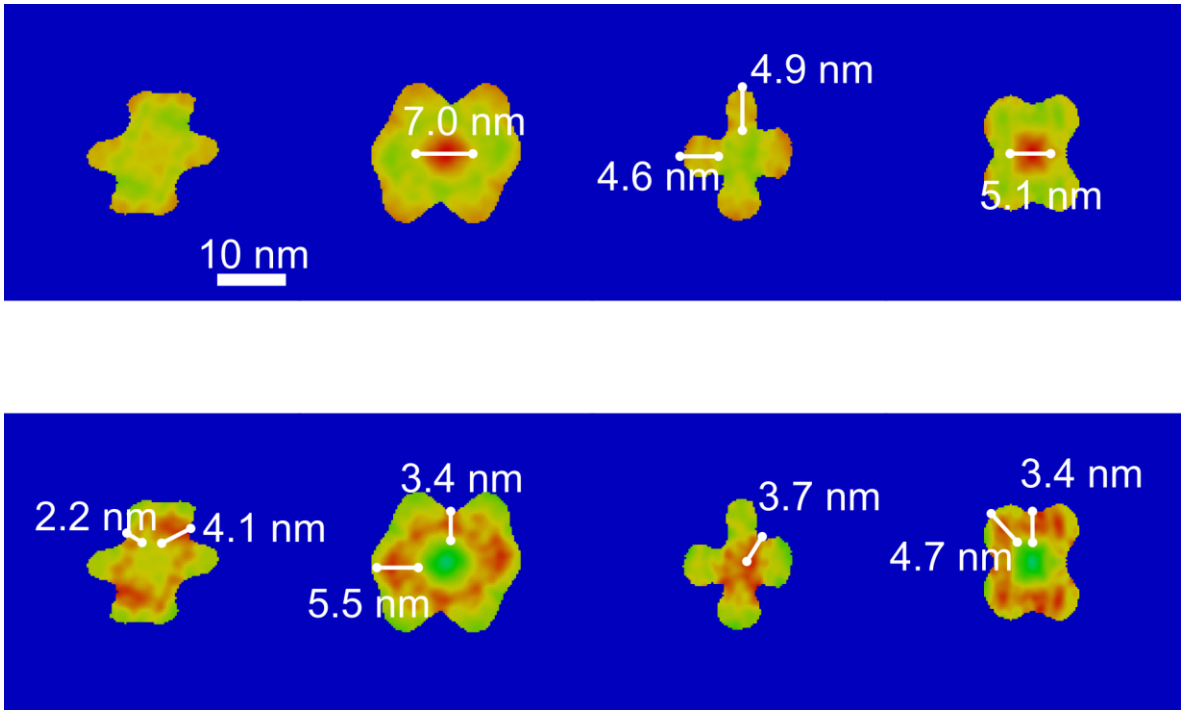

Figure S4: Size analysis of composition segregation features. Images in the first and second row correspond to Figure 4 c and d in the main text.

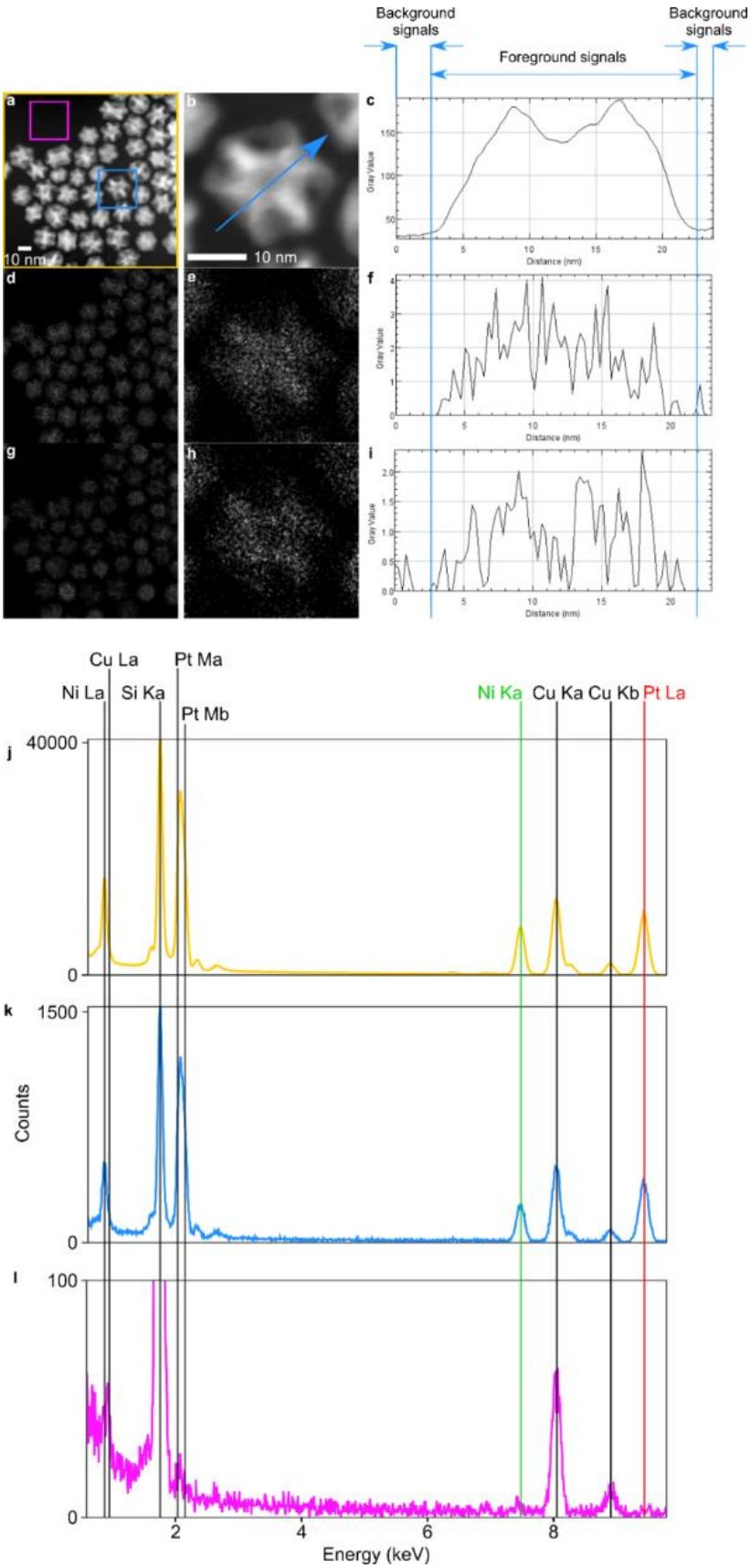

Figure S5. Illustration of HAADF signals and EDS spectra in unprocessed data used for SPR. a, d and

g, Unprocessed survey images of STEM HAADF, STEM EDS Pt Lα and STEM EDS Ni Kα X-rays, respectively. **b, e and h**, Enlarged image of blue framed region in **(a)** showing a single particle for the STEM HAADF image, and for the STEM EDS Pt Lα and EDS Ni Kα X-ray maps, respectively. **c, f and i**, Intensity line scans extracted from **(b), (e)** and **(h)**, respectively. The line scan position has been highlighted by a blue arrow in **(b). j, k, and l**, Summed EDS spectra of all pixels in the yellow, blue and magenta frames highlighted in **(a)**. No Ni Kα and Pt Lα peaks appear in **(l),** indicating that there are no spurious X-rays coming from the region where no sample is present.

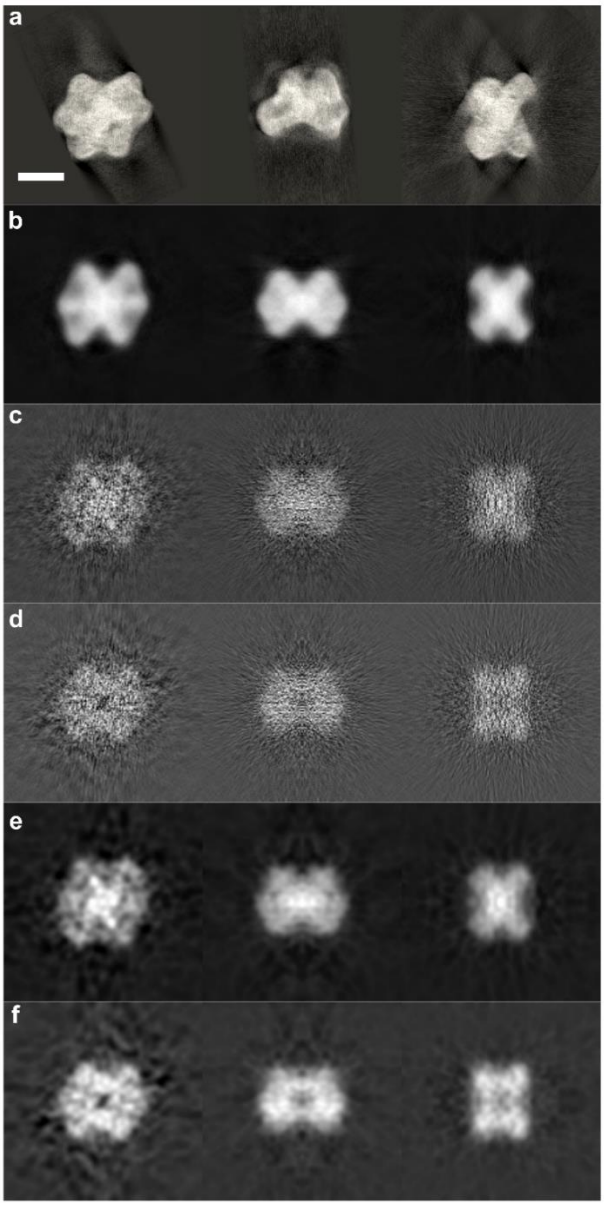

Figure S6: Orthoslices through raw reconstructions. a and **b,** Orthoslices of the unprocessed 3D reconstructions obtained by **a,** HAADF STEM tilt series tomography, **b** HAADF STEM SPR of particles with a composition of 55-65 at% Pt. The intensity range in **(a)** and **(b)** displays the minimum to maximum pixel intensities. The streaks indicate the reconstruction artefacts due to the missing information present in tilt series reconstruction **(a)**. Artefacts are reduced when reconstruction is performed using SPR in **(b). c** and **d,** STEM EDS Pt and Ni intensity respectively (from SPR of particles with a composition of 55-65 at% Pt). **e** and **f,** Gaussian filtered (with sigma 2) versions of **(c)** and **(d)**.

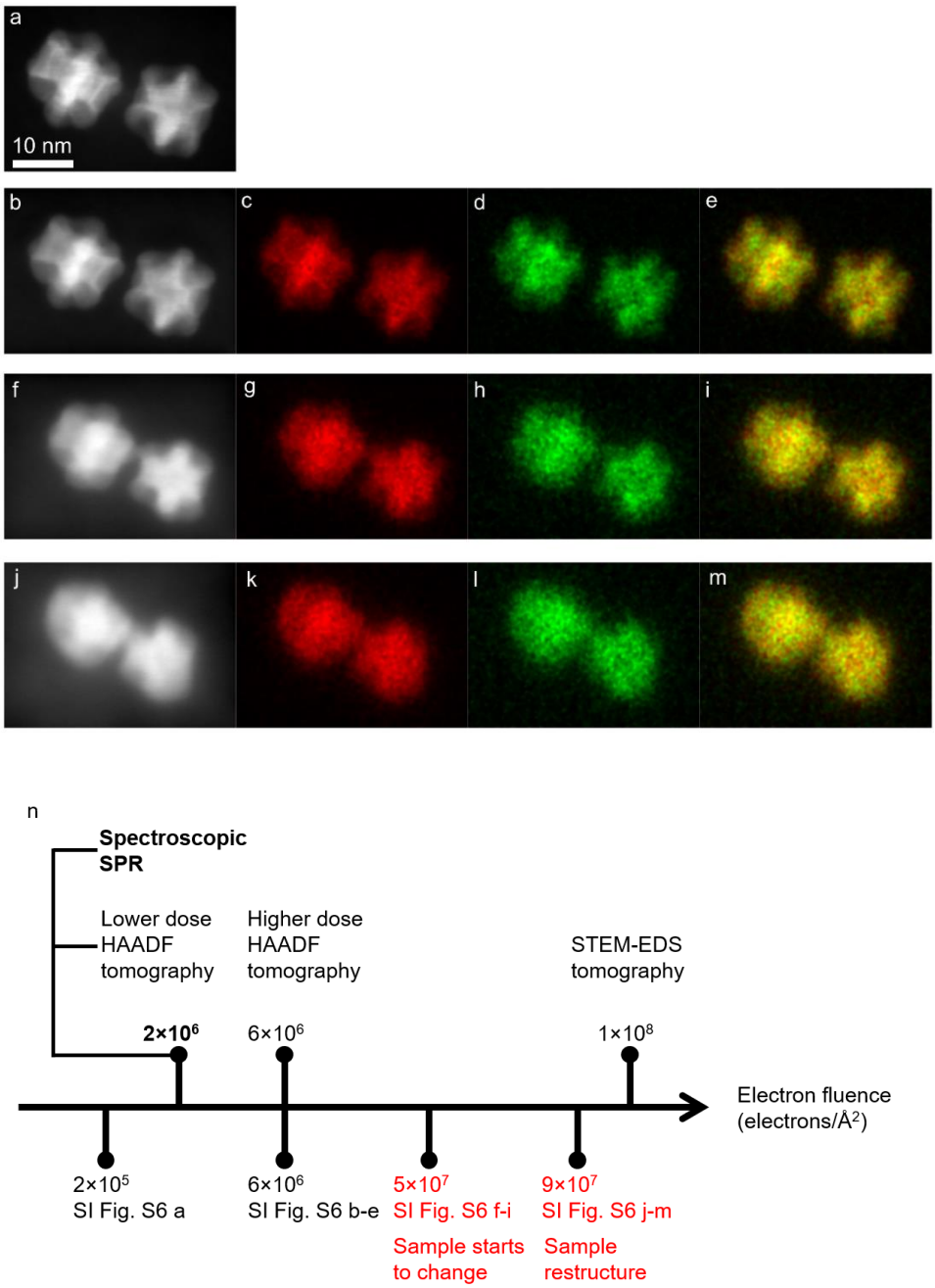

Figure S7: Illustration of electron beam damage of PtNi nanoparticles when exposed to excessive electron fluence. Data acquired after a, 2×10^5 electrons/Å^2, b-e, 6×10^6 electrons/Å^2, f-i, 5×10^7 electrons/Å^2 and j-m, 9×10^7 electrons/Å^2. (a), (b), (f) and (j) STEM HAADF images. (c), (g) and (k) elemental maps for Pt. (d), (h) and (l) elemental maps for Ni. (e), (i) and (m) composite elemental maps for Pt+Ni. (c-e), (g-i) and (k-m) are extracted from STEM EDS spectrum images. n, comparison of different electron fluence values.

Table S1: Electron fluence used by different techniques for imaging at a resolution on the order of 1 nm.

Approach	Approximate total electron fluence (e/Å^2)	Signal type	Beam current (pA)	Dwell time (µs)	Pixel size (Å)	Number of frames per acquisition	Number of acquisitions per particle
Spectroscopic single particle reconstruction	**2×10^6**	**STEM-EDS**	**520**	**190**	**2.8**	**24**	**1**
STEM-EDS tomography (SNR equivalent to spectroscopic SPR)	9×10^8	STEM-EDS	520	190	2.8	24	475
Normal STEM-EDS tomography (tilt range ±70° with 2.5° tilt increments)	1×10^8	STEM-EDS	520	190	2.8	24	56
Lower fluence HAADF tomography	2×10^6	HAADF	180	10	0.7	1	91
Higher fluence HAADF tomography	6×10^6	HAADF	520	10	0.7	1	91

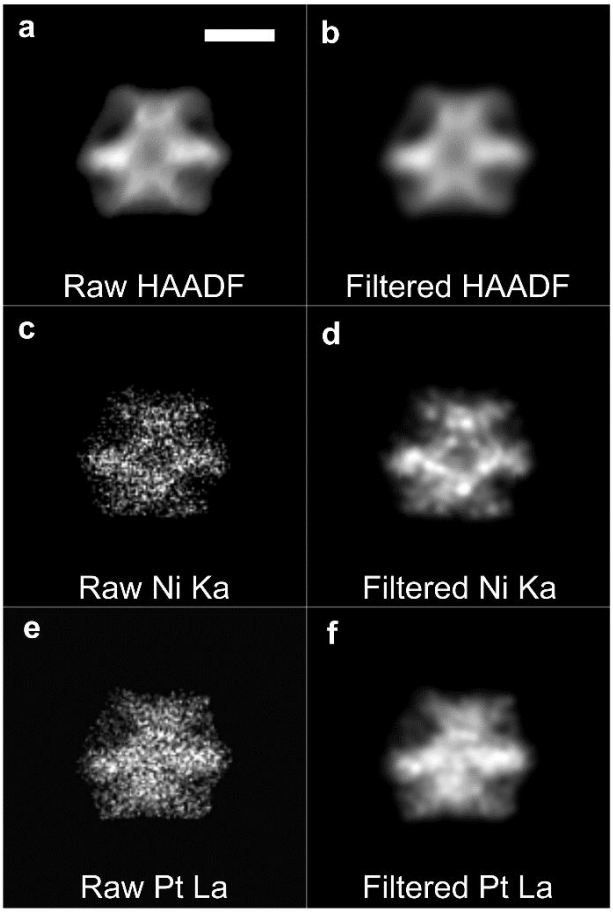

Figure S8: 2D images of a segmented individual nanoparticle. a, Raw STEM HAADF image after particle segmentation. b, Gaussian filtered (sigma 2) STEM HAADF image. c and e, Raw STEM EDS map for Ni Kα or Pt Lα X-rays, respectively, after particle segmentation. d and f, Gaussian filtered (sigma 2) image of (c) or (e), respectively. Scale bar is 10 nm.

Table S2: Quantification of size and composition of PtNi nanoparticle population.

	Feret diameter		Composition	Number
	Minimum to maximum (nm)	Mean ± Std (nm)	Mean ± Std (at% Pt)	of Particles
All NPs	13.4–37.4	19.7 ± 2.3	56 ± 6	1056
55-65 at% Pt	14.1–37.4	20.0 ± 2.3	59 ± 3	698
45-55 at% Pt	13.4–35.2	19.0 ± 2.1	51 ± 2	314
Used for SPR in main text (55-65 at% Pt, Fig. 4.)	15.7–36.2	20.0 ± 1.9	59 ± 3	475
Used for SPR in supporting information (45-55 at% Pt, Fig. S16.)	15.8–24.8	19.2 ± 1.7	51 ± 2	198

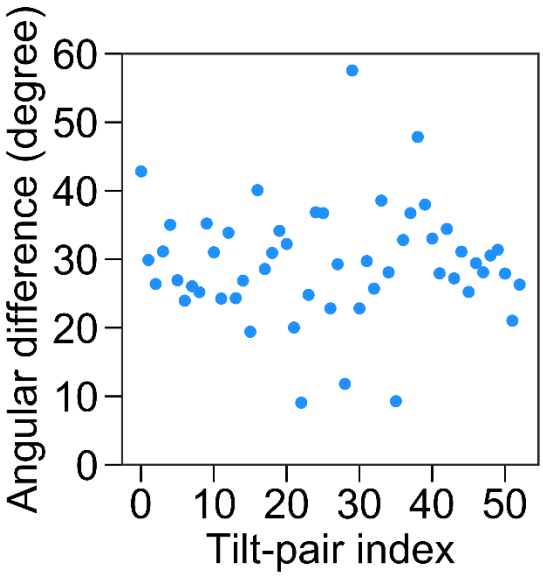

Figure S9: Angular differences of the tilt-pair orientations assigned by cross-correlation matching. The relative orientations of each tilt-pair were obtained taking into account the 24 octahedral symmetry transformations. The matched cross correlation coefficient values are usually in the range 0.92-0.98.

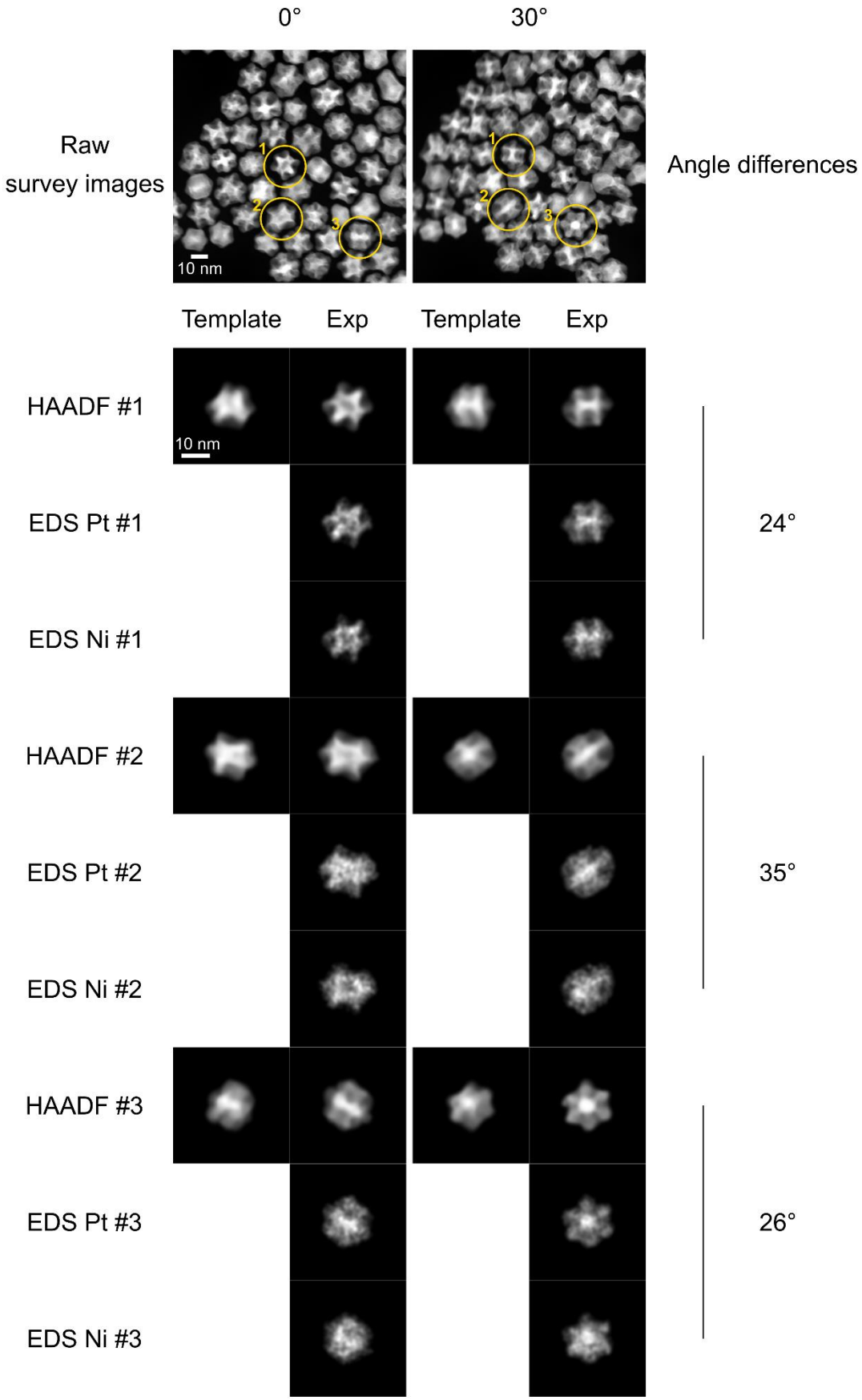

Figure S10: Illustrative tilt-pair matches.

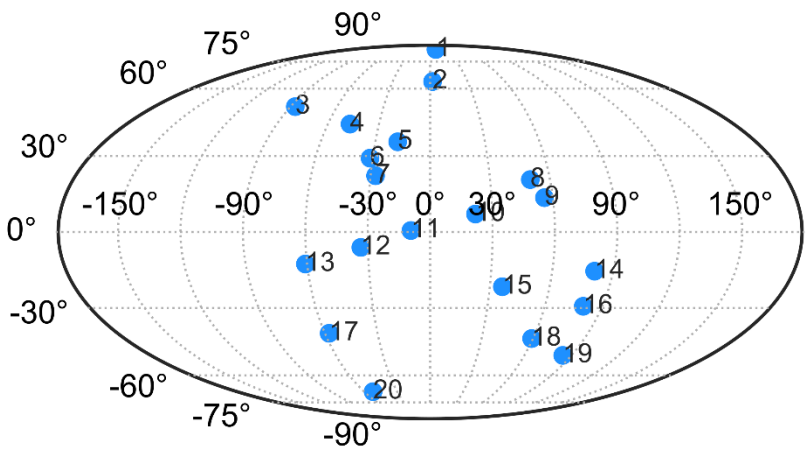

Figure S11: Angular position of 20 illustrative class averages used in SPR. Examples of particles from each class are shown in figures S1121 - 15. Numbers shown next to points on this figure indicated the numbering used in Figs. S12 - S15.

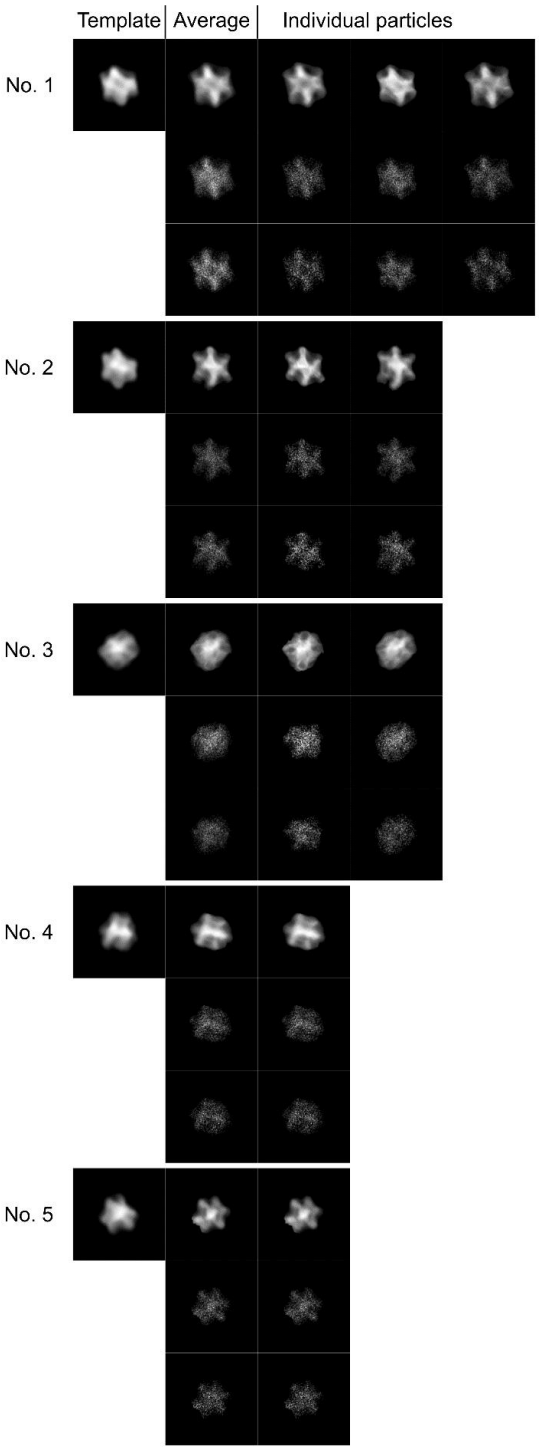

Figure S12: Matched templates (left hand column) and class averages used for SPR and individual particles assigned to the class by template matching. In each class average, rows are top to bottom: STEM HAADF, STEM EDS Pt and STEM EDS Ni signals, respectively. This figure presents the class averages from No.1 to 5, the orientations of which are shown in Figure S11.

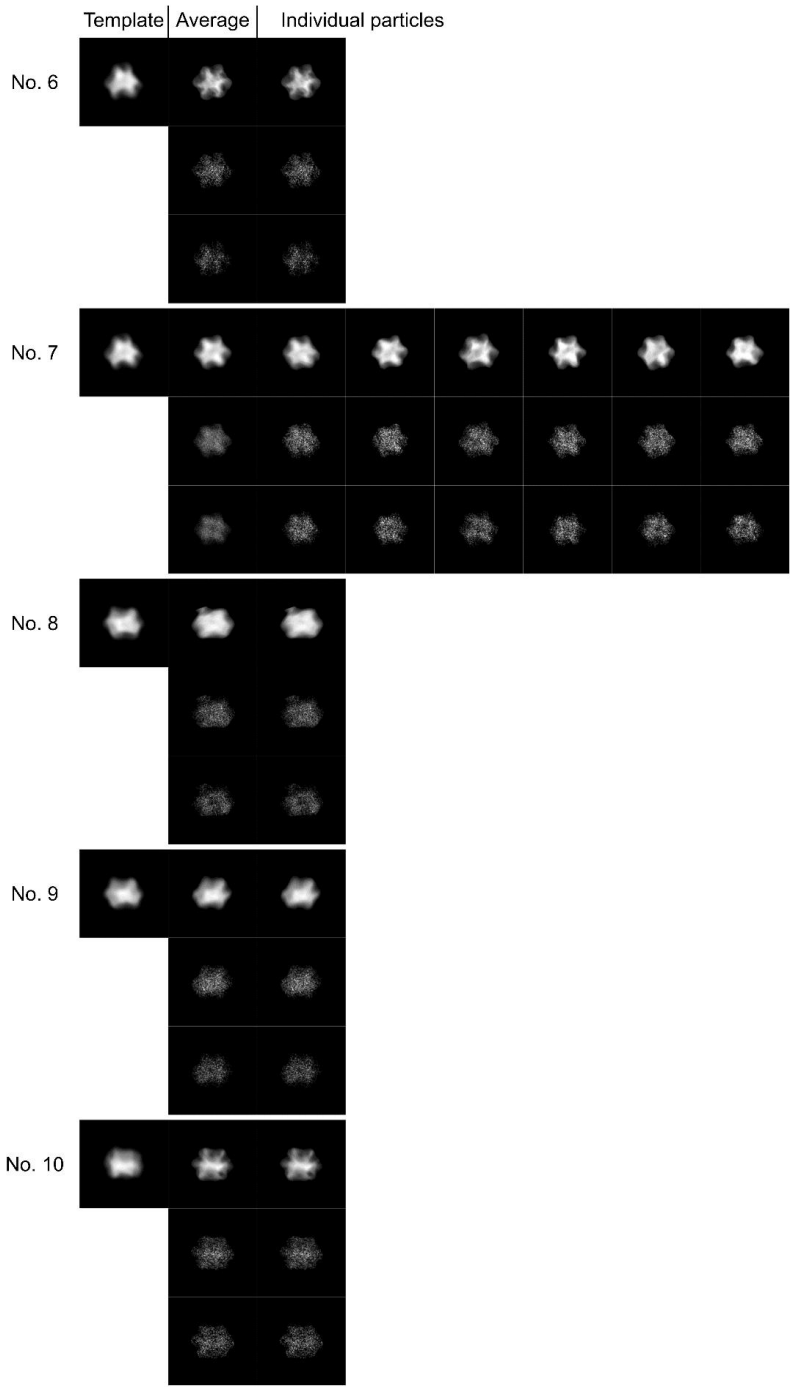

Figure S13: Matched templates (left hand column) and class averages used for SPR and individual particles assigned to the class by template matching. In each class average, rows are top to bottom: STEM HAADF, STEM EDS Pt and STEM EDS Ni signals, respectively. This figure presents the class averages from No.6 to 10, the orientations of which are shown in Figure S11.

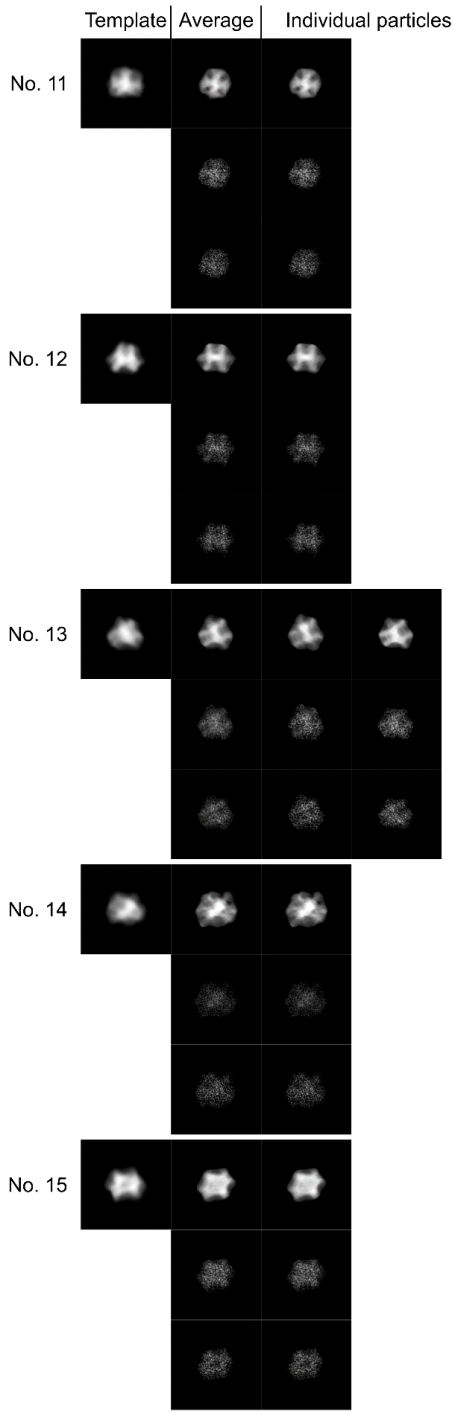

Figure S14: Matched templates (left hand column) and class averages used for SPR and individual particles assigned to the class by template matching. In each class average, rows are top to bottom: STEM HAADF, STEM EDS Pt and STEM EDS Ni signals, respectively. This figure presents the class averages from No.11 to 15, the orientations of which are shown in Figure S11.

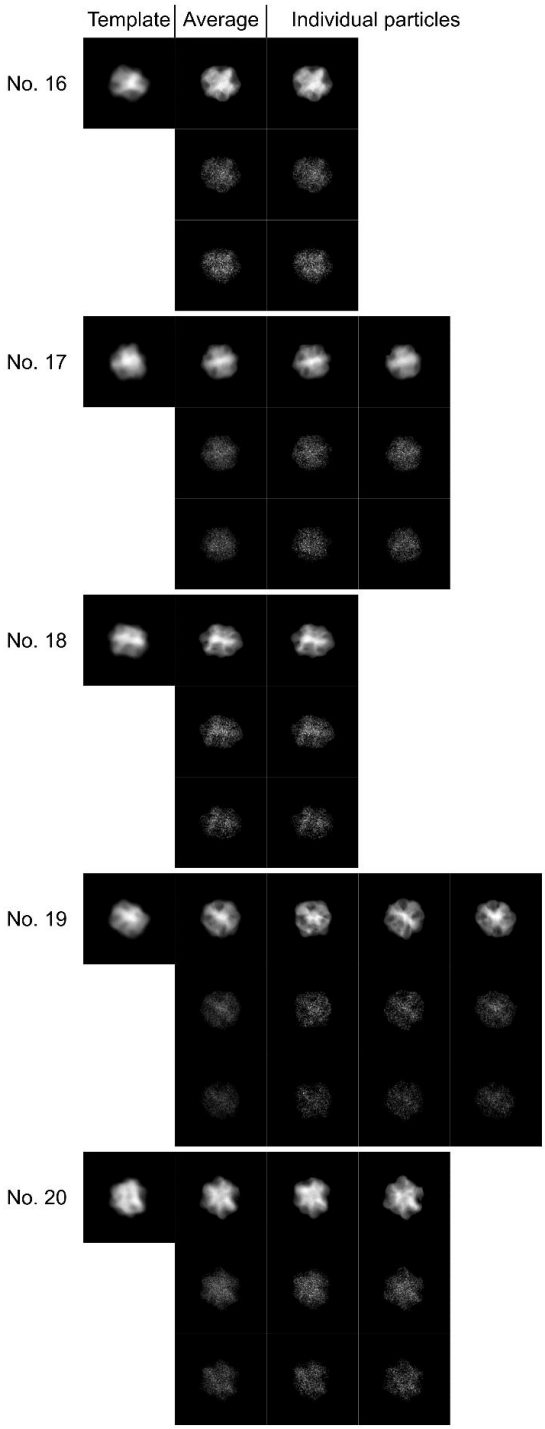

Figure S15: Matched templates (left hand column) and class averages used for SPR and individual particles assigned to the class by template matching. In each class average, rows are top to bottom: STEM HAADF, STEM EDS Pt and STEM EDS Ni signals, respectively. This figure presents the class averages from No.16 to 20, the orientations of which are shown in Figure S11.

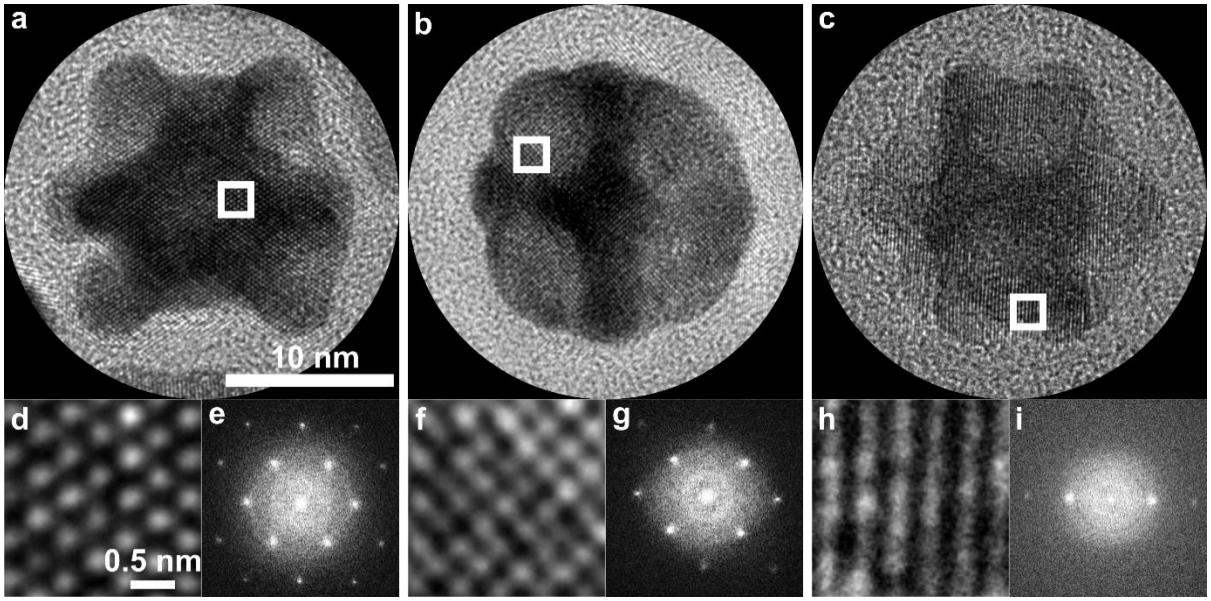

Figure S16: High resolution TEM (HRTEM) images illustrating the crystallographic orientation of PtNi nanocrystals. a-c, HRTEM images of PtNi nanoparticles oriented along <110>, <100> and <113> directions. d, f, and h, Enlarged regions showing lattice detail for regions marked by white squares in (a-c), respectively. e, g and i, Fourier transforms (FT) of (a-c), respectively.

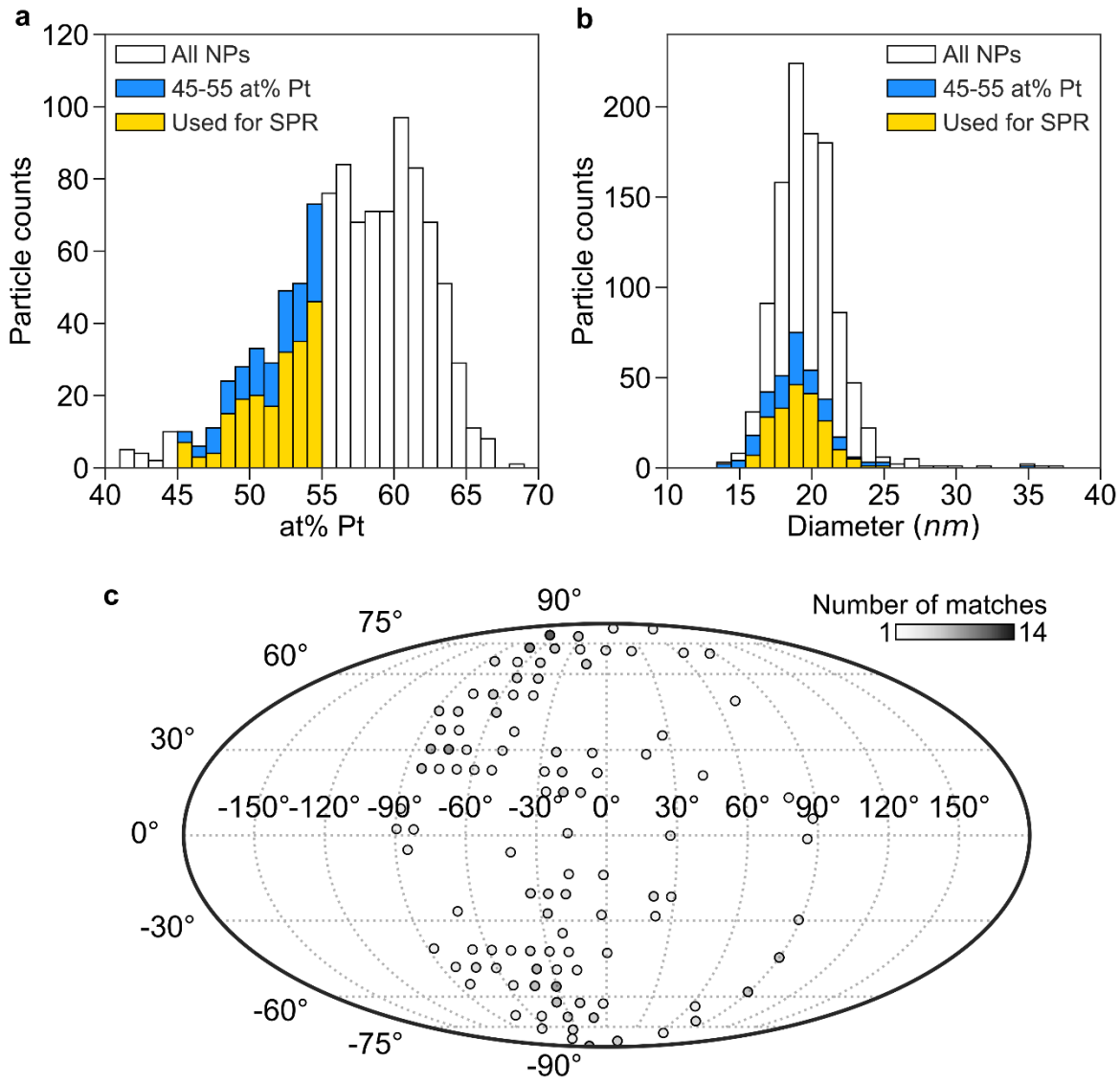

Figure S17: Composition, Feret diameter and angular coverage distribution of PtNi nanoparticles with compositions of 45-55 at% Pt.

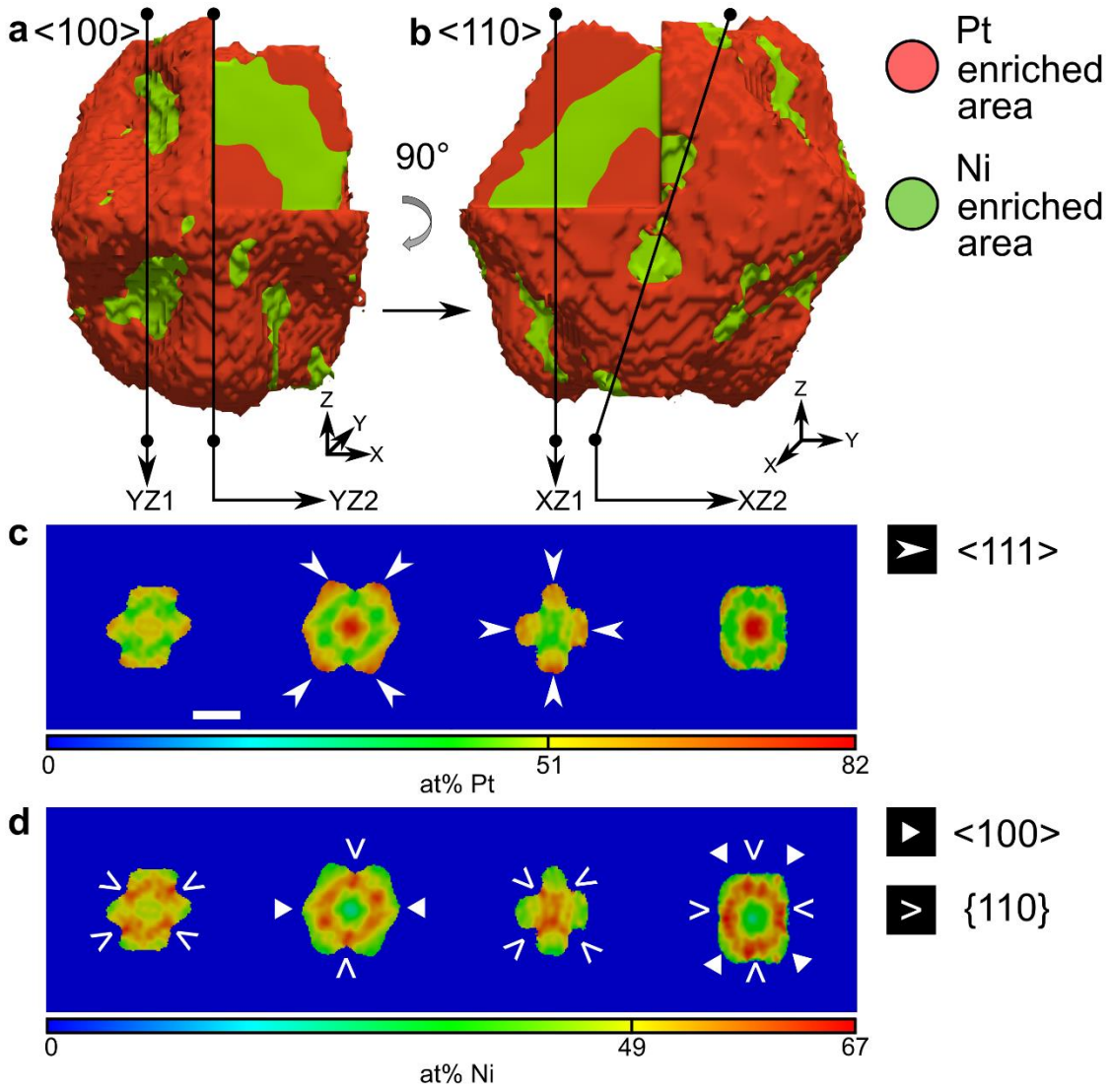

Figure S18: 3D chemical distribution obtained using spectroscopic SPR for particles with composition 45-55 at% Pt. a and b, The quantitative SPR elemental reconstruction thresholded above 51 at% Pt (red) and 49 at% Ni (green) and viewed along <100> and <110> directions, respectively. One eighth is cut from each reconstruction to reveal the internal elemental distribution. c and d, Slices through the at% distributions for Pt and Ni, respectively. Elemental enrichment on the <111> vertices, {110} facets and <100> vertices are indicated by different arrows. Scale bar is 10 nm.

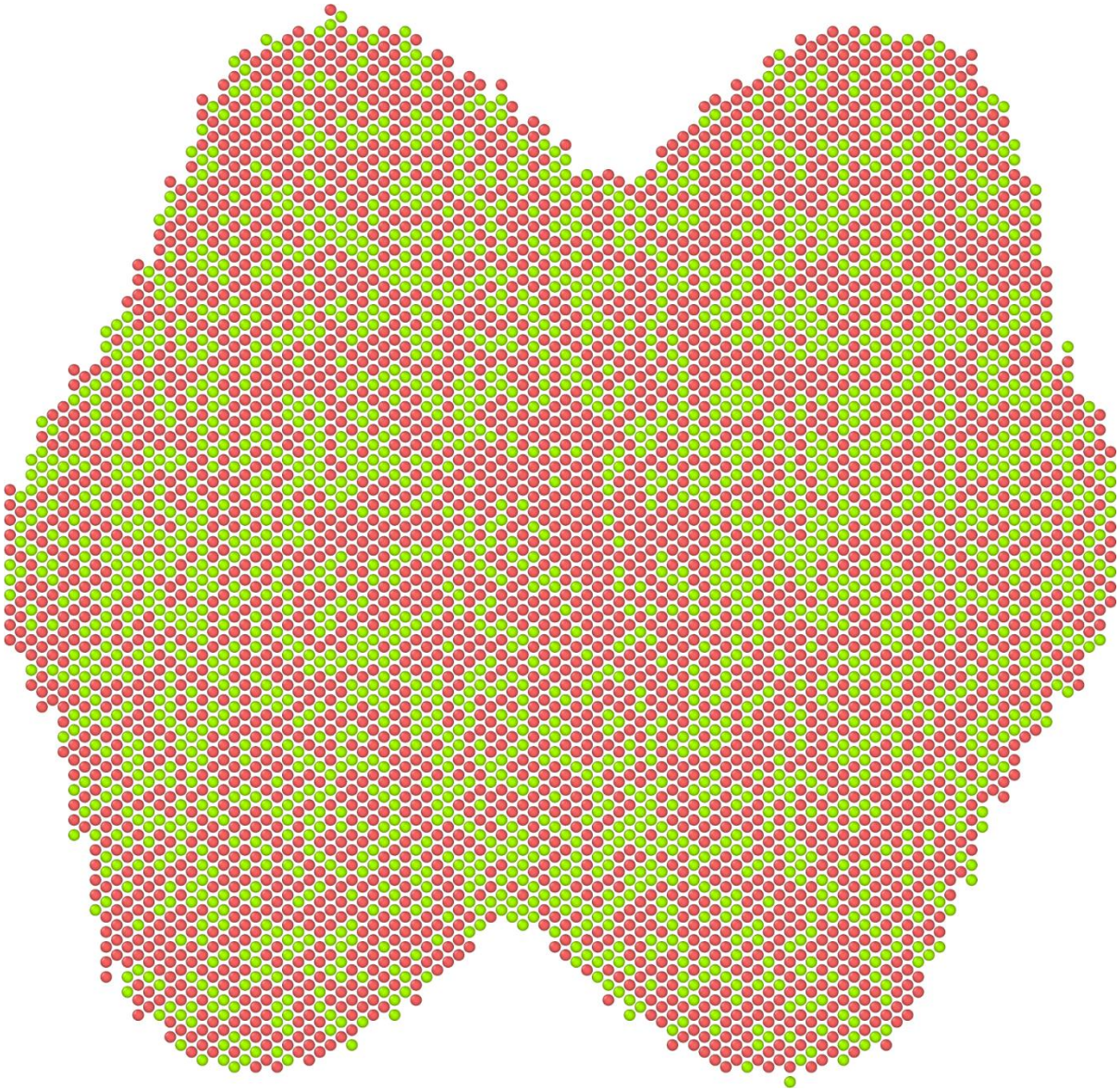

Figure S19: Enlarged view of Figure 4 e from the main text.

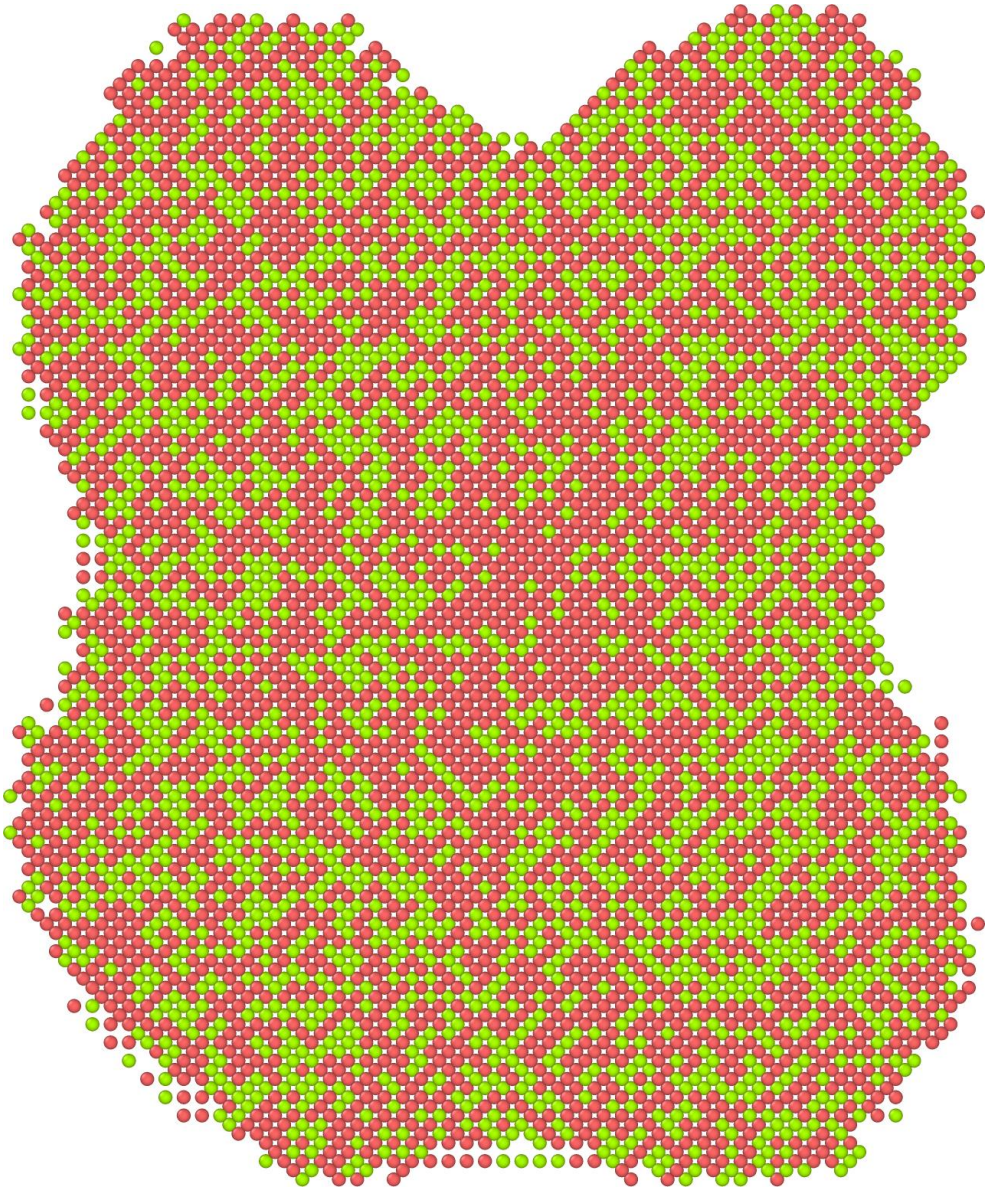

Figure S20: Enlarged view of Figure 4 f from the main text.

References

1. Chen, C.; Kang, Y.; Huo, Z.; Zhu, Z.; Huang, W.; Xin, H. L.; Snyder, J. D.; Li, D.; Herron, J. A.; Mavrikakis, M.; et al. *Science* **2014**, *343*, 1339–1343.

2. Slater, T. J. A.; Janssen, A.; Camargo, P. H. C.; Burke, M. G.; Zaluzec, N. J.; Haigh, S. J. *Ultramicroscopy* **2016**, *162*, 61–73.

3. Sternberg, S. R. *Computer* **1983**, *16***,** 22–34.

4. Schindelin, J.; Arganda-Carreras, I.; Frise, E.; Kaynig, V.; Longair, M.; Pietzsch, T.; Preibisch, S.; Rueden, C.; Saalfeld, S.; Schmid, B.; et al*. Nat. Methods* **2012,** *9***,** 676–682.

5. Huang, L.-K.; Wang, M.-J. J. *Pattern Recognit.* **1995**, 41–51.

6. Gonzales, R. C. & Woods, R. E. *Digital image processing* Prentice Hall, **2007**.

7. de la Peña, F.; Ostasevicius, T.; Fauske, V. T.; Burdet, P.; Prestat, E.; Jokubauskas, P.; Nord, M.; MacArthur, K. E.; Sarahan, M.; Johnstone, D. N.; et al*. hyperspy: HyperSpyv1.4.* **2018**. doi:10.5281/zenodo.46897

8. van Aarle, W; Palenstijn, W. J.; De Beenhouwer, J.; Altantzis, T.; Bals, S.; Batenburg, K. J.; Sijbers, J. *Ultramicroscopy* **2015** *157***,** 35–47.

9. Tang, G.; Peng, L;, Baldwin, P.R.; Mann, D.S.; Jiang, W.; Rees, I.; Ludtke, S.J., *J. Struct. Biol.***2007**, *157***,** 38–46.

10. Baldwin, P. R.; Penczek, P. A. *J. Struct. Biol.* **2007**, *157***,** 250–261.

11. Williams, D. B.; Carter, C. B. *Transmission Electron Microscopy: A Textbook for Materials Science* Springer, **2009**.

12. Levin, B.D.; Jiang, Y.; Padgett, E.; Waldon, S.; Quammen, C.; Harris, C.; Ayachit, U.; Hanwell, M.; Ercius, P.; et al... *Micros. Today*, **2018**,*26***,** 12–17.

13. Davey, W. P. *Phys. Rev.* **1925**, *25***,** 753–761.

14. Stukowski, A. *Model. Simul. Mater. Sci. Eng.***2010***, 18*.

15. van Heel, M.;Harauz, G. *Optik* **1986,** *73***,** 119–122.

16. Stewart, P. L.; Chiu, C. Y.; Haley, D. A; Kong, L. B.; Schlessman, J. L. *J. Struct. Biol.* **1999,** *128***,** 58–64.

17. Rosenthal, P. B.; Henderson, R.*J. Mol. Biol.* **2003**, *333***,** 721–745.

18. Van Heel, M.; Schatz, M. *J. Struct. Biol.* **2005**, *151***,** 250–262.

19. Liao, H. Y.; Frank, J. *Structure* **2010**, *18,* 768–775.

20. Penczek, P. A. *Methods in Enzymology* Elsevier Inc., **2010**.

21. Henderson, R.; Sali, A.; Baker, M.L.; Carragher, B.; Devkota, B.; Downing, K.H.; Egelman, E.H.; Feng, Z.; Frank, J.; Grigorieff, N.; et al.. *Structure* **2012**, *20,* 205–214.

22. Chen, S.; McMullan, G.; Faruqi, A.R.; Murshudov, G.N.; Short, J.M.; Scheres, S.H.; Henderson, R. *Ultramicroscopy* **2013**, *135,* 24–35.

23. Kucukelbir, A.; Sigworth, F. J.; Tagare, H. D. *Nat. Methods* **2014**, *11,* 63–65.

24. Frank, J. *Nat. Protoc.***2017**, *12***,** 209–212.

6. Towards in-situ 3D imaging of nanoparticles using single particle reconstruction

6.1. Introduction

This chapter extends the applicability of SPR to a new dimension to investigate the 3D structural and elemental transformation in-situ at heating temperatures. Although only one data set presented in this chapter, multiple preliminary in-situ heating tests were performed to find a suitable temperature range and heating time. The dimensionality of the as-collected raw data set also increases as same area has to be imaged at several steps. In-house python scripts were used to sort data sets. The current results show that at each heating temperature HAADF 3D reconstruction can be faithfully performed while corresponding EDS maps cannot due to low SNR. The results shows here demonstrate the potential to use SPR approach to reconstruct a series of 3D structure and compositional distribution along time and extra stimuli at more challenging environments when TS-ET is not applicable.

Dr Thomas Slater, Dr Sarah Haigh and I conceived the idea. Dr Gerard Leteba and Dr Candace Lang provide the nanoparticle. I did the rest of the work and wrote the manuscript with inputs from Dr Thomas Slater and Dr Sarah Haigh.

Paper: Towards in-situ 3D imaging of nanoparticles using single particle reconstruction

Yi-Chi Wang[1], Thomas J A Slater*[2], Gerard Leteba[3], Candace Lang[4], Sarah J Haigh*[1]

1. School of Materials, University of Manchester, Oxford Road, Manchester, M13 9PL, U.K.

2. Electron Physical Sciences Imaging Centre, Diamond Light Source Ltd., OX11 0DE, U.K.

3. Catalysis Institute, Department of Chemical Engineering, University of Cape Town, Corner of Madiba Circle and South Lane, Rondebosch 7701, South Africa

4. School of Engineering, Macquarie University, NSW 2109 Australia

*Sarah.haigh@manchester.ac.uk, *Thomas.slater@diamond.ac.uk

Abstract

In-situ scanning transmission electron microscopy for imaging the transformation of inorganic nanoparticles at varying environments could provide distinctive knowledge compared to conventional ex situ studies. Single particle reconstruction is a widely used 3D reconstruction approach for imaging the structure of biological molecules, with each particle experiencing minimal electron dose. Here we demonstrate that this approach can also be applied to reduce the requirements for high electron fluence when performing in situ analysis of inorganic nanoparticles. Using PtNi nanoparticles as an example, combined with a commercial in situ heating holder, we show that the single particle reconstruction methodology has the potential to image the 3D structural and elemental redistribution pathway of nanoparticles during heating to elevated temperatures.

1. Introduction

Combining multiple elements in inorganic nanoparticles is a proven route to achieve higher catalytic activity and low costs[1–3]. Revealing the three-dimensional (3D) morphology and elemental distribution in these nanoparticles is vital to the understanding of their structure-property relationships. Conventional 3D characterisation of nanoparticles in the transmission electron microscope (TEM) or scanning transmission electron microscope (STEM) are performed in static, high vacuum and room temperature environments. Recently, in situ holders are becoming mature and commercially available[4–6], as well as the environmental TEM (ETEM) equipped with a differentially-pumped objective lens[7], both of which provide the opportunity to characterise the evolution of nanoparticles under additional environmental stimuli.

Tilt-series electron tomography (TS-ET) is one of the most popular methods to perform 3D imaging[8,9] and has recently demonstrated its applicability to in-situ 3D imaging[10–16]. This method requires imaging the same specimen many times by usually tilting the holder to around ±75° and collecting data at each tilt angle. This tilt series dataset can then be used to reconstruct the 3D distribution of some property of the specimen through established tomographic algorithms[17]. Depending on the types of signals collected, bright field TEM (BF-TEM)[18] or high angle annular dark field STEM (HAADF-STEM)[19] are usually used to reconstruct the 3D morphology, while spectroscopic data such as energy dispersive X-ray spectroscopy [20] or electron energy loss spectroscopy[21] are used for reconstruction of the 3D elemental distribution. Zhou et al. used a normal high angle tilt holder to perform atomic resolution HAADF 3D reconstruction of the same FePt nanoparticle after heating ex-situ in an oven at 520°C for 9, 16 and 26 minutes respectively[10]. They tracked every atom position at the three heating times and found nuclei for the solid-solid phase transitions undergoing growth, shrinkage or dimensional fluctuation. However, they did not simultaneously heat and image the same particle inside microscope because standard in situ heating holders can usually be tilted to only 30°, which severally reduces reconstruction quality. Baaziz et al. also performed TS-ET before and after the same specimen had been subjected to different gaseous environments to study the morphology and faceting change of Pd@SiO2 core shell nanostructures[11].

If an in-situ holder can be tailored to allow a high tilt range, in-situ TS-ET is achievable. The design of heating holders has shifted from a tungsten filament heating system[22] to microelectromechanical systems (MEMS) based holders with better stability and temperature control[23]. Utilising the combination of a high tilt heating holder and ETEM, Epicier et al. have performed TS-ET using BF-TEM in an ETEM to study the thermally induced structural change for a series of supported NP catalysts with distinct atomic differences[12–14]. In addition to the in situ 3D structural imaging, they proposed fast rotation acquisition methods to continuously rotate the holder while recording data to improve the temporal resolution of one full range tilt series data to about 2 minutes[13].

Extending the fast rotation acquisition scheme to HAADF-STEM signals, the overall structural change of Au[15] or Au/Pd alloyed nanoparticles[16] as a function of heating temperature have both been investigated. Combined with boundary element method simulation, it found curvature induced surface diffusion drives the reshape of sharp Au tips to blunter tips[15]. Au/Pu octopods were found to maintain strong plasmon resonance and shape stability up to 600°C.

Atom counting is another method capable of performing 3D atomic reconstruction of nanoparticles in gaseous environments[24]. Using a standard gas cell holder, atomic resolution HAADF images of Pt nanoparticles were captured in various gaseous environments. As the HAADF signal intensity of each atom column can be related precisely to the number of atoms under ideal conditions[25], a 3D distribution of each atomic column can then be reconstructed to show the dominant facet of Pt nanoparticles are cycling from {100} and {111} planes to higher order facets when switching the gas from H_2 to O_2[24].

However, the aforementioned methods only track the evolution of one or of a few particles, which limits the sampling quantities and therefore whether the transformation identified is applicable to the whole population of nanoparticles. In addition, special in situ holders are required to allow TS-ET to be tilted to high angles. Furthermore, imaging the same specimen many times at every tilt angle

requires high electron dose and hinders the characterisation of beam sensitive nanoparticles, especially if collecting full tilt series data at every time step.

Spectroscopic single particle reconstruction (SPR) has recently been proposed for imaging 3D elemental distribution of beam sensitive bimetallic nanoparticles[26]. The method shares the same theory as conventional SPR used in biology to study the 3D conformation of macromolecules[27]. The SPR approach assumes the whole population of nanoparticles are identical and each particle is oriented randomly on the support. By imaging many particles using simultaneously acquired HAADF and EDS signals, with subsequent matching of each particle to reference images to obtain their orientation, the averaged 3D information of the nanoparticle population can be obtained.

An SPR acquisition scheme greatly increases the number of particles sampled and does not require a high tilt holder. Here, following our previous study on PtNi bimetallic nanoparticles, we demonstrate the potential of spectroscopic SPR to be used to reveal the 3D structural and compositional change during heating at different temperatures.

2. Experimental methods

2.1. In-situ heating experiment set up

PtNi nanoparticles were synthesised through a standard co-reduction between nickel acetatetetrahydrate and chloroplatinic acid solution in the presence of ternary hydrophobic surfactants oleylamine (OAm), octadecylamine (ODA) and oleic acid (OLEA), as detailed in previous work[26]. The as-synthesised nanoparticles were re-suspended in chloroform followed by 5 minutes sonification. A Protochips Fusion 500 double tilt heating holder and MEMS based heating chips (series number E-FHBS, covered by 40 nm thick continuous SiN support film) were used for deposition of the nanoparticle solution and to perform heating of the specimen inside the microscope.

To minimise the contamination during long acquisition times inside the microscope, heating chips were vacuum baked for 2 hours at 100°C and plasma cleaned for 5 minutes before the deposition of specimen. After drop-casting the specimen on heating chips, a few drops of methanol were also drop-cast onto the chip to increase nanoparticle dispersion and to prevent severe agglomeration of the nanoparticles. Heating chips were then vacuum baked for 12 hours at 100°C and plasma cleaned for 15 seconds and were then loaded onto the heating holder. The holder was loaded into the microscope 12 hours before the start of experiment to help reduce contamination in the microscope. Before data acquisition, a 30-minute beam shower was performed on viewing region.

2.2. STEM and EDS data acquisition

A Thermo Fisher Titan G2 80-200 S/TEM was used for HAADF and EDS data acquisition. The microscope was operated at 200 kV, with a beam current of 180 pA, equipped with an X-FEG high brightness source and STEM probe aberration corrector. All HAADF and EDS data were acquired at 225000X magnification with a full frame size of 1024 x 1024 pixels, resulting in a pixel size of 3.86 Å and a field of view of 395 nm.

For HAADF STEM imaging, a 21 mrad convergence angle and 55 mrad acceptance inner angle were used. HAADF images were acquired in the Thermo Fisher TIA software using a pixel dwell time of 20 µs. For EDS spectrum imaging, the Bruker Esprit software was used for data acquisition using a Super-X EDS detector system consisting of four silicon drift detectors (SDDs) with a total collection solid angle of approximately 0.7 sr. A pixel dwell time of 50 µs and 15 frames scanning were used for EDS spectrum data collection, resulting in a total pixel dwell time of 750 us. The EDS spectrometer was set to collect an energy range from 0-20 keV with 2048 channels.

At room temperature, six regions of interest (ROI) were selected for characterisation during heating. The selection criterion for the ROI was to ensure as many nanoparticles were included in the field of view as possible but without the individual particles overlapping. This ensured that the later particle extraction image processing steps can be easily performed and that the nanoparticles do not melt

into adjacent nanoparticles. Each region contains about 10 well dispersed nanoparticles, as demonstrated in Figure 1 a-c. The heat treatment was performed at 200°C, 250°C, 300°C, 350°C, 500°C, 450°C and 550°C with a heating ramp of 10 °C/s and a total heating time of 10 minutes at each step. After heat treatment, the specimen was quenched to room temperature instantly (cooling rate 100°C/s), then the 6 selected regions were characterised by HAADF and EDS.

2.3. 2D image processing

The as-collected data sets were 6 stacks of HAADF images with axes [x, y, temperature] and 6 stacks of EDS spectrum data with axes of [x, y, energy, temperature]. The inter-frame shifts between acquisitions at each temperature were calculated and minimised by cross correlating HAADF stacks according to their temperature axis. This alignment was also applied to the simultaneously acquired EDS data sets. Next, each nanoparticle was selected by manually picking the centre of particle using ImageJ[28] and cropping picked nanoparticles into a 100 x100 pixel box (Figure 1 d) using in-house python scripts.

After cropping each nanoparticle into a small box, the cropped areas were processed by the following procedures to isolate each particle: 1) using a “rolling ball” algorithm[29] in ImageJ[28] with a conservative parameter (rolling ball radius 50 pixels with the sliding paraboloid option enabled) to perform a background subtraction to correct the uneven background intensity; 2) a “Huang” thresholding algorithm[29] was performed to binarise foreground particle regions; 3) using a watershed segmentation algorithm to segment touching particles; 4) the final segmented particles (9 illustrative examples are shown in Figure 1 e) were binarised again and were used as masks to extract the particle region from raw EDS data; 5) the geometric centre of the segmented HAADF particle images was matched to the box’s centre, the same alignments were applied on corresponding EDS data; 6) using the HyperSpy python package[30], 2D EDS intensity maps were extracted at energies of 7.334–7.622 keV (Ni Kα) and 9.281–9.603 keV (Pt Lα); 7) each HAADF particle image and their EDS maps were normalised to ensure the pixel values in each image have a

mean of 0 and a standard deviation of 1 (Figure 1 f shows 9 illustrative examples of intensity normalised HAADF particle images with a 2-pixel Gaussian smoothing). The processed HAADF images were used for orientation matching with reference re-projections generated from reference 3D data discussed further in sections 2.4.1 and 2.4.2.

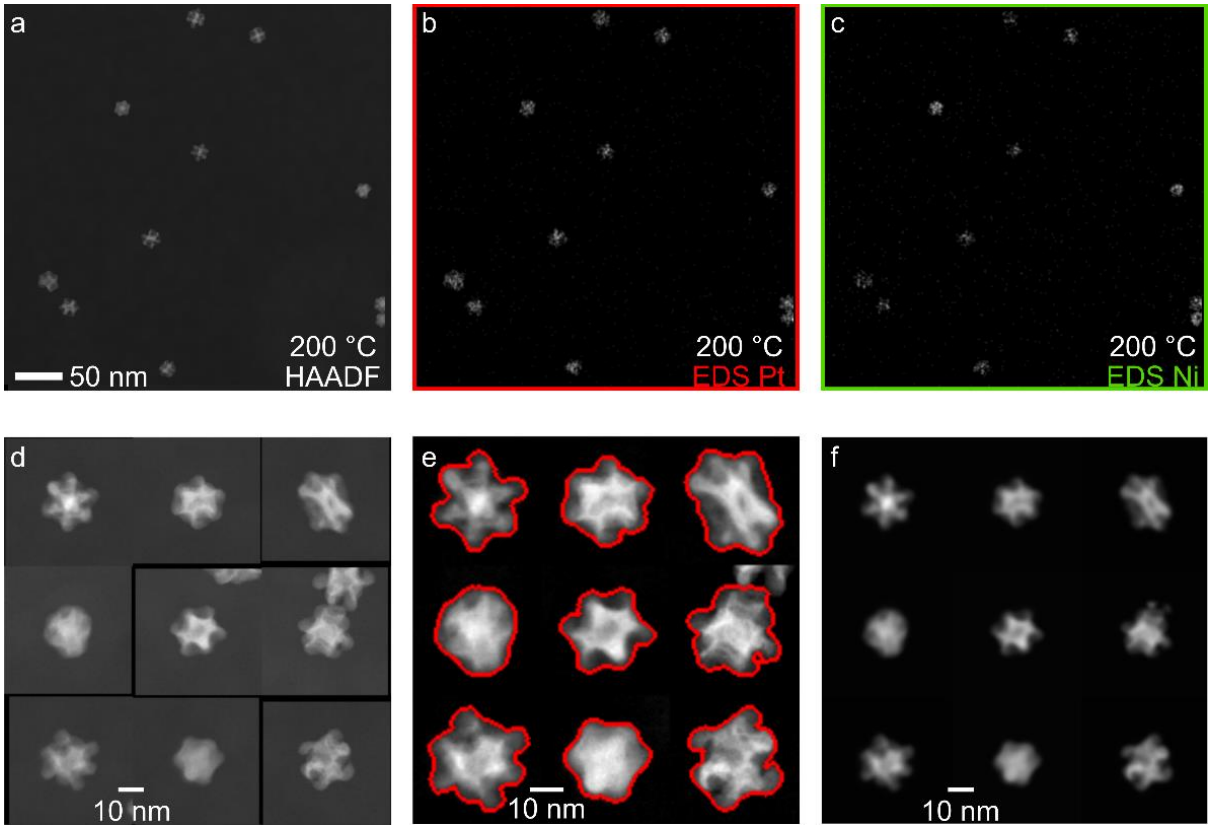

Figure 1. Overview of PtNi nanoparticle population and summary of image processing performed before reconstruction. (a-c) One of the 6 regions characterised in-situ using (a) HAADF, (b) EDS Pt and (c) EDS Ni signals. (d-f) HAADF images showing 9 out of 78 imaged particles demonstrating (d) how particles are cropped from raw HAADF images into boxes, (e) how particles are segmented from the background and are isolated from touching particles where red lines delineate the isolated particle boundary and (f) how the final background is removed, centred, intensity normalised and filtered image ready for orientation matching.

2.4. Orientation matching and 3D reconstruction

The general procedure for spectroscopic SPR reconstruction involves: 1) generating reference re-projections with known orientations; 2) matching experimental 2D HAADF images with reference re-projections; 3) performing 3D reconstruction using established reconstruction algorithms and special parameters; and 4) visualisation. In the present work, we performed two reconstructions using different reference re-projection data sets.

2.4.1. Full re-projection reference data set (code Full-Reproj)

Here the images are matched with re-projections generated from all possible orientations so minimal symmetry is imposed. This method used the same 3D reference data and procedures used in our previous work[26]. The 3D reference data is a HAADF TS-ET tomogram of one PtNi nanoparticle collected from ±70° with incremental steps of 2° between ±50° and 1° for the rest of the tilt range, using 0.07 nm pixel size, 10 µs pixel dwell time, a Fischione 2020 single tilt tomography holder and FEI Inspect3D software. A simultaneous iterative reconstruction technique (SIRT) algorithm in the Astra toolbox[31] with 200 iterations was used for the 3D reconstruction of the reference tomogram. The tomogram was then filtered by a 3D Gaussian filter with 2-pixel kernel size and aligned to its 2-fold rotational (C2) symmetry axis, i.e. <110> direction. A total of 400 re-projections were generated from this 3D tomogram using C2 symmetry and including mirror portions using the EMAN2 projection generator coded[32,33] in python. The orientation of the reference re-projection was described by its azimuth and altitude angles.

The matching between experiment data and re-projections were performed in a “brute force” way. Using a 2D cross correlation implemented using the scikit-image python package[34], every processed HAADF particle image was matched with all 400 references images and their rotated forms. Re-projections were rotated from 0°–360° with 3° increments. Therefore, matching 1 experimental particle with all possible references is equal to 400×360/3=48000 calculations. Then, these 48000 matching results were sorted according to the cross-correlation coefficient (CCC) value from high to

low, with only the match with highest CCC value being retained. Visual inspections were conducted to discard any incorrect matches.

To perform 3D reconstruction, the experimental images were first rotated using the in-plane rotation angle of the matched reference but in a reverse direction. Then the matched azimuth and altitude angle were used as input values for a filtered Fourier space back-projection reconstruction algorithm implemented in EMAN2[28], with an enforced C2 symmetry.

To visualise data, the HAADF 3D reconstruction was thresholded and binarised using a "Huang" thresholding algorithm. The associated EDS reconstructions were masked by this binarised HAADF 3D mask and filtered with a 3D 2-pixel size Gaussian filter to reduce noise.

2.4.2. High symmetry re-projection reference data set (code 4-Reproj)

Here the images were matched with re-projections generated from only 4 orientations. The reference 3D data used in this method was the HAADF SPR reconstructed in previous work[26] but using only the reference re-projections acquired along <110>, <111>, <113> and <100> crystallographic directions. The associated azimuth and altitude angles for the four orientations are [45°, 90°], [45°, 54.74°], [45°, 25.24°] and [45°, 0°], respectively. The angles were chosen based on a rhombic dodecahedron structure.

The matching procedures were the same as the first method (section 2.4.1) except the cross-correlation matching for each experimental particle only requires 4×360/3=480 calculations. The 3D reconstruction procedures were also similar to the first method, except the enforced symmetry was octahedral, which is the highest symmetry of a rhombic dodecahedron. The visualisation steps were the same as the first method.

3. Results and discussion

3.1. Considering the microscope acquisition parameters.

As the SPR method requires imaging many regions under the same imaging conditions and an in-situ study is usually time consuming and expensive, microscope acquisition parameters should be considered based on practical limitations. There are three limitations: the specimen total beam fluence tolerance, the available acquisition time and the reconstruction quality desired.

The total beam fluence can be calculated using the equation shown below.

$$Total\ beam\ fluence = \frac{beam\ current \times dwell\ time}{elementary\ charge \times pixel\ size^2} \times temperature\ steps$$

The same PtNi nanoparticles were examined in previous work and were shown to damage at around 5×10^7 electrons/Å^2. Using this value as an upper limit, all electron fluence imparted to the specimen during in-situ heating experiments should below this limit. The estimated total beam fluence used for each region during all 7 temperature steps is about 4×10^5 electrons/Å^2, which is much lower than the upper limit and ensures the specimen is not affected by the electron beam.

A pixel size of 0.386 nm was fixed to be similar to previous ex-situ spectroscopic SPR work (0.28 nm)[26] so the quality of both intensity reconstructions is comparable. The other variable parameters are pixel dwell time, temperature step and beam current. The electron fluence ideally should be close to the beam tolerance limit to ensure HAADF images and EDS maps have high signal to noise ratio (SNR).

The total acquisition time required for an in situ SPR data set can be calculated using the equation shown below.

$$Total\ acquisition\ time = dwell\ time \times frame\ size^2 \times 1.2 \times number\ of\ regions \times temperature\ steps$$

The factor 1.2 is an experimental factor tested on the ThermoFisher Titan microscope and is considered as the flyback correction to move the beam from the last scanned pixel on previous line to the first pixel of the next line.

Using the equation above and current parameters, the calculated total acquisition time is estimated as 12 hours, which excludes the time for microscope alignments, manually moving between regions and switching temperatures. Increasing dwell time can obtain better SNR images and spectrum data, but even a 50% increase would lead to a 6 hour increase in acquisition time. Reducing the number of temperature steps could reduce acquisition time but may miss nanoparticle transformation details.

Frame size and number of regions do not directly affect the total beam fluence imparted on the specimen but determine the number of particles imaged and therefore affect reconstruction quality. These two parameters are also affected by the dispersion of nanoparticles. The heating chip was prepared by drop casting nanoparticle solutions then drop casting methanol to prevent nanoparticle agglomeration. Increasing the amount of nanoparticle solution and decreasing the amount of methanol could result in particles being packed closely, such that a smaller frame size and fewer image regions are required for the same number of particles. However, precise control of drop casting solution is difficult. If too much nanoparticle solution is deposited onto the chip, they are agglomerated and cannot be isolated and reconstructed. In order to perform a successful experiment, nanoparticles should be well dispersed, although this may require longer acquisition times to find enough particles.

3.2. Analysis of individual particles before 3D reconstruction

By considering individual nanoparticle the change in their 2D projected area and composition as a function of heating temperature can be analysed to demonstrate any possible variations within the specimen population. A HAADF image of an example particle (Figure 2a) demonstrates the melting process of the PtNi rhombic dodecahedron nanoparticle shape starting from losing facets and forming round vertices to the final uniform spherical structure without obvious facets or vertices. From 400°C to 550°C, both HAADF intensity and structure do not show significant variation. The area percentage loss analysis for all extracted nanoparticles (Figure d) also shows that high area

percentage loss in the temperature range of 250°C to 350°C whilst no significant loss is found from 400°C to 550°C.

However, the corresponding EDS maps (Figure 2 b-c) suggest that there are continuous changes at all temperatures. These local variations may be due to the low SNR of EDS maps, as only about 150 EDS counts were detected in each particle. The composition analysis for all individual particles (Figure 2 e) using a k-factor method[35] shows that the composition change between each temperature is small.

The large standard deviations shown in the area loss analysis (Figure 2 d) and composition change analysis (Figure 2 e) imply nanoparticles do not change in an identical way during heating, which will reduce the achievable SPR reconstruction quality if using all these nanoparticles as input to reconstruct the averaged 3D structure and elemental distribution.

As most of nanoparticles lost geometric shapes during heating, orientation matching based on their undefined morphology is inaccurate. Therefore, the room temperature morphology of these nanoparticles are used for template matching and assuming that nanoparticles have not undergone substantial change in orientation during the heating process. To validate this assumption, one nanoparticle is imaged at room temperature and 400 °C during varies heating times from 5 seconds to 300 seconds. Atomic resolution HAADF images are shown in Figure 3. The circled area in Figure 3 a illustrates an initial feature where HAADF intensities are lower than the surroundings, probably due to the lack of Pt atoms and/or the excessive etching during nanoparticle synthesis. As heating time increasing, the shape of nanoparticle projection transforms from the concaved hexagon to hexagon (Figure 3 a-c), the remained general shape indicates the nanoparticle do not tilt dramatically at the beginning of the heating. Then the nanoparticle starts to lost hexagonal shape (Figure 3 d-i). The circled initial feature, however, is presented in the whole heating process, which suggests the nanoparticle remains its orientation while melting and re-solidification.

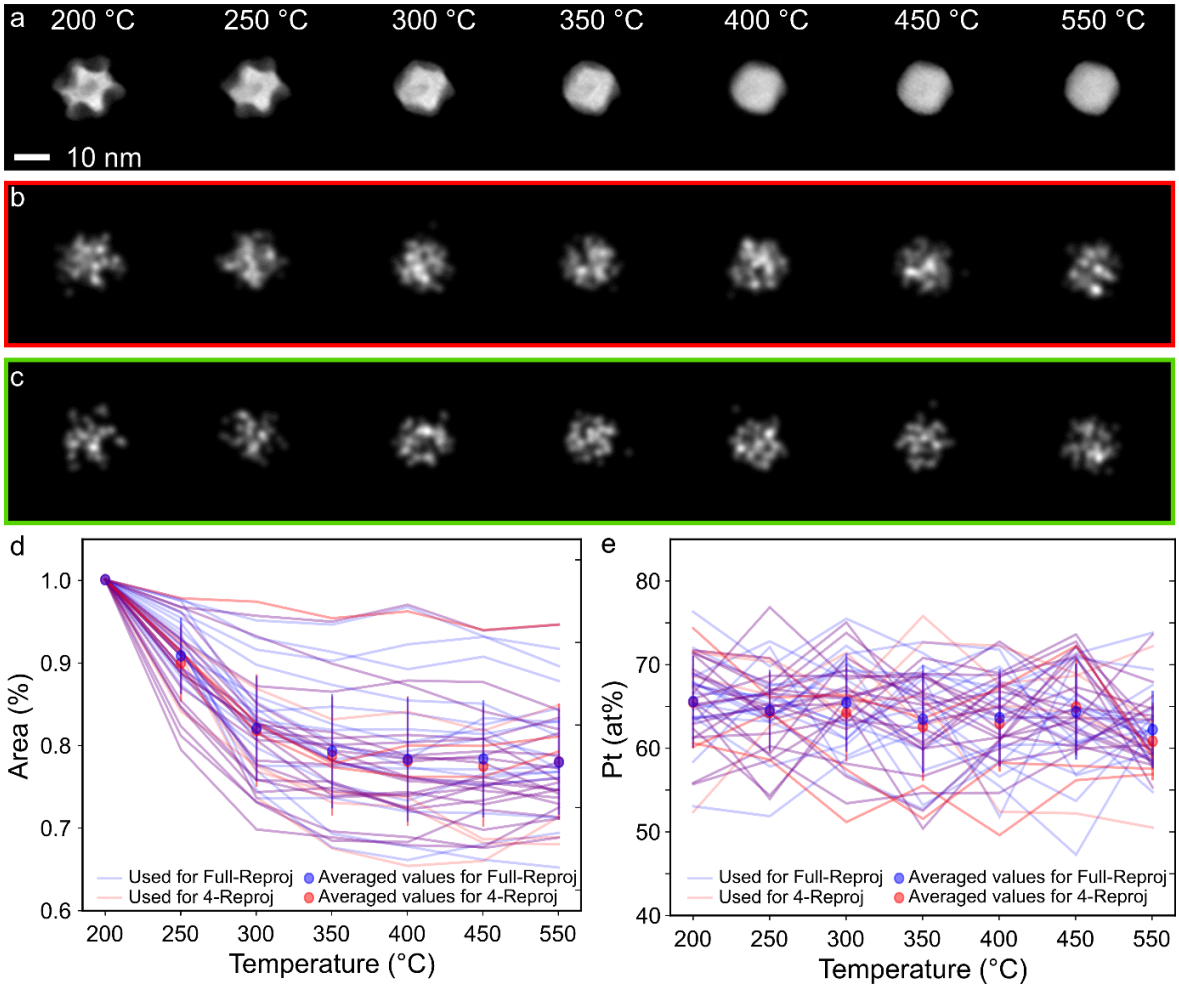

Figure 2. Individual particle analysis of structural and composition change during heating. a-c) Extracted individual particles imaged at each temperature by a) HAADF, b) EDS Pt and c) EDS Ni. d) Percentage of particle area change and e) composition change during heating. In d,e), each line represents one extracted particle from survey images, blue lines represent particles used for 3D reconstruction method Full-Reproj and red lines means particles used for 3D reconstruction method 4-Reproj. Blue and red dots are averaged values for different reference data sets at each temperature step, error bars are standard deviation.

The associated FFT patterns of these atomic resolution HAADF images are shown in Figure 4. Before heating, six most prominent reflection spots are indexed (Figure 4 a, red circled) as the reference of the nanoparticle orientation. The six spots remain distinguishable until heated over 25 seconds (Figure 4 a-f) while four new spots are appearing from 15 seconds heating (Figure 4 d-f). The mixture

of the remaining six spots and new four spots in the FFTs suggests a part of room temperature crystal structure remains while another parts are transformed to new structure. This partial crystal structure transformation is also illustrated in Figure 3 f, where the atom arrangement on the top part of nanoparticle is the same as the room temperature structure (Figure 3 f, red framed and enlarged on the inset) but the atom arrangement on the bottom has changed. The bottom part of the nanoparticle seems to be transformed to ordered PtNi (Figure 3 d-h). In addition, intensities of two of the initial six spots decrease when heated over 25 seconds (Figure 4 f, white arrows), which suggests the overall nanoparticle is slightly rotated. When the nanoparticle is heated over 60 seconds (Figure 4 g), multiple spots are appearing on the neighbour of the initial 6 spots, indicating the original single crystal nanoparticle is becoming polycrystalline. Combing the real space and reciprocal space analysis of atom arrangement at high resolution, it is evidenced that the nanoparticle only undergoes slight tilt but not dramatic rotation during heating. This finding validates the procedure of using room temperature morphology to match orientations and applying the matched orientations on the following heating processing for 3D reconstruction.

3.3. 3D reconstruction

We now discuss two methods of 3D SPR reconstruction based on an SPR framework using a full re-projection reference data set and high-symmetry re-projection data. The full re-projection reference method (Full-Reproj code) matches all 78 isolated particle images to 400 reference images and results in 38 matched particles with 33 matched orientations (Figure 5 b). Then the C2 symmetry was imposed to perform a reconstruction. This is the same method used in previous ex-situ room temperature work[26]. In preliminary in-situ heating tests we found heating nanoparticles to 200°C did not result in visible morphological change. Therefore the comparison between orthoslices of 3D intensity distributions reconstructed at 200°C in the current study (Figure 5 f-h first columns) and that of the reconstructed ex situ data at 25°C (Figure 5 c-e) allows us to assess the reconstruction quality. In both HAADF intensity reconstructions (Figure 5 c and first column in f), the general shape

of the orthoslices remains roughly similar, as well as presence of the higher intensity core. However, six corners in orthoslice 1 and four corners in orthoslice 2 are severely blurred in the 200°C reconstruction, as well as the general appearance of the particle. These blurring artefacts are likely to be the result of there being fewer matched orientations used for reconstruction. EDS intensity reconstructions of Pt and Ni (first columns in Figure 5 g and h, respectively) are even less similar to the room temperature reconstruction, except the Pt rich core and Ni lean core. The significant lower quality of the reconstruction obtained using EDS signals compared to HAADF signals illustrates the necessity of high SNR 2D projections for a good quality reconstruction. To improve EDS map SNR, higher beam current or more particles could be used in future experiments.

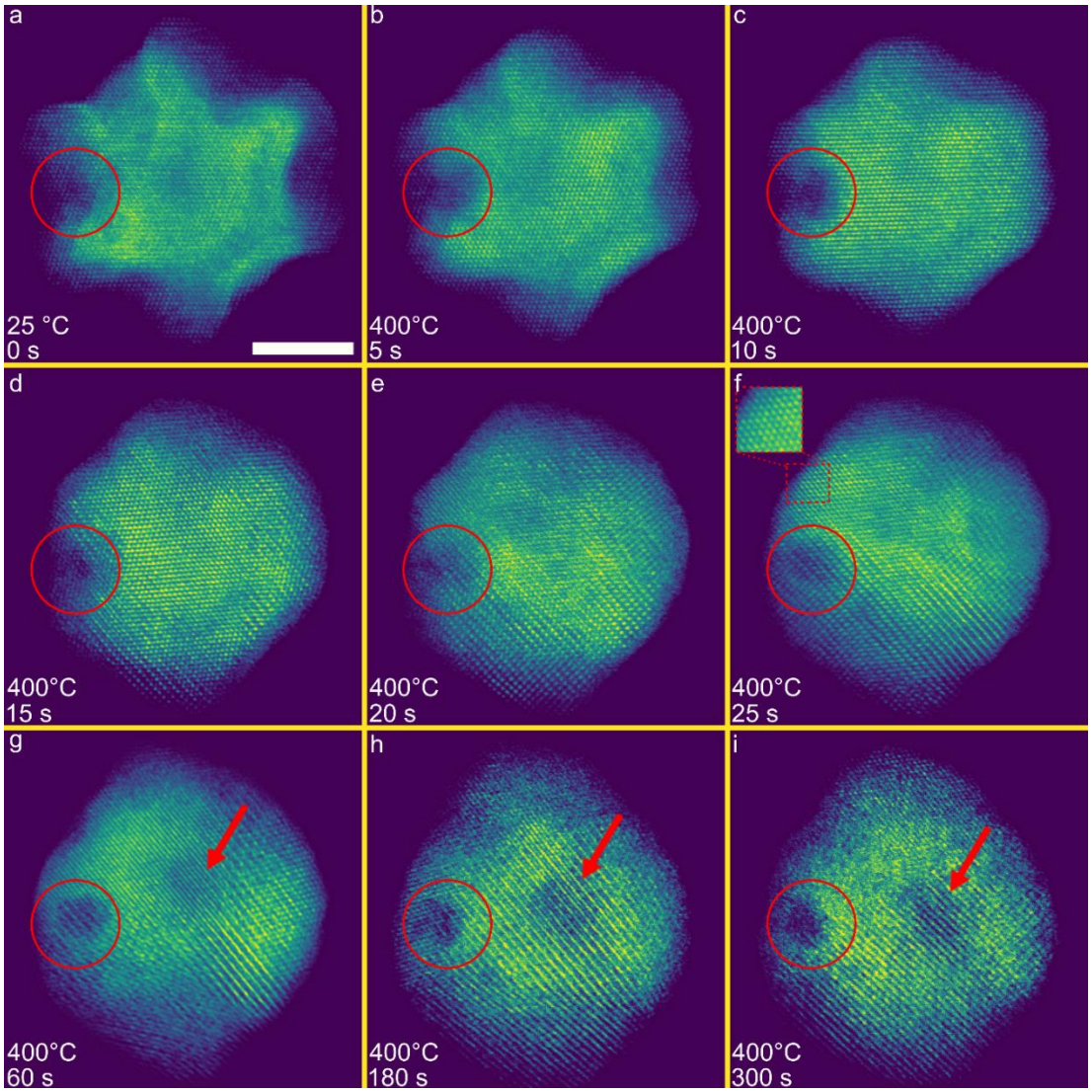

Figure 3. Atomic resolution STEM-HAADF images of a PtNi nanoparticle heated (a) at room temperature and (b-i) at 400 °C in 5, 10, 15, 20, 25, 60, 180 and 300 seconds, respectively. Circles indicating the initial feature on the nanoparticle remains in the whole heating timescale. Inset in (f) shows the framed region imaged at the same time but with different defocus. Arrows indicate the damaged region caused by the parked beam after acquisition. Scale bar 5 nm.

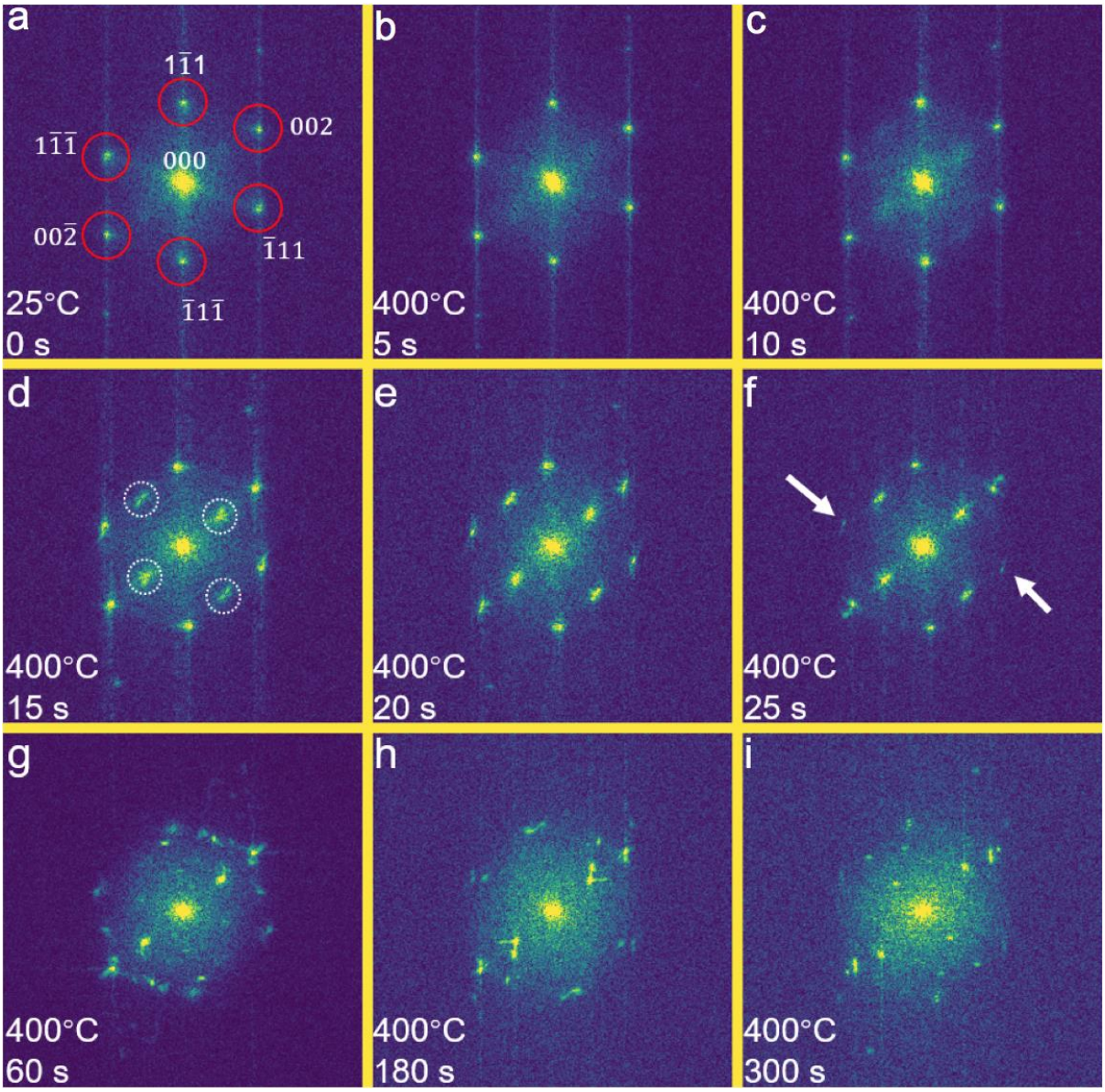

Figure 4. Associated FFTs of the atomic resolution STEM-HAADF images of a PtNi nanoparticle shown in Figure 3. Red circles indicate the position of initial indexed reflections. White circles indicate the

position of the emerging new reflection spots when heated over 15 seconds at 400 °C. White arrows indicate the vanishing of initial reflection spots.

A practical guide suggested by Tang et al. is that the number of orientations for SPR reconstruction should be roughly at least 2.5 times of the target reconstruction box size divided by the symmetry[28]. By considering that half of the orientations projected on a sphere are the mirror of the half's orientations, the required orientations can be further divided by a factor of 2. As the box size we used is 100 pixels wide and mirror portions were not excluded, the minimum required orientations using C2 symmetry should be 100×2.5/2=125, which is much higher than the 33 orientations used here. This calculation not only demonstrates that insufficient orientations cannot result in a good reconstruction, but also indicates that if using high symmetry such as octahedral symmetry and explicitly using all mirror portions the required orientations can be reduced to roughly 100×2.5/24/2=5.

In principle, for the Full-Reproj method, higher symmetries can be applied during reconstruction without using new references and re-doing the matching. However, as we previously tested[26], the orientation assigned by template matching to full 400 re-projections has a standard deviation of 8°. If a high symmetry was imposed during reconstruction, such error may accumulates and results worse reconstruction.

The high symmetry re-projection method (4-Reproj code) attempts to match all 78 isolated particle images to 4 high symmetry reference images (Figure 6 b) and results in 31 successfully matched particles (Figure 6 a). Then octahedral symmetry was imposed to perform the reconstruction. The matched mean projections (Figure 6 c,e,g) prior to the reconstruction are shown to be in good agreement to references (Figure 6 b,d,f). For the HAADF signals, because high SNR and high symmetry are imposed during reconstruction, the reconstruction quality is improved compared to the result of the full re-projection method. The 200°C reconstruction is visually closer to the ex-situ result, not only in the general shape and presence of the high intensity core, but also with respect to

the high intensity corners and low intensity edges; the orthoslices from the 200°C reconstruction (the first column in Figure 7 d) appear similar to those in the high quality ex-situ 25°C reconstruction (Figure 7 a). Based on a comparison between data at 200°C and 25°C, the high symmetry re-projection (4-Reproj code) HAADF reconstruction can be considered as a true reconstruction and the subsequent reconstructions at each temperature step (Figure 7 d) can be used to interpret the PtNi nanoparticle's structural transformation during heating.

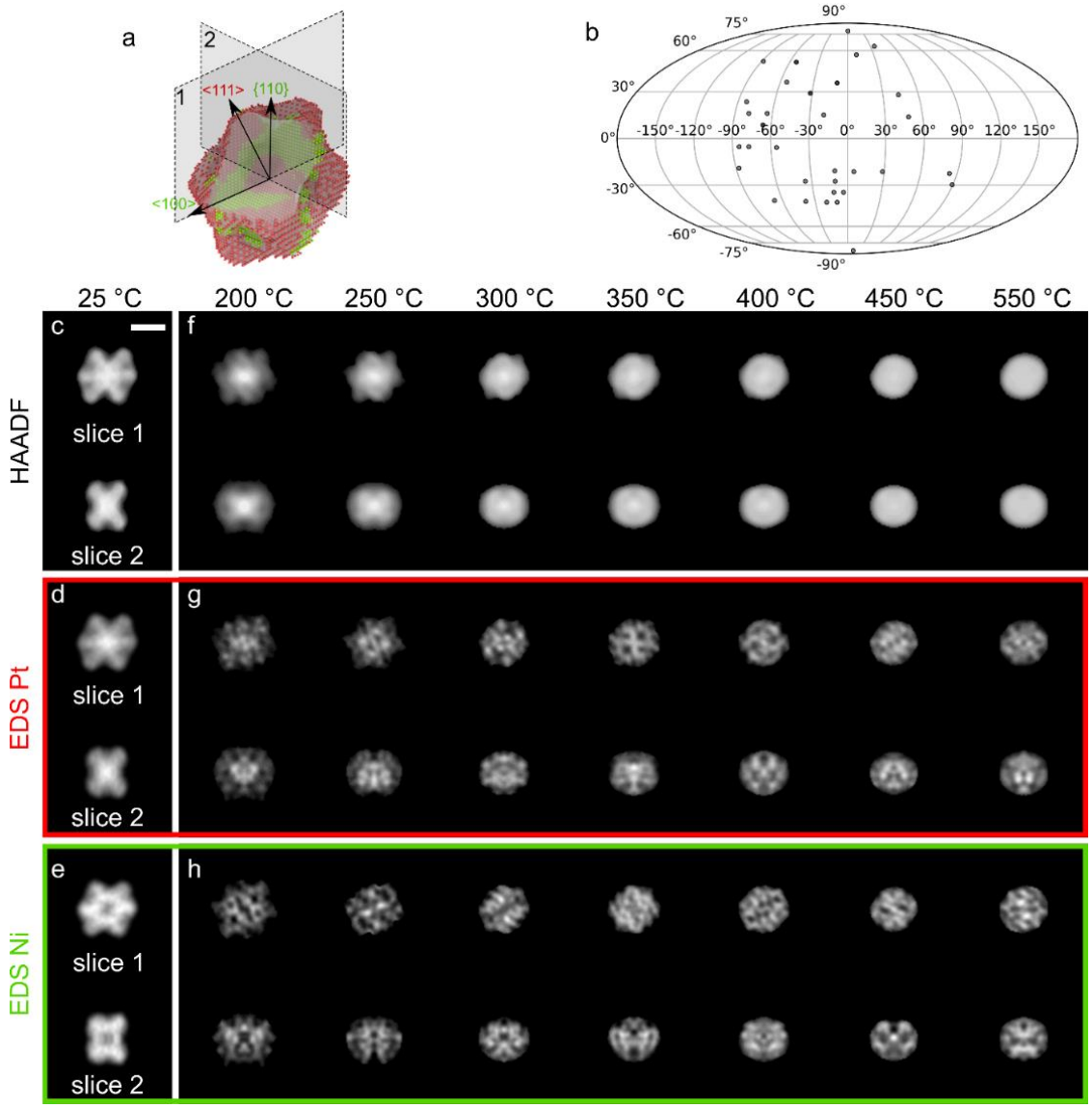

Figure 5. Orthoslices of 3D reconstruction intensity at each temperature. a) 3D model of the same PtNi nanoparticle reconstructed at 25°C. b) Distribution of matched orientations used for

reconstruction Full-Reproj. c-e) Orthoslices extracted from previous reconstructions at 25°C. f-h) Orthoslices extracted from Full-Reproj reconstructions at various temperatures using 33 orientations and C2 symmetry. In each sub-figure, top and bottom rows are slices from position 1 and position 2 illustrated in a). Scale bar 10 nm.

From 200°C to 250°C (Figure 7 d), the low intensity edges in the HAADF orthoslices increase in intensity while high intensity corners lose intensity, resulting in a more uniform rhombic dodecahedron structure without concave facets. At 300°C and 350°C, the HAADF orthoslices show that the highest intensity core remains (Figure 7 d), but the middle shell seems to show lower intensity compared to the outmost shell. Because orthoslices are only 0.39 nm thick and the particles are fully dense, the mass-thickness contrast of the HAADF signal can be considered to be only relevant to mass difference, so higher intensity could imply a higher concentration of Pt atoms compared to lower atomic number Ni. From 400°C to 450°C, the intensity of the core decreases, which may suggest that Pt atoms in the high concentration core start to migrate to the intermediate shell. Finally at 550°C, the HAADF orthoslices illustrate a round structure and uniform intensity, which indicates that not only the facets of the concave rhombic dodecahedron structure found at room temperature become a round sphere structure at 550°C, but that elements are also redistributed and lead a completely uniformly alloyed PtNi nanoparticle.

When examining the EDS Pt and Ni intensity orthoslices, the similarity between the 200°C reconstruction and 25°C reconstruction is much poorer. For the EDS Pt signal, the general shape and high intensity core remains similar in both reconstructions but intensities on the corners marked with arrows (first column in Figure 7 e) are less similar to the slices from 25°C reconstruction (Figure 7 b). This implies that as expected the low SNR EDS Pt maps result in a worse reconstruction quality than the high SNR HAADF signals. For EDS Ni signals, as the ionisation cross section of Ni Kα is smaller than Pt Lα and Ni elements present with lower concentration in this specimen, there is less chance of detecting Ni X-rays and the SNR for EDS Ni is lower than EDS Pt. The poorer SNR could be

the reason that even the general shape of the EDS Ni orthoslices from 200°C reconstructions (the first column in Figure 7 f) do not resemble the slices from 25°C reconstructions (Figure 7 c).

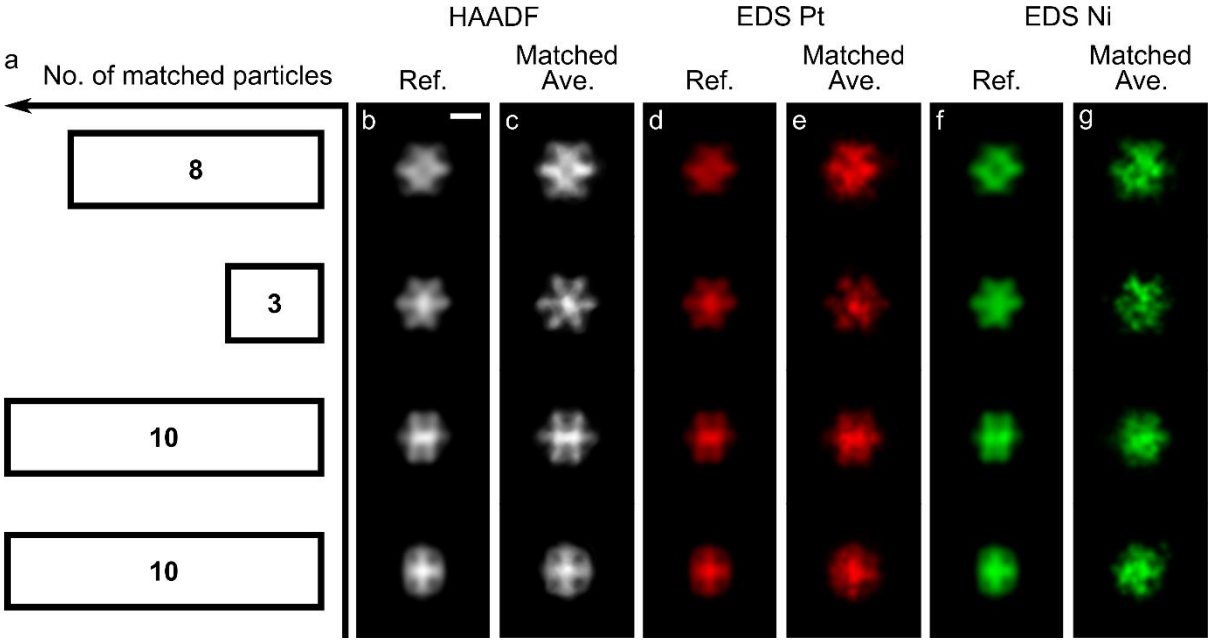

Figure 6. Overview of particles used for reconstruction. a) Histogram of matched particles for 4 reference orientations that correspond to images in b,d,f). All matched particles are averaged and the averages are displayed in c,e,g). Scale bar 10 nm.

4. Conclusion

In this work, we extend the spectroscopic single particle reconstruction method from ex-situ room temperature conditions to dynamic in-situ analysis of temperature induced structural changes and demonstrate study of the thermal stability of PtNi rhombic dodecahedron nanoparticles. The current work demonstrates that it is possible to reconstruct the averaged nanoparticle 3D structure at each temperature step using HAADF signals. However, due to low SNR of EDS maps and fewer imaged nanoparticles, EDS reconstructions do not show reliable results. Increasing beam current while keeping total electron fluence below beam damage thresholds could increase EDS SNR without increasing total acquisition time by controlling parameters such as pixel dwell time and number of imaged regions. If the whole acquisition scheme can be automated, more particles could be imaged

in long sessions. Because the spectroscopic single particle reconstruction scheme does not require tilting holders to high angles, we envision this method can be extended further to other in situ environments without modification of holder or microscope.

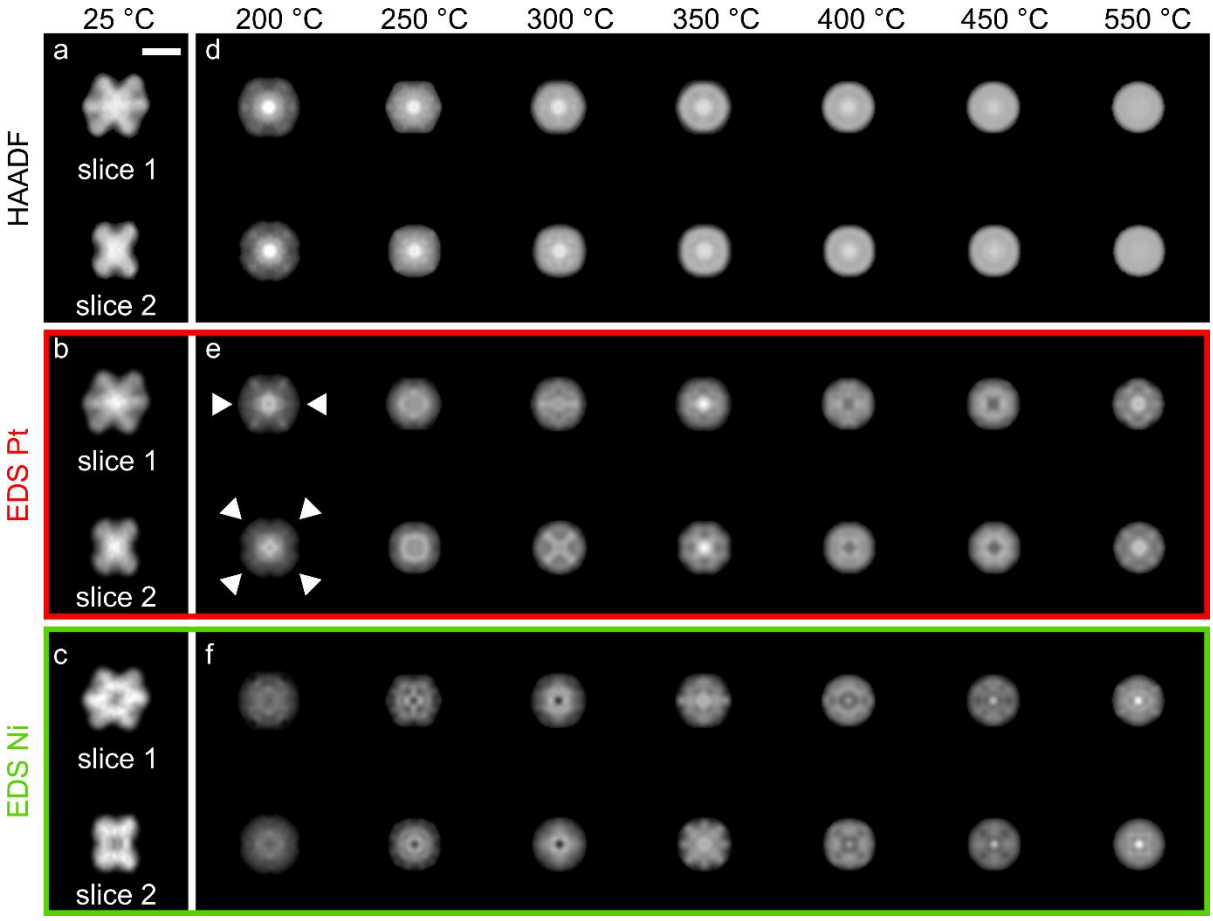

Figure 7. Orthoslices of 3D reconstruction intensity at each temperature. a-c) Orthoslices extracted from previous ex-situ reconstructions at 25°C. d-f) Orthoslices extracted from 4-Reproj reconstructions at various temperatures using 4 orientations and octahedral symmetry. In each sub-figure, top and bottom rows are slices from position 1 and position 2 illustrated in Figure 5 a. Scale bar 10 nm.

References

1. Asset, T. *et al.* A Review on Recent Developments and Prospects for the Oxygen Reduction

Reaction on Hollow Pt-alloy Nanoparticles. *ChemPhysChem* **19**, 1552–1567 (2018).

2. Chaudhari, N. K. *et al.* Recent advances in electrocatalysts toward the oxygen reduction reaction: The case of PtNi octahedra. *Nanoscale* **10**, 20073–20088 (2018).

3. Strasser, P., Gliech, M., Kuehl, S. & Moeller, T. Electrochemical processes on solid shaped nanoparticles with defined facets. *Chem. Soc. Rev.* **47**, 715–735 (2018).

4. Allard, L. F. *et al.* Novel MEMS-based gas-cell/heating specimen holder provides advanced imaging capabilities for in situ reaction studies. *Microsc. Microanal.* **18**, 656–666 (2012).

5. Ramachandramoorthy, R., Bernal, R. & Espinosa, H. D. Pushing the envelope of in situ transmission electron microscopy. *ACS Nano* **9**, 4675–4685 (2015).

6. van Omme, J. T., Zakhozheva, M., Spruit, R. G., Sholkina, M. & Pérez Garza, H. H. Advanced microheater for in situ transmission electron microscopy; enabling unexplored analytical studies and extreme spatial stability. *Ultramicroscopy* **192**, 14–20 (2018).

7. Jinschek, J. R. Advances in the environmental transmission electron microscope (ETEM) for nanoscale in situ studies of gas–solid interactions. *Chem. Commun.* **50**, 2696 (2014).

8. Midgley, P. A. & Dunin-Borkowski, R. E. Electron tomography and holography in materials science. *Nat. Mater.* **8**, 271–280 (2009).

9. Miao, J., Ercius, P. & Billinge, S. J. L. Atomic electron tomography: 3D structures without crystals. *Science* **353**, aaf2157–aaf2157 (2016).

10. Zhou, J. *et al.* Observing crystal nucleation in four dimensions using atomic electron tomography. *Nature* **570**, 500–503 (2019).

11. Baaziz, W. *et al.* Thermal behavior of Pd@SiO2 nanostructures in various gas environments: A combined 3D and: In situ TEM approach. *Nanoscale* **10**, 20178–20188 (2018).

12. Roiban, L. *et al.* Fast 'Operando' electron nanotomography. *J. Microsc.* **269**, 117–126 (2018).

13. Koneti, S. *et al.* Fast electron tomography: Applications to beam sensitive samples and in situ TEM or operando environmental TEM studies. *Mater. Charact.* **151**, 480–495 (2019).

14. Epicier, T. *et al.* 2D & 3D in situ study of the calcination of Pd nanocatalysts supported on delta-Alumina in an Environmental Transmission Electron Microscope. *Catal. Today* **334**, 68–78 (2019).

15. Vanrompay, H. *et al.* 3D characterization of heat-induced morphological changes of Au nanostars by fast: In situ electron tomography. *Nanoscale* **10**, 22792–22801 (2018).

16. Albrecht, W. *et al.* Thermal Stability of Gold/Palladium Octopods Studied In Situ in 3D: Understanding Design Rules for Thermally Stable Metal Nanoparticles. *ACS Nano* **13**, 6522–6530 (2019).

17. Ercius, P., Alaidi, O., Rames, M. J. & Ren, G. Electron Tomography: A Three-Dimensional Analytic Tool for Hard and Soft Materials Research. *Adv. Mater.* **27**, 5638–5663 (2015).

18. Grothausmann, R. *et al.* Quantitative structural assessment of heterogeneous catalysts by electron tomography. *J. Am. Chem. Soc.* **133**, 18161–18171 (2011).

19. Leary, R. *et al.* Quantitative high-angle annular dark-field scanning transmission electron microscope (HAADF-STEM) tomography and high-resolution electron microscopy of unsupported intermetallic GaPd 2 catalysts. *J. Phys. Chem. C* **116**, 13343–13352 (2012).

20. Slater, T. J. A. *et al.* STEM-EDX tomography of bimetallic nanoparticles: A methodological investigation. *Ultramicroscopy* **162**, 61–73 (2016).

21. Jarausch, K., Thomas, P., Leonard, D. N., Twesten, R. & Booth, C. R. Four-dimensional STEM-EELS: Enabling nano-scale chemical tomography. *Ultramicroscopy* **109**, 326–337 (2009).

22. Gontard, L. C., Dunin-Borkowski, R. E., Fernández, A., Ozkaya, D. & Kasama, T. Tomographic Heating Holder for In Situ TEM: Study of Pt/C and PtPd/Al 2 O 3 Catalysts as a Function of

Temperature. *Microsc. Microanal.* **20**, 982–990 (2014).

23. DENS solutions. Available at: https://denssolutions.com/products/wildfire/sample-holder/.

24. Altantzis, T. *et al.* Three-Dimensional Quantification of the Facet Evolution of Pt Nanoparticles in a Variable Gaseous Environment. *Nano Lett.* **19**, 477–481 (2019).

25. De Backer, A., Martinez, G. T., Rosenauer, A. & Van Aert, S. Atom counting in HAADF STEM using a statistical model-based approach: Methodology, possibilities, and inherent limitations. *Ultramicroscopy* **134**, 23–33 (2013).

26. Wang, Y. *et al.* Imaging Three-Dimensional Elemental Inhomogeneity in Pt–Ni Nanoparticles Using Spectroscopic Single Particle Reconstruction. *Nano Lett.* **19**, 732–738 (2019).

27. Cheng, Y., Grigorieff, N., Penczek, P. A. & Walz, T. A Primer to Single-Particle Cryo-Electron Microscopy. *Cell* **161**, 438–449 (2015).

28. Schindelin, J. *et al.* Fiji: An open-source platform for biological-image analysis. *Nat. Methods* **9**, 676–682 (2012).

29. Huang, L.-K. & Wang, M.-J. J. Image thresholding by minimizing the measure of fuzziness. *Pattern Recognit.* 41–51 (1995).

30. Peña, F. de la *et al.* HyperSpy: v1.4.2. (2019). doi:10.5281/zenodo.3249885

31. van Aarle, W. *et al.* The ASTRA Toolbox: A platform for advanced algorithm development in electron tomography. *Ultramicroscopy* **157**, 35–47 (2015).

32. Tang, G. *et al.* EMAN2: An extensible image processing suite for electron microscopy. *J. Struct. Biol.* **157**, 38–46 (2007).

33. Baldwin, P. R. & Penczek, P. A. The Transform Class in SPARX and EMAN2. *J. Struct. Biol.* **157**, 250–261 (2007).

34. scikit-image. (2019). Available at: https://scikit-image.org/.

35. Cliff, G. & Lorimer, G. W. The quantitative analysis of thin specimens. *J. Microsc.* **107**, 203–207 (1975).

7. Conclusion and future works

7.1. Thesis summary

The aim of this doctorate thesis has been to characterise the 3D structure and compositional distribution of beam sensitive nanoparticles using SRP. This aim has definitely been achieved, as evidenced by chapters 5 and 6.

The first paper "Imaging Three-Dimensional Elemental Inhomogeneity in Pt–Ni Nanoparticles Using Spectroscopic Single Particle Reconstruction" established the methodology of using SPR approach with HAADF and EDS signals to quantify 3D elemental segregation. In this study, the advantages of SPR over TS-ET for 3D imaging has been clearly demonstrated. Firstly, SPR results significant beam fluence reduction during acquisition, opens opportunity to imaging this beam sensitive nanoparticle. Secondly, through averaging many EDS spectrum images, the counts per voxel are enhanced and allows 3D EDS quantification after reconstruction, which enables the detection of local composition inhomogeneity.

The second paper "Towards in-situ 3D imaging of nanoparticles using single particle reconstruction" explores further the advantage of SPR over TS-ET which is no requirement for a specialised high tilt holder. In this paper, the in situ heating was performed in a heat-and-quench manner to allow enough time to acquire EDS signals at each temperature step. HAADF signal is used mainly to interpret the 3D structure and compositional change during heating because the SNR of the chemical 3D reconstruction using EDS data is too low to provide reliable reconstruction.

Both techniques in the thesis provide a new level of details on the characterisation of nanomaterials that cannot be reached by other conventional techniques. The outlook on the improvement and application of the technique is discussed further in the next section.

7.2. Future works

7.2.1. Ex situ spectroscopic single particle reconstruction

The spectroscopic single particle reconstruction of nanoparticles performed on ex situ conditions was demonstrated in the chapter 5 which established a workflow combining the use of HAADF and EDS signals to construct the averaged 3D elemental distribution of nanoparticles (Chapter 5, Figure 2). This workflow utilises an initial 3D tomogram template reconstructed by the tilt series HAADF tomography of a single PtNi nanoparticle to generate reference 2D projections with known orientations. Although the final SPR reconstruction quality using this initial high quality TS-ET template was verified to be able to achieve about 1nm resolution. Here the discussion of the effect of the initial template quality to the final spectroscopic single particle reconstruction quality are extended.

If the initial model is considered to represent the general shape of the target nanoparticle, the resolution of the initial model may affect the final reconstruction quality. In general, the initial model resolution should not be worse than the minimal resolvable feature on the target nanoparticle. In the case reported in the chapter 5, the minimal resolvable feature is 2 nm elemental segregation region on PtNi nanoparticle vertices and facets whereas the initial model resolution is better than 1 nm. Low resolution initial model may result in an inaccurate final reconstruction if the algorithm converges to a local minimum and not to the global minimum that represents a true reconstruction. However, initial model with highest resolution may not lead to a high quality final reconstruction. During the orientation matching procedure, high resolution projections generated from the initial model may contain too many details that cannot be matched to low quality experimental data, which results inaccurate orientation assignments and thus reduces final reconstruction quality.

The previous discussion of the initial 3D template quality only focuses on the resolution. The template bias is potentially more detrimental and could lead to a completely wrong reconstruction. Therefore, when choose only one particle as initial template, it is essential for the operator to screen 2D projections of nanoparticles in the microscope session to ensure the picked nanoparticle

resembles the vast majority of nanoparticle population. In some cases, tilt specimen at ±30° to ensure the picked nanoparticle at different orientations all resemble the whole population is required. This pre-screening procedure usually do not require extensive extra operation and is incorporated in the workflow used in the chapter 5.

To alleviate the initial model bias, or the operator's bias, the initial 3D reconstruction could be performed on multiple nanoparticles and using the mean 3D model as the initial template. In practice, the previous high quality one particle TS-ET can be performed for many individual nanoparticles using the same acquisition and reconstruction procedures, with the requirements of more processing time. Otherwise, multiple TS-ET can be obtained with the sacrifice of reconstruction resolution to reduce the operation time, as the initial 3D template resolution is not detrimental to the final reconstruction quality as discussed above. Furthermore, a method named subtomogram averaging can be used to obtain the initial model [127]. This method is essentially same to the TS-ET but includes many particles in the field of view at each tilt [127]. Then the whole field of view is reconstructed, individual nanoparticles are segmented, aligned and averaged. In the above three methods, each method takes less acquisition time than the previous method, and the resolution of the reconstructed individual nanoparticles by each method is worse than the previous method. The decreased acquisition time is beneficial to the applicability of the method but the decreased resolution results difficulties for the following nanoparticle alignments and averaging [165], which may change the accuracy of the averaged initial model and introduce additional alignment bias/error.

To fully eliminate the initial model bias, random orientations of 2D experimental images can be used to reconstruct the initial tomogram and optimising orientations at each iteration until the similarity between 2D experimental images and the 2D re-projections reaches maximum. This method is often used in the final resolution refinement steps in the cryo-EM community to achieve atomic resolutions [151].

As discussed above, the orientation matching procedure is one of the most important step for the spectroscopic SPR reconstruction. The previous methods used in the chapter 5 is cross correlating experiment images to references. Each experiment image is compared to all references and cross correlation quality is sorted by the cross correlation coefficient value. Only the orientation from the reference with the highest cross correlation coefficient value is assigned to the experimental image and other references with low cross correlation coefficient candidates are discarded. This single orientation assignment procedure ensures that only one set of orientations is used for the reconstruction and the reconstruction improvement can be focused on the reconstruction algorithm and image processing. Because the final target in the chapter 5 is to reconstruct the EDS signals, the low SNR is the main resolution limiting factor. In addition, the elemental segregation feature is about 2 nm and the 3D HAADF SPR reconstruction using this method already achieved 1 nm. So it is acceptable to neglect the effect of the orientation assignment error to the final reconstruction. However, if the target resolving feature is smaller, final resolution can be improved by weighting multiple orientations and assigning them to each experimental image. Then the weighting factors can be changed gradually during each reconstruction iteration to improve the orientation assignment accuracy.

In addition, as the PtNi nanoparticles preserve high crystallinity, it is possible to utilise diffraction technique to obtain the crystallographic orientation of each nanoparticle to increase the fidelity of particle orientation matching. Basically, scanning diffraction continuously collects diffraction patterns as a small beam scanning over the specimen [166]. Recent advances in detector technologies and computation allow rapidly recording high dynamic range signals, which renews the technique as 4D STEM, i.e. both two dimensional diffraction signals and two dimensional real space signals can be simultaneously obtained by collecting diffraction patterns at every scanned pixel [167]. Once the complete set of diffraction patterns of each nanoparticle is obtained, not only the crystallographic textures from diffraction patterns, but also the nanoparticle morphology from HAADF images can be reconstructed from the complete 4D data set by applying a virtual aperture to mask desired

positions and ranges on the data set. As diffraction patterns are more sensitive to atomic arrangements than atomic species and the PtNi nanoparticles are FCC structure, it is possible to create a FCC structure 3D atomic model that neglects the atomic species and using this model to create diffraction patterns at all orientations. Then these reference diffraction patterns can be matched to experimentally obtained nanoparticle diffraction patterns. As diffraction patterns are a set of sparse spots and only the position not intensity of these spots needs to be interpreted if no precision diffraction techniques enabled [168], the matching should be less computing expensive than using greyscale HAADF images. Furthermore, correlating the particle orientation matched by diffraction patterns and by HAADF images improves the matching fidelity and accuracy. Diffraction based technique is also capable of identifying nanoparticle orientation where nanoparticles lack of geometric specific features but preserve high crystallinity.

The investigated PtNi nanoparticles present complex structure, morphology and composition segregation. Using spectroscopic single particle reconstruction method, it was found that the nanoparticle is rhombic dodecahedron structure with concaved facets, and on the surface present Pt enrichment on <111> vertices and Ni enrichment on {110} facets and <100> vertices. Previous discussion of the elemental segregation behaviour is focused on the kinetic influence of the synthesis route. Further works could be carried on the effect of the shape of the nanoparticle to the elemental segregation and the catalytic performance. In particular, the surface curvature on nanoparticles may play an important role as not all facets with same atom arrangement show same level of elemental segregation. In previous studies, octahedron PtNi nanoparticles with concaved surface enriched by Ni are found to have superior ORR activity over concaved Pt surface and flat Pt surface [169,170], which is attributed to a descriptor “surface distortion” that consists of local microstrain, defects and composition [171]. In order to elucidate the effect of surface curvature to ORR activity for the rhombic dodecahedron PtNi nanoparticle studied in this thesis, further experiments could be designed to synthesis nanoparticles with same composition but vertices are etched at different level and compare their catalytic performance. The level of etching could be controlled by

attaching excessive or insufficient protective ligands during the synthesis and etching process. In addition, whether the nanoparticle morphology is the cause or the result of the elemental segregation is an interesting direction to explore. If morphology induces elemental segregation, controlled etching and changing surface curvature could result more obvious elemental segregation. On the other hand, if elemental segregation leads to such facets concaved rhombic dodecahedron structure, changing nanoparticle composition should affect the final structure. Although the proposed further experiments involve significant work of chemical synthesis, 3D imaging techniques provided in this thesis are still valid and are essential to unambiguously identify and correlate both morphological and local compositional change to the synthesis route and catalytic activity.

7.2.2. In situ spectroscopic single particle reconstruction

The previous study in the chapter 6 utilises room temperature structure to match orientations and to assign orientations to the following heating steps. It is confirmed by high resolution HAADF images that the nanoparticle does not change its orientation substantially during the heating process and thus the orientation matching method is valid. However, the existence of small rotation is possible and difficult to be corrected when nanoparticles lost their morphology during heating. Using diffraction patterns or FFTs of atomic resolution HAADF images could be one solution to directly index the orientation, as mentioned in the previous section. However, this indexing also relies on the prior knowledge of nanoparticle crystal structure. It is found that the nanoparticle may undergo dramatic atomic rearrangement or disordering, which also affects the accuracy of diffraction based orientation finding [172]. In this condition, iterative reconstruction and updating orientation at each iteration may be more useful as no prior knowledge is required [66,67].

The SNR of the EDS data in the chapter 6 is not sufficient to reconstruct reliable 3D tomogram, thus only HAADF intensity is used to interpret the nanoparticle elemental segregation during heating. One direction to increase the reliability of the reconstruction is to increase SNR of EDS data, by tuning the acquisition parameters such as increasing beam current, acquisition time and number of particles imaged. Another direction is to utilise simulation to validate the HAADF intensity results. As

the HAADF intensity interpretation is based on the 0.39 nm central slices through the reconstructed tomogram, it is relative easy to simulate a HAADF image projection of a thin slice rather than a projection of an entire 20 nm 3D nanoparticle. As the slice thickness is close to the Pt and Ni unit cell length (0.39 and 0.36 nm, respectively [173]), slice simulation can be simplified to generate only one atom thick slice and neglect the channelling effect. Procedures of using simulation to validate the HAADF intensity and elemental segregation can be summarised as the following steps: 1) Before simulation, a threshold value should be chosen to binarise the HAADF slice from the reconstruction so any area with intensity below the threshold is considered to be occupied by Ni atoms. 2) Then the position of Pt and Ni atoms on one atom thick slice can be constructed based on binarised images and inputted into simulation program with same experimental parameters to generate the an HAADF image. 3) The intensity of the experimental and simulated HAADF image should be normalised so they are comparable. 4) After normalisation, the similarity of both images should be compared and summarised into one value use methods such as root mean squared difference or cross correlation coefficient. 5) Repeat steps 1-4 for a wide range of threshold values to obtain a list of similarity comparison results. 6) Choose the comparison with the highest similarity value then the corresponding Pt and Ni atom arrangements should be the elemental segregation. This simulation procedure may also be extended to the whole 3D HAADF tomogram by simulating every slice.

7.3. Outlook of the spectroscopic single particle reconstruction technique

In this thesis, the spectroscopic single particle reconstruction method is proposed to characterise 3D structure and elemental distribution of nanoparticle with less beam damage and more representative sampling of nanoparticle population. The spectroscopic SPR method also releases the requirements of a specialised thin in situ holder or large gap pole pieces for 3D in situ characterisation. But the application and development of the spectroscopic SPR based technique is not limited by the thesis. As there are many types of signal available in the modern TEM such as EELS, cathodoluminescence, diffraction, etc. and each of them carrying unique information, utilising EDS

could be combined with or replaced by these signals to explore unique properties of nanoparticles. The spatial resolution of the spectroscopic SPR can also be push to atomic level to distinguish the shared and unique 3D atomic arrangement for a large amount of similar nanoparticles as the current atomic resolution 3D imaging is limited to only one or a few nanoparticles. Furthermore, the temporal resolution can be improved as long as remaining sufficient SNR and particles in the field of view when operating the microscope at continuous heating and imaging conditions. This time resolution can be improved to as fast as frame rate to generate a movie of in situ 3D structure transformation. In addition to all of the abovementioned development, they can be combined together with the new in situ capabilities to provide the ultimate atomic resolution, video-level temporal resolution, three dimensions, real environments, quantitative elemental information and other spectroscopic information enabled characterisation of nanoparticles in the future.

8. References

1. Ruska, E. & Knoll, M. Die magnetische Sammelspule für schnelle Elektronenstrahlen. (The magnetic concentrating coil for fast electron beams.). *Z. techn. Phys.* 389–400 (1931).
2. Ophus, C. Four-Dimensional Scanning Transmission Electron Microscopy (4D-STEM): From Scanning Nanodiffraction to Ptychography and Beyond. *Microsc. Microanal.* **25**, 563–582 (2019).
3. de Jonge, N., Houben, L., Dunin-Borkowski, R. E. & Ross, F. M. Resolution and aberration correction in liquid cell transmission electron microscopy. *Nature Reviews Materials* **4**, 61–78 (2019).
4. Orloff, J. Survey of electron sources for high-resolution microscopy. *Ultramicroscopy* **28**, 88–97 (1989).
5. Ross, I. M. & Walther, T. Configuring a 300kV cold field-emission gun for optimum analytical performance. *J. Phys. Conf. Ser.* **371**, (2012).
6. Williams, D. B. & Carter, C. B. *Transmission Electron Microscopy: A Textbook for Materials Science*. (Springer, 2009).
7. Brydson, R. *Aberration-corrected analytical transmission electron microscopy*. (RMS-Wiley, 2011).
8. Midgley, P. A. & Eggeman, A. S. Precession electron diffraction - A topical review. *IUCrJ* **2**, 126–136 (2015).
9. Nguyen, L. *et al.* Atomic-Scale Insights into the Oxidation of Aluminum. *ACS Appl. Mater. Interfaces* **10**, 2230–2235 (2018).
10. Urban, K., Kabius, B., Haider, M. & Rose, H. A way to higher resolution: Spherical-aberration correction in a 200 kV transmission electron microscope. *J. Electron Microsc. (Tokyo).* **48**, 821–826 (1999).
11. Krivanek, O. L., Dellby, N. & Lupini, A. R. Towards sub-angstrom electron beams.

Ultramicroscopy **78**, 1–11 (1999).

12. Brydson, R. & Hondow, N. Electron Energy Loss Spectrometry and Energy Dispersive X-ray Analysis. in *Aberration-Corrected Analytical Transmission Electron Microscopy* 163–210 (John Wiley & Sons, Ltd, 2011).
13. Reimer, L. & Kohl, H. *Transmission electron microscopy - Physics of image formation*. (Springer, 2008).
14. Krivanek, O. L. *et al.* Atom-by-atom structural and chemical analysis by annular dark-field electron microscopy. *Nature* **464**, 571–574 (2010).
15. Pennycook, S. J. Imaging in STEM. in *Transmission electron microscopy - Diffraction, imaging, and spectrometry* (eds. Carter, C. B. & Williams, D. B.) 283–342 (Springer, 2016).
16. Nellist, P. D. The principles of STEM imaging - Imaging and analysis. in *Scanning transmission electron microscopy* (eds. Pennycook, S. J. & Nellist, P. D.) 91–116 (Springer, 2011).
17. Moseley, H. G. J. The High Frequency Spectra of the Element. *Philos. Mag.* 1024 (1913).
18. Bethe, H. A. Zur Theorie des Durchgangs schneller Korpuskularstrahlen durch Materie. *Ann. Phys.* 325–400 (1930).
19. Auger, M. P. Sur L'Effet Photoelectrique Compose. *J. Phys Radium* 205–208 (1925).
20. Kramers, H. A. *On the theory of X-ray absorption and of the continuous X-ray spectrum*. *Philosophical Magazine* **46**, (1923).
21. Newbury, D. E. The new X-ray mapping: X-ray spectrum imaging above 100 kHz output count rate with the silicon drift detector. *Microsc. Microanal.* **12**, 26–35 (2006).
22. *X-Ray Spectrometry in Electron Beam Instruments*. (Springer, 1995).
23. Kemmer, J., Lutz, G., Belau, E., Prechtel, U. & Welser, W. Low capacity drift diode. *Nucl. Inst. Methods Phys. Res. A* **253**, 378–381 (1987).
24. Aurola, A., Marochkin, V., Golovleva, M. & Tuuva, T. Novel silicon drift detector design enabling low dark noise and simple manufacturing. *J. Instrum.* **10**, C02047–C02047 (2015).
25. Colijn, H. O., Yang, F., Williams, D. B., Sandborg, A. & McComb, D. W. Performance of an

improved TEM SDD detector. *Microsc. Microanal.* **20**, 608–609 (2014).

26. Faschingbauer, U., Schmitt, B., Warner, A. & Wurm, J. P. Large Area Cylindrical Silicon Drift Detector. *IEEE Trans. Nucl. Sci.* **39**, 619–628 (1992).

27. Zaluzec, N. J. XEDS systems for the next generation analytical electron microscope. *Microsc. Microanal.* **10**, 122–123 (2004).

28. Zaluzec, N. J. Innovative Instrumentation for Analysis of Nanoparticles: The π Steradian Detector. *Micros. Today* **17**, 56–59 (2009).

29. Terborg, R., Käppel, A. & Salge, T. Applications using an Annular Four-Channel Silicon Drift Detector. *Microsc. Microanal.* **16**, 1400–1401 (2010).

30. Schlossmacher, P., Klenov, D. O., Freitag, B., Harrach, S. Von & Steinbach, A. Nanoscale Chemical Compositional Analysis with an Innovative S/TEM-EDX System. *Microsc. Anal. Nanotechnol. Suppl.* **24**, S5–S8 (2010).

31. Kawai, S. *et al.* A double silicon drift type detector system for EDS with ultrahigh efficiency and throughput for TEM. *Microsc. Microanal.* **20**, 1150–1151 (2014).

32. Kothleitner, G. *et al.* Quantitative Elemental Mapping at Atomic Resolution Using X-Ray Spectroscopy. *Phys. Rev. Lett.* **112**, 085501 (2014).

33. Cliff, G. & Lorimer, G. W. The quantitative analysis of thin specimens. *J. Microsc.* **107**, 203–207 (1975).

34. Watanabe, M. & Williams, D. B. The quantitative analysis of thin specimens: A review of progress from the Cliff-Lorimer to the new ζ-factor methods. *J. Microsc.* **221**, 89–109 (2006).

35. Gonzalez, R. C. & Woods, R. E. *Digital image processing*. (Pearson, 2007).

36. Newbury, D. E. & Ritchie, N. W. M. Performing elemental microanalysis with high accuracy and high precision by scanning electron microscopy/silicon drift detector energy-dispersive X-ray spectrometry (SEM/SDD-EDS). *J. Mater. Sci.* **50**, 493–518 (2015).

37. Kotula, P. X-ray and EELS Imaging. in *Transmission electron microscopy - Diffraction, imaging, and spectrometry* (eds. Carter, C. B. & Williams, D. B.) 439–466 (Springer, 2016).

38. Kotula, P. G., Keenan, M. R., Grant, R. P. & Hlava, P. F. Multivariate statistical analysis of wavelength and energy-dispersive X-ray spectral images. *Microsc. Microanal.* **10**, 118–119 (2004).

39. Potapov, P., Longo, P. & Okunishi, E. Enhancement of noisy EDX HRSTEM spectrum-images by combination of filtering and PCA. *Micron* **96**, 29–37 (2017).

40. Rossouw, D. *et al.* Multicomponent Signal Unmixing from Nanoheterostructures: Overcoming the Traditional Challenges of Nanoscale X-ray Analysis via Machine Learning. *Nano Lett.* **15**, 2716–2720 (2015).

41. Potapov, P. Why Principal Component Analysis of STEM spectrum-images results in 'abstract', uninterpretable loadings? *Ultramicroscopy* **160**, 197–212 (2016).

42. Wood, J. E., Williams, D. B. & Goldstein, J. I. Experimental and theoretical determination of kAFe factors for quantitative X-ray microanalysis in the analytical electron microscope. *J. Microsc.* **133**, 255–274 (1984).

43. Watanabe, M., Horita, Z. & Nemoto, M. Absorption correction and thickness determination using the zeta factor in quantitative X-ray microanalysis. *Ultramicroscopy* **65**, 187–198 (1996).

44. Rueda-Fonseca, P. *et al.* Quantitative Reconstructions of 3D Chemical Nanostructures in Nanowires. *Nano Lett.* **16**, 1637–1642 (2016).

45. Baumeister, W., Grimm, R. & Walz, J. Electron tomography of molecules and cells. *Trends Cell Biol.* **9**, 81–85 (1999).

46. Hart, R. G. Electron microscopy of unstained biological material: The polytropic montage. *Science* **159**, 1464–1467 (1968).

47. De Rosier, D. J. & Klug, a. Reconstruction of Three Dimensional Structures from Electron Micrographs. *Nature* **217**, 130–134 (1968).

48. Frank, J. Averaging of low exposure electron micrographs of non-periodic objects. *Ultramicroscopy* **1**, 159–162 (1975).

49. Henderson, R. & Unwin, P. N. T. Three-dimensional model of purple membrane obtained by

electron microscopy. *Nature* **257**, 28–32 (1975).

50. Frank, J. Optimum use of image information using signal detection and averaging techniques. *Ann. N. Y. Acad. Sci.* **306**, 112–120 (1978).

51. Radon, J. On determination of functions by their integral values along certain multiplicities. *Ber. der Sachische Akad. der Wissenschaften Leipzig,(Germany)* **69**, 262–77 (1917).

52. Crowther, R. A., DeRosier, D. J. & Klug, A. The Reconstruction of a Three-Dimensional Structure from Projections and its Application to Electron Microscopy. *Proc. R. Soc. London A Math. Phys. Eng. Sci.* **317**, 319–340 (1970).

53. Gilbert, P. Iterative methods for the three-dimensional reconstruction of an object from projections. *J. Theor. Biol.* **36**, 105–117 (1972).

54. Gordon, R., Bender, R. & Herman, G. T. Algebraic reconstruction techniques (ART) for three-dimensional electron microscopy and x-ray photography. *J. Theor. Biol.* **29**, 471–481 (1970).

55. Midgley, P. A. & Weyland, M. 3D electron microscopy in the physical sciences: the development of Z-contrast and EFTEM tomography. *Ultramicroscopy* **96**, 413–431 (2003).

56. Slater, T. J. A. *et al.* STEM-EDX tomography of bimetallic nanoparticles: A methodological investigation. *Ultramicroscopy* **162**, 61–73 (2016).

57. Collins, S. M. & Midgley, P. A. Progress and opportunities in EELS and EDS tomography. *Ultramicroscopy* **180**, 133–141 (2017).

58. Van den Broek, W., Van Aert, S. & Van Dyck, D. A model based atomic resolution tomographic algorithm. *Ultramicroscopy* **109**, 1485–1490 (2009).

59. Burdet, P., Saghi, Z., Filippin, A. N., Borrás, A. & Midgley, P. A. A novel 3D absorption correction method for quantitative EDX-STEM tomography. *Ultramicroscopy* **160**, 118–129 (2016).

60. Collins, S. M. *et al.* Eigenmode Tomography of Surface Charge Oscillations of Plasmonic Nanoparticles by Electron Energy Loss Spectroscopy. *ACS Photonics* **2**, 1628–1635 (2015).

61. Batenburg, K. J. *et al.* 3D imaging of nanomaterials by discrete tomography. *Ultramicroscopy*

109, 730–740 (2009).

62. Goris, B., Van den Broek, W., Batenburg, K. J., Heidari Mezerji, H. & Bals, S. Electron tomography based on a total variation minimization reconstruction technique. *Ultramicroscopy* **113**, 120–130 (2012).

63. Leary, R., Saghi, Z., Midgley, P. A. & Holland, D. J. Compressed sensing electron tomography. *Ultramicroscopy* **131**, 70–91 (2013).

64. Saghi, Z. *et al.* Reduced-dose and high-speed acquisition strategies for multi-dimensional electron microscopy. *Adv. Struct. Chem. Imaging* **1**, 1–10 (2015).

65. Zhong, Z., Palenstijn, W. J., Adler, J. & Batenburg, K. J. EDS tomographic reconstruction regularized by total nuclear variation joined with HAADF-STEM tomography. *Ultramicroscopy* **191**, 34–43 (2018).

66. Pryor, A. *et al.* GENFIRE: A generalized Fourier iterative reconstruction algorithm for high-resolution 3D imaging. *Sci. Rep.* **7**, 10409 (2017).

67. Yang, Y. *et al.* Deciphering chemical order/disorder and material properties at the single-atom level. *Nature* **542**, 75 (2017).

68. Zhou, J. *et al.* Observing crystal nucleation in four dimensions using atomic electron tomography. *Nature* **570**, 500–503 (2019).

69. Feng, J., Somlyo, A. P., Somlyo, A. V. & Shao, Z. Automated electron tomography with scanning transmission electron microscopy. *J. Microsc.* **228**, 406–412 (2007).

70. Tian, X. *et al.* Determining the 3D Atomic Coordinates and Crystal Defects in 2D Materials with Picometer Precision. *Microsc. Microanal.* **25**, 404–405 (2019).

71. Vanrompay, H., Béché, A., Verbeeck, J. & Bals, S. Experimental Evaluation of Undersampling Schemes for Electron Tomography of Nanoparticles. *Part. Part. Syst. Charact.* **1900096**, 1900096 (2019).

72. Radermacher, M. Three-dimensional reconstruction of single particles from random and nonrandom tilt series. *J. Electron Microsc. Tech.* **9**, 359–94 (1988).

73. Arslan, I., Tong, J. R. & Midgley, P. a. Reducing the missing wedge: High-resolution dual axis tomography of inorganic materials. *Ultramicroscopy* **106**, 994–1000 (2006).

74. Kato, M. *et al.* Maximum diameter of the rod-shaped specimen for transmission electron microtomography without the "missing wedge". *Ultramicroscopy* **108**, 221–229 (2008).

75. Xu, R. *et al.* Three-dimensional coordinates of individual atoms in materials revealed by electron tomography. *Nat. Mater.* **14**, 1099–1106 (2015).

76. Saxton, W. O., Baumeister, W. & Hahn, M. Three-dimensional reconstruction of imperfect two-dimensional crystals. *Ultramicroscopy* **13**, 57–70 (1984).

77. Miao, J., Förster, F. & Levi, O. Equally sloped tomography with oversampling reconstruction. *Phys. Rev. B* **72**, 052103 (2005).

78. Lee, E. *et al.* Radiation dose reduction and image enhancement in biological imaging through equally-sloped tomography. *J. Struct. Biol.* **164**, 221–227 (2008).

79. Liu, B., Yu, H., Verbridge, S. S., Sun, L. & Wang, G. Dictionary-learning-based reconstruction method for electron tomography. *Scanning* **36**, 377–383 (2013).

80. Weyland, M., Midgley, P. A. & Thomas, J. M. Electron tomography of nanoparticle catalysts on porous supports: A new technique based on Rutherford scattering. *J. Phys. Chem. B* **105**, 7882–7886 (2001).

81. Midgley, P. A. & Dunin-Borkowski, R. E. Electron tomography and holography in materials science. *Nat. Mater.* **8**, 271–280 (2009).

82. Midgley, P. A. *et al.* High-Resolution Scanning Transmission Electron Tomography and Elemental Analysis of Zeptogram Quantities of Heterogeneous Catalyst. *J. Phys. Chem. B* **108**, 4590–4592 (2004).

83. Friedrich, H., Jongh, P. E. De, Verkleij, A. J. & Jong, K. P. De. Electron Tomography for Heterogeneous Catalysts and Related Nanostructured Materials Materials. *Chem. Rev.* **109**, 1613–1629 (2009).

84. Tessonnier, J. P. *et al.* Selective deposition of metal nanoparticles inside or outside

multiwalled carbon nanotubes. *ACS Nano* **3**, 2081–2089 (2009).

85. Yu, Y. *et al.* Three-dimensional tracking and visualization of hundreds of Pt-Co fuel cell nanocatalysts during electrochemical aging. *Nano Lett.* **12**, 4417–4423 (2012).

86. Ward, E. P. W. E. P. W. *et al.* Three-Dimensional Nanoparticle Distribution and Local Curvature of Heterogeneous Catalysts Revealed by Electron Tomography. *J. Phys. Chem. C* **111**, 11501–11505 (2007).

87. Pinho, L., Hernández-Garrido, J. C., Calvino, J. J. & Mosquera, M. J. 2D and 3D characterization of a surfactant-synthesized TiO 2 -SiO 2 mesoporous photocatalyst obtained at ambient temperature. *Phys. Chem. Chem. Phys.* **15**, 2800–2808 (2013).

88. Kovarik, L. *et al.* Tomography and high-resolution electron microscopy study of surfaces and porosity in a plate-like γ-Al2O3. *J. Phys. Chem. C* **117**, 179–186 (2013).

89. Sueda, S., Yoshida, K. & Tanaka, N. Quantification of metallic nanoparticle morphology on TiO2 using HAADF-STEM tomography. *Ultramicroscopy* **110**, 1120–1127 (2010).

90. Tanaka, N., Yoshida, K. & Arai, S. In-situ gas study and 3D quantitation of titania photocatalysts by advanced electron microscopy. *J. Phys. Conf. Ser.* **371**, (2012).

91. Mourdikoudis, S. *et al.* Governing the morphology of Pt-Au heteronanocrystals with improved electrocatalytic performance. *Nanoscale* **7**, 8739–8747 (2015).

92. Percebom, A. M. *et al.* Janus gold nanoparticles obtained via spontaneous binary polymer shell segregation. *Chem. Commun.* **52**, 4278–4281 (2016).

93. Gontard, L. C., Dunin-Borkowski, R. E. & Ozkaya, D. Three-dimensional shapes and spatial distributions of Pt and PtCr catalyst nanoparticles on carbon black. *J Microsc* **232**, 248–259 (2008).

94. Xia, Y. *et al.* 3D Quantification of Low-Coordinate Surface Atom Density: Bridging Catalytic Activity to Concave Facets of Nanocatalysts in Fuel Cells. *Small* **12**, 6332–6337 (2016).

95. Yu, W., Batchelor-mcauley, C., Wang, Y., Shao, S. & Compton, R. G. Characterising porosity in platinum nanoparticle. *Nanoscale* (2019). doi:10.1039/c9nr06071e

96. Leary, R. *et al.* Quantitative high-angle annular dark-field scanning transmission electron microscope (HAADF-STEM) tomography and high-resolution electron microscopy of unsupported intermetallic GaPd 2 catalysts. *J. Phys. Chem. C* **116**, 13343–13352 (2012).

97. Scott, M. C. *et al.* Electron tomography at 2.4-ångström resolution. *Nature* **483**, 444–447 (2012).

98. Goris, B. *et al.* Atomic-scale determination of surface facets in gold nanorods. *Nat. Mater.* **11**, 930–935 (2012).

99. Van Aert, S., Batenburg, K. J., Rossell, M. D., Erni, R. & Van Tendeloo, G. Three-dimensional atomic imaging of crystalline nanoparticles. *Nature* **470**, 374–377 (2011).

100. Möbus, G., Doole, R. C. & Inkson, B. J. Spectroscopic electron tomography. *Ultramicroscopy* **96**, 433–51 (2003).

101. Zhong, Z., Goris, B., Schoenmakers, R., Bals, S. & Batenburg, K. J. 3D structure and chemical composition reconstructed simultaneously from HAADF-STEM images and EDS-STEM maps. in *EMC2016* 1–3 (2016). doi:10.1002/9783527808465.EMC2016.6737

102. Lepinay, K., Lorut, F., Pantel, R. & Epicier, T. Chemical 3D tomography of 28nm high K metal gate transistor: STEM XEDS experimental method and results. *Micron* **47**, 43–49 (2013).

103. Sorel, J. *et al.* Correlative HAADF-STEM and EDX-STEM Tomography for the 3D Morphological and Elemental Analysis of FinFET Semiconductor Devices. *Microsc. Microanal.* **24**, 388–389 (2018).

104. Fu, B. & Gribelyuk, M. A. 3D analysis of semiconductor devices: A combination of 3D imaging and 3D elemental analysis. *J. Appl. Phys.* **123**, (2018).

105. Baumann, F. H., Popielarski, B., Mitchell, T. & Lu, Y. Towards Routine EDX Tomography in Semiconductor Failure Analysis. *Microsc. Microanal.* **25**, 1820–1821 (2019).

106. Genc, A. *et al.* XEDS STEM tomography for 3D chemical characterization of nanoscale particles. *Ultramicroscopy* **131**, 24–32 (2013).

107. Liakakos, N. *et al.* Co-Fe nanodumbbells: Synthesis, structure, and magnetic properties. *Nano*

Lett. **14**, 2747–2754 (2014).

108. Goris, B., Polavarapu, L., Bals, S., Van Tendeloo, G. & Liz-Marzán, L. M. Monitoring galvanic replacement through three-dimensional morphological and chemical mapping. *Nano Lett.* **14**, 3220–3226 (2014).

109. Polavarapu, L. *et al.* Galvanic Replacement Coupled to Seeded Growth as a Route for Shape-Controlled Synthesis of Plasmonic Nanorattles. *J. Am. Chem. Soc.* **138**, 11453–11456 (2016).

110. Slater, T. J. A. *et al.* Correlating catalytic activity of Ag-Au nanoparticles with 3D compositional variations. *Nano Lett.* **14**, 1921–1926 (2014).

111. Han, L. *et al.* Interrogation of bimetallic particle oxidation in three dimensions at the nanoscale. *Nat. Commun.* **7**, 13335 (2016).

112. Xia, W. *et al.* Bimetallic nanoparticle oxidation in three dimensions by chemically sensitive electron tomography and in situ transmission electron microscopy. *ACS Nano* **12**, 7866–7874 (2018).

113. Collins, S. M. *et al.* Phase diagrams of liquid-phase mixing in multi-component metal-organic framework glasses constructed by quantitative elemental nano-tomography. *APL Mater.* **091111**, (2019).

114. Chen, J. Z. *et al.* A dose-rate effect in single-particle electron microscopy. *J. Struct. Biol.* **161**, 92–100 (2008).

115. Grassucci, R. A., Taylor, D. J. & Frank, J. Preparation of macromolecular complexes for cryo-electron microscopy. *Nat. Protoc.* **2**, 3239–3246 (2007).

116. Dubochet, J. & McDowall, A. W. Vitrification of Pure Water for Electron Microscopy. *J. Microsc.* **124**, 3–4 (1981).

117. Elmlund, D. & Elmlund, H. Cryogenic electron microscopy and single-particle analysis. *Annu. Rev. Biochem.* **84**, 499–517 (2015).

118. Tan, Y. Z., Cheng, A., Potter, C. S. & Carragher, B. Automated data collection in single particle electron microscopy. *Reprod. Syst. Sex. Disord.* dfv369- (2015). doi:10.1093/jmicro/dfv369

119. McMullan, G., Chen, S., Henderson, R. & Faruqi, A. R. Detective quantum efficiency of electron area detectors in electron microscopy. *Ultramicroscopy* **109**, 1126–1143 (2009).

120. Faruqi, A. R. & McMullan, G. *Electronic detectors for electron microscopy*. *Quarterly Reviews of Biophysics* **44**, (2011).

121. McMullan, G., Faruqi, A. R. & Henderson, R. *Direct Electron Detectors*. *Methods in Enzymology* **579**, (Elsevier Inc., 2016).

122. Li, X. *et al.* Electron counting and beam-induced motion correction enable near-atomic-resolution single-particle cryo-EM. *Nat. Methods* **10**, 584–90 (2013).

123. Danev, R. & Baumeister, W. Cryo-EM single particle analysis with the volta phase plate. *Elife* **5**, 1–14 (2016).

124. Wang, H.-W. & Fan, X. Challenges and opportunities in cryo-EM with phase plate. *Curr. Opin. Struct. Biol.* **58**, 175–182 (2019).

125. Elad, N., Bellapadrona, G., Houben, L., Sagi, I. & Elbaum, M. Detection of isolated protein-bound metal ions by single-particle cryo-STEM. *Proc. Natl. Acad. Sci.* **114**, 11139–11144 (2017).

126. Radermacher, M., Wagenknecht, T., Verschoor, A. & Frank, J. Three-dimensional reconstruction from a single-exposure, random conical tilt series applied to the 50S ribosomal subunit of Escherichia coli. *J. Microsc.* **146**, 113–136 (1987).

127. Wan, W. & Briggs, J. A. G. *Cryo-Electron Tomography and Subtomogram Averaging*. *Methods in Enzymology* **579**, (Elsevier Inc., 2016).

128. Galaz-Montoya, J. G., Flanagan, J., Schmid, M. F. & Ludtke, S. J. Single particle tomography in EMAN2. *J. Struct. Biol.* **190**, 279–290 (2015).

129. Leschziner, A. E. & Nogales, E. The orthogonal tilt reconstruction method: An approach to generating single-class volumes with no missing cone for ab initio reconstruction of asymmetric particles. *J. Struct. Biol.* **153**, 284–299 (2006).

130. Frank, J., McEwen, B. F., Radermacher, M., Turner, J. N. & Rieder, C. L. Three-dimensional

tomographic reconstruction in high voltage electron microscopy. *J. Electron Microsc. Tech.* **6**, 193–205 (1987).

131. Liu, Y., Penczek, P. A., McEwen, B. F. & Frank, J. A marker-free alignment method for electron tomography. *Ultramicroscopy* **58**, 393–402 (1995).

132. Mastronarde, D. N. Fiducial Marker and Hybrid Alignment Methods for Single- and Double-axis Tomography. in *Electron Tomography: Methods for Three-Dimensional Visualization of Structures in the Cell* (ed. Frank, J.) 163–185 (Springer New York, 2006). doi:10.1007/978-0-387-69008-7_6

133. Printemps, T., Bernier, N., Bleuet, P., Mula, G. & Hervé, L. Non-rigid alignment in electron tomography in materials science. *J. Microsc.* **0**, 1–8 (2016).

134. Weyland, M. & Midgley, P. A. Electron Tomography. in *Nanocharacterisation* (eds. Hutchison, J. & Kirkland, A.) 211–299 (The Royal Society of Chemistry, 2015). doi:10.1039/9781782621867-00211

135. Gontard, L. C. Removing the effects of the 'dark matter' in tomography. *Ultramicroscopy* **154**, 64–72 (2015).

136. Gontard, L. C., Cintas, H. & Borkowski, R. E. D. The benefit of thresholding carbon layers in electron tomographic tilt series by intensity downshifting. *J. Microsc.* **265**, 298–306 (2017).

137. Frank, J., Goldfarb, W., Eisenberg, D. & Baker, T. S. Reconstruction of glutamine synthetase using computer averaging. *Ultramicroscopy* **3**, 283–290 (1978).

138. Frank, J. Two-Dimensional Averaging Techniques. in *Three-Dimensional Electron Microscopy of Macromolecular Assemblies* (ed. Frank, J.) 34–70 (Oxford University Press, 2006). doi:https://doi.org/10.1016/B978-012265040-6/50003-5

139. Voss, N. R., Yoshioka, C. K., Radermacher, M., Patter, C. S. & Carragher, B. DoG Picker and TiltPicker: software tools to facilitate particle selection in single particle electron microscopy. *J. Struct. Biol.* **166**, 205–213 (2009).

140. Ramani Lata, K., Penczek, P. & Frank, J. Automatic particle picking from electron micrographs.

Ultramicroscopy **58**, 381–391 (1995).

141. Vargas, J. *et al.* Particle quality assessment and sorting for automatic and semiautomatic particle-picking techniques. *J. Struct. Biol.* **183**, 342–353 (2013).

142. Al-Azzawi, A., Ouadou, A., Tanner, J. J. & Cheng, J. Autocryopicker: An unsupervised learning approach for fully automated single particle picking in cryo-em images. *BMC Bioinformatics* **20**, 1–26 (2019).

143. Huang, Z. & Penczek, P. A. Application of template matching technique to particle detection in electron micrographs. in *Journal of Structural Biology* **145**, 29–40 (2004).

144. Chen, J. Z. & Grigorieff, N. SIGNATURE: A single-particle selection system for molecular electron microscopy. *J. Struct. Biol.* **157**, 168–173 (2007).

145. Wang, F. *et al.* DeepPicker: A deep learning approach for fully automated particle picking in cryo-EM. *J. Struct. Biol.* **195**, 325–336 (2016).

146. van Heel, M. & Frank, J. Use of multivariate statistics in analyzing the images of biological macromolecules. *Ultramicroscopy* **6**, 187–194 (1981).

147. van Heel, M. & Stöffler-Meilicke, M. Characteristic views of E. coli and B. stearothermophilus 30S ribosomal subunits in the electron microscope. *EMBO J.* **4**, 2389–2395 (1985).

148. Sorzano, C. O. S. *et al.* A clustering approach to multireference alignment of single-particle projections in electron microscopy. *J. Struct. Biol.* **171**, 197–206 (2010).

149. Yang, Z., Fang, J., Chittuluru, J., Asturias, F. J. & Penczek, P. A. Iterative stable alignment and clustering of 2D transmission electron microscope images. *Structure* **20**, 237–247 (2012).

150. Reboul, C. F., Bonnet, F., Elmlund, D. & Elmlund, H. A Stochastic Hill Climbing Approach for Simultaneous 2D Alignment and Clustering of Cryogenic Electron Microscopy Images. *Structure* **24**, 988–996 (2016).

151. Cheng, Y., Grigorieff, N., Penczek, P. A. & Walz, T. A Primer to Single-Particle Cryo-Electron Microscopy. *Cell* **161**, 438–449 (2015).

152. Yan, X., Dryden, K. A., Tang, J. & Baker, T. S. Ab initio random model method facilitates 3D

reconstruction of icosahedral particles. *J. Struct. Biol.* **157**, 211–225 (2007).

153. Elmlund, H., Elmlund, D. & Bengio, S. PRIME: Probabilistic initial 3D model generation for single-particle cryo-electron microscopy. *Structure* **21**, 1299–1306 (2013).

154. Reboul, C. F., Eager, M., Elmlund, D. & Elmlund, H. Single-particle cryo-EM—Improved ab initio 3D reconstruction with SIMPLE/PRIME. *Protein Sci.* **27**, 51–61 (2018).

155. Sigworth, F. J. A maximum-likelihood approach to single-particle image refinement. *J. Struct. Biol.* **122**, 328–339 (1998).

156. Scheres, S. H. W. RELION: Implementation of a Bayesian approach to cryo-EM structure determination. *J. Struct. Biol.* **180**, 519–530 (2012).

157. Scheres, S. H. W. A bayesian view on cryo-EM structure determination. *J. Mol. Biol.* **415**, 406–418 (2012).

158. Heidari Mezerji, H., Van den Broek, W. & Bals, S. A practical method to determine the effective resolution in incoherent experimental electron tomography. *Ultramicroscopy* **111**, 330–336 (2011).

159. Chen, D., Friedrich, H. & With, G. De. On resolution in electron tomography of beam sensitive materials. *J. Phys. Chem. C* **118**, 1248–1257 (2014).

160. Saxton, W. O. & Baumeister, W. The correlation averaging of a regularly arranged bacterial cell envelope protein. *J. Microsc.* **127**, 127–138 (1982).

161. Liao, H. Y. & Frank, J. Definition and Estimation of Resolution in Single-Particle Reconstructions. *Structure* **18**, 768–775 (2010).

162. Van Heel, M. & Schatz, M. Fourier shell correlation threshold criteria. *J. Struct. Biol.* **151**, 250–262 (2005).

163. Henderson, R. *et al.* Outcome of the first electron microscopy validation task force meeting. *Structure* **20**, 205–214 (2012).

164. Kucukelbir, A., Sigworth, F. J. & Tagare, H. D. Quantifying the local resolution of cryo-EM density maps. *Nat. Methods* **11**, 63–65 (2014).

165. Galaz-Montoya, J.G., & Ludtke, S. J. The advent of structural biology in situ by single particle cryo-electron tomography. *Biophys Rep.* **3**, 17-35 (2017).

166. Eggeman, A. S. Scanning transmission electron diffraction methods. *Acta Crystallogr B Struct Sci Cryst Eng Mater.*, **75**, 0-0 (2019).

167. Ophus, C. Four-Dimensional Scanning Transmission Electron Microscopy (4D-STEM): From Scanning Nanodiffraction to Ptychography and Beyond. *Microsc. Microanal.*, **25**, 563-582 (2019).

168. Midgley, P. A. & Eggeman, A. S. Precession electron diffraction–a topical review. *IUCrJ*, **2**, 126-136 (2015).

169. Cui, C., Gan, L., Li, H. H., Yu, S. H., Heggen, M., Strasser, P. Octahedral PtNi nanoparticle catalysts: exceptional oxygen reduction activity by tuning the alloy particle surface composition. *Nano Lett.* **12**, 5885-5889 (2012).

170. Kühl, S., Gocyla, M., Heyen, H. A., Selve, S. C., Heggen, M., Dunin-Borkowski, R. E., Strasser, P. Concave curvature facets benefit oxygen electroreduction catalysis on octahedral shaped PtNi nanocatalysts. *J. Mater. Chem. A.* **7**, 1149-1159 (2019).

171. Chattot, R., Le Bacq, O., Beermann, V., Kühl, S., Herranz, J., Henning, S., Kühn, L., Asset, T., Guétaz, L., Renou, G., Drnec, J., Bordet, P., Pasturel, A., Eychmüller, A., Schmidt, T. J., Strasser, P., Dubau, L., Maillard, F. Surface distortion as a unifying concept and descriptor in oxygen reduction reaction electrocatalysis. *Nat. Mater.* **17**, 827-833 (2018).

172. Chi, M., Wang, C., Lei, Y., Wang, G., Li, D., More, K. L., Lupini, A., Allard, L. F., Markovic, N. M., Stamenkovic, V. R. Surface faceting and elemental diffusion behaviour at atomic scale for alloy nanoparticles during in situ annealing. *Nat. Commun.* **6**, 8925 (2015).

173. Davey, W. P. Precision measurements of the lattice constants of twelve common metals. *Phys. Rev.* **25**, 753–761 (1925).